Segmentation of the aorta from 4D flow MRI for biomarkers computation

Diana Marin Castrillon

THESE DE DOCTORAT DE L'ETABLISSEMENT UNIVERSITE BOURGOGNE FRANCHE-COMTE

PREPAREE au Laboratoire ImViA

Ecole doctorale n°37

Sciences Pour l'Ingénieur et Microtechniques (SPIM)

Doctorat de Instrumentation, Informatique de l'image

Par

MARIN CASTRILLON Diana Marcela

Segmentation of the aorta from 4D flow MRI for biomarkers computation

Thèse présentée et soutenue à Dijon, décembre 2022

Composition du Jury :

Pr. GARREAU Mireille	PU à l'Université de Rennes 1, Rennes	Rapporteur
Pr. RUAN Su	PU à l'Université de Rouen, Normandie	Rapporteur
Pr. JACQUIER Alexis	PU-PH à CHU Marseille	Président
Pr. BOUCHOT Olivier	PU-PH à l'université de Bourgogne Franche-Comté	Directeur de thèse
Dr. BOUCHER Arnaud	MC à l'université de Bourgogne Franche-Comté	Co-encadrant de thèse
Dr. PRESLES Benoit	MC à l'université de Bourgogne Franche-Comté	Co-encadrant de thèse

Title : Segmentation of the aorta from 4D flow MRI for biomarkers computation

Keywords: 4D flow MRI, aortic aneurysm, aortic dissection, aortic segmentation, Deep learning

Abstract: Aortic dissection and aortic aneurysms are highly lethal pathologies. The latter is ranked as the nineteenth leading cause of death. Aortic aneurysms are defined as a dilatation greater than or equal to the diameter of the aorta. In clinical practice, the growth rate and size of the aneurysm are the main criteria for determining surgical intervention. However, new and better biomarkers of rupture and aortic dissection are needed for personalized treatment and better decision making. In this regard, the analysis of the interaction of blood flow with aortic tissues is a key factor. In recent years, 4D flow magnetic resonance imaging (MRI) has made it possible to acquire information on blood flow throughout the cardiac cycle. Despite the potential of this imaging modality, a previous 4D segmentation step is required to delineate the analysis of the fluid-structure interaction.

The aim of this thesis is to automatically segment the aorta from 4D flow MRI and to analyze the feasibility of using these automatic segmentations in the generation of biomarkers such as aortic wall pressure. To this end, we initially evaluated automatic 3D systolic phase segmentation with state-of-the-art methods such as multi-atlas-based and deep learning-based methods. With this study we have shown that deep learning outperforms the segmentation performance of the multi-atlas-based method. Furthermore, it was observed that biomarkers such as aortic wall pressure are more robust when using automatic segmentations from deep learning. Consequently, a 4D two approaches based on neural networks were proposed for aortic segmentation in the complete cardiac cycle.
With the analysis of the performance of the 4D segmentation, promising results were obtained and must be confirmed on databases from other hospitals.

Titre : Segmentation de l'aorte à partir de l'IRM de flux 4D pour le calcul de biomarqueurs

Mots clés: IRM de flux 4D, anévrisme aortique, dissection aortique, segmentation aortique, apprentissage profond

Résumé: Parmi les maladies cardiaques, la dissection aortique et les anévrismes aortiques sont des pathologies particulièrement létales. Cette dernière est classée comme la dix-neuvième cause de décès. Les anévrismes aortiques sont définis comme une dilatation supérieure ou égale au diamètre de l'aorte. Dans la pratique clinique, le taux de croissance et la taille de l'anévrisme constituent les principaux critères pour déterminer la nécessité d'une intervention chirurgicale. Cependant, de meilleurs biomarqueurs de rupture et de dissection aortique sont nécessaires afin d'effectuer un traitement personnalisé et une meilleure prise de décision. À cet égard, l'analyse de l'interaction entre le flux sanguin et les tissus aortiques est un facteur clé. Ces dernières années, l'IRM de flux 4D a permis d'acquérir des informations sur le flux sanguin tout au long du cycle cardiaque. La première étape pour profiter du potentiel de cette modalité d'imagerie est l'élaboration d'une méthode de segmentation 4D de l'aorte, permettant d'effectuer à des analyses de l'interaction fluide-structure.
L'objectif de cette thèse est de segmenter automatiquement l'aorte à partir de l'IRM de flux 4D et d'analyser la faisabilité de l'utilisation de ces segmentations automatiques dans la génération de biomarqueurs tels que la pression de la paroi aortique. À cette fin, nous avons d'abord évalué la segmentation automatique de la phase systolique en 3D avec des méthodes de pointe, telles que la segmentation basée sur des méthodes d'apprentissage profond. Avec cette étude il a été démontré que l'apprentissage profond surpasse la performance de segmentation de méthodes basés sur l'utilisation de multi-atlas. En outre, il a été observé que les biomarqueurs tels que la pression de la paroi aortique sont plus robustes lorsqu'on utilise des segmentations automatiques par apprentissage profond.
Par conséquent, deux approches 4D basées sur les réseaux neuronaux ont été proposées pour la segmentation aortique dans le cycle cardiaque complet.
Avec l'analyse des performances de la segmentation 4D, des résultats prometteurs ont été obtenus et doivent être confirmés sur des bases de données d'autres hôpitaux.

UBFC UNIVERSITE BOURGOGNE FRANCHE-COMTE
Université Bourgogne Franche-Comté
Bâtiment I3M, 64b rue Sully 21000
Dijon, France

ACKNOWLEDGMENTS

I would like to thank my thesis advisor Olivier Bouchot and co-supervisors, Benoit Presles and Arnaud Boucher for the opportunity to be part of this project. I also thank them for the support that each one with their experience gave me during these three years.

I would also like to thank Alain Lalande and Sarah Leclerc for the valuable knowledge they shared with me and for advice on how to be an optimistic researcher XD. But most importantly, thank you for showing me the humanity behind the research and for the moments we shared outside of the work context.

I thank Siyu Lin, my colleague and friend, for the help she gave me from the beginning, for all the coffee breaks and even for remembering everything for me. Her help was really valuable in these three years and I am happy to keep her friendship at the end of this journey. I especially thank my family: my mom Luz Castrillón, my dad Fernando Marín, and my sister Natali Marín and my brother in law Juangui. I thank them for supporting me from the distance, for making me feel that in every difficult moment their love can cross continents and for believing in me more than I do.

Last but not least, I thank my boyfriend Deivid Botina for his love support and company, for being the reason to go home happy with our cat Bruce despite any difficult day. And most importantly, I thank him for sharing a path of dreams fulfilled and dreams to fulfill.

Contents

List of Figures

List of Tables

List of Definitions

AAo: ascending aorta
AAS: Acute aortic syndromes
BA: Brachiocephalic artery
BAV: Bicuspid aortic valve
BAV: Bicuspid aortic valve
BN: Batch normalization
CFD: Computational Fluid Dynamics
CI: Confidence interval
CMRI: Cardiac magnetic resonance imaging
CNN: Convolutional neural networks
CT: Computed tomography
CV: Cross-validation
DSC: Dice similarity coefficients
ECG: Electrocardiography
FC-NN: Fully-connected neural network
GN: Group normalization
LCCA: Left common carotid artery
LDL: Low-density lipoprotein
LSA: Left subclavian artery
MAS: Multi-atlas-based segmentation
MRA: Magnetic resonance angiography
MRI: magnetic resonance imaging
MV: Majority voting
PAAo: Proximal abdominal aorta
PWMV: Patch weighted majority voting
RF: Radio frequency
RMSE: Root Mean Square Error
TAAs: Thoracic aortic aneurysms
TAo: thoracic aorta
TDAo: Thoracic descending aorta
TKE: Turbulent kinetic energy
tMIP: Temporal maximum intensity projection
tMSV: Temporal maximum velocity volume
Venc: Velocity encoding sensitivity
WMV: Weighted majority voting
WSS: Wall shear stress

INTRODUCTION

Aortic diseases can occur due to different conditions that cause increased aortic wall stress or abnormalities in the aorta. The second most common aortic disease and the nineteenth most common cause of death are aortic aneurysms, which are defined as an increase of 50% or more in aortic diameter [95]. The increase in diameter represents a lethal risk since it can cause rupture or tears in the aortic wall, called aortic dissection.

Patients with aortic aneurysms are managed based on their medical history, and the decision to operate is primarily based on the size and growth rate of the aneurysm [92]. However, ruptures and dissections have been observed in aneurysms with a smaller diameter than those indicated in the guidelines [5], which makes these decision parameters unreliable [46, 22]. A personalized decision making is therefore necessary and requires the generation of new predictors of aortic rupture and dissection.

Modern advances in magnetic resonance imaging (MRI) have led to the development of phase-contrast MRI, which encodes the blood flow in three directions to depict the evolution of blood flow during the cardiac cycle. This sequence can then be used to generate new predictors and biomarkers, such as those derived from fluid dynamics simulations. However, to use this information effectively, prior segmentation of the aorta is mandatory to limit the analysis to the fluid-structure interaction. A manual image segmentation process is tedious, time-consuming, and prone to inter- and intra-subject variabilities. Moreover, the amount of data in 4D flow MRI considerably increases the difficulty.

Several challenges must be addressed to automatically segment the aorta from 4D flow MRI: the low visibility and poor definition of some regions of the aorta due to the low resolution of the images, the high-dimensional space (3D and 4D), the computational cost of processing large volumes of data, and the generation of ground truths to implement and compare the performance of the algorithms. Advances in the field of image analysis have allowed the implementation of different automatic and semi-automatic segmentation methods for medical applications. In particular, machine learning-based methods have shown over the last decades a high performance in various segmentation tasks. For automatic or semi-automatic segmentation of the aorta from 4D flow MRI several approaches have been proposed. However, most of them have been limited to 3D segmentation of the aorta using a frame in the systolic cardiac phase or a 3D image generated with preprocessing. Then, the standardization of an automatic 3D aortic segmentation technique and the extension of segmentation to 4D is still an open problem.

This thesis is part of a research project that aims to prospectively assess biomechanical properties of the thoracic aorta by coupling magnetic resonance imaging with in vitro elasticity tests. In particular, the aim of this thesis is to address the automatic 3D and 4D segmentation of the aorta from 4D flow MRI. Addressing this problem contributes to expanding the use of this sequence in the analysis of blood flow dynamics and its influence on the rupture and dissection of aortic aneurysms by exploring new biomarkers. In the future, biomarkers related to the evolution of aortic pathologies, such as aneurysms, could be used for personalized diagnosis and prognosis.

The lack of a freely available 4D flow MRI database of the aorta with ground truths makes it difficult to generate a fully automatic segmentation pipeline based on the supervised machine learning methods or model-based methods implemented for this thesis. In order to overcome this problem, a dataset was generated with manual segmentation of the aorta from 4D flow images obtained at the university hospital of Dijon, France. With the generated database, we evaluated the performance of two automatic methods in 3D aortic segmentation from 4D flow MRI. These approaches were multi-atlas-based segmentation and deep learning-based segmentation. Based on the analysis of the segmentation performance of these methods, two 4D aortic segmentation strategies based on deep learning were proposed.

A general summary of our contributions is as follows:

- We created a dataset with 4D segmentations of the aorta from 4D flow MRI for the implementation and validation of automatic segmentation algorithms.
- We explored recent state-of-the-art methods for segmenting the aorta in the systolic phase of the cardiac cycle and their potential use for biomarker generation.
- We proposed and implemented a 4D strategy to segment the aorta based on a 3D deep learning model.
- We proposed and implemented a 4D deep learning model for aortic segmentation over the complete cardiac cycle from 4D flow MRI.

The rest of this manuscript is organized in seven chapters. In chapter one, an overview of the clinical context, causes and management of aortic aneurysm and aortic imaging techniques are presented.

Chapter Two covers the different methods of aortic segmentation proposed in the state-of-the-art and the fundamentals of the automatic segmentation methods applied in this thesis.

In chapter three, we present the details of the 4D flow MRI acquisition protocol and the manual segmentation of the aorta to generate the labeled dataset, which will be used later into our algorithms and used to validate them.

Chapter four presents the segmentation of the aorta in the systolic phase from 4D flow MRI, using multi-atlas and deep learning-based segmentation methods. The objective of chapter three is to evaluate these methods in our database and analyze the feasibility of a 4D implementation for the segmentation of the complete cardiac cycle and the use of automatic segmentations in biomarker computation.

In chapter five, we present the results of the evaluation of a 3D deep learning model in aortic segmentation from 4D flow MRI.

In chapter six, a 4D deep learning model for segmenting the aorta throughout the cardiac cycle using 4D flow MRI is therefore proposed. In order to evaluate the use of these segmentations in clinical practice, an analysis of widely used flow measurements is presented.

Finally, chapter seven summarizes the thesis and presents several perspectives.

I

CLINICAL CONTEXT AND STATE OF THE ART

1

CLINICAL CONTEXT

This chapter covers the clinical background related to our work in order to define our application field and the motivation of the thesis. First, the cardiovascular system, the causes and management of aortic aneurysms are described. Second, magnetic resonance imaging techniques of the aorta are presented. In particular, the benefits of extending 4D flow MRI for personalized prognoses of pathologies such as aortic aneurysms are presented.

1.1/ CARDIOVASCULAR SYSTEM

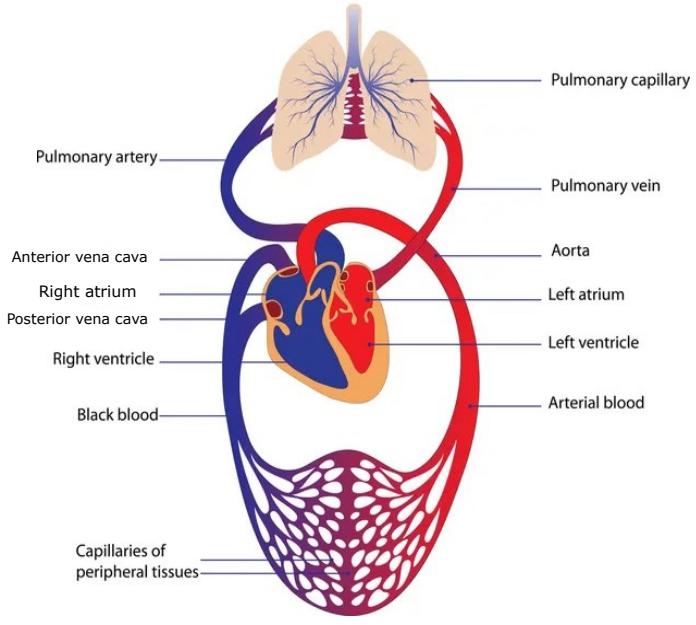

Figure 1.1: The cardiovascular system. Credit: `depositphotos.com`

The cardiovascular system consists of the heart and a network of arteries and capillaries that supply oxygen, proteins, and nutrients to the entire body and veins (Figure. 1.1). The cardiovascular system is divided into systemic and pulmonary circulation. The systemic circulation transports oxygenated blood from the heart

to the tissues. Blood is transported through the aorta to the neck, head, upper limbs, thoracic cavity organs, and lower limbs. Then, in the systemic capillaries, blood oxygen is exchanged for carbon dioxide resulting in oxygen-poor blood. The oxygen-poor blood returns to the heart's right atrium via the superior and inferior vena cava. Pulmonary circulation then begins, in which blood is carried from the right ventricle to the pulmonary trunk. The oxygen-poor blood reaches the lungs through the right and left pulmonary arteries to be oxygenated again. Finally, the oxygenated blood is transported to the left atrium through the pulmonary veins and the process starts again.

The heart is the center of this system since it periodically contracts to pump an average of five liters of blood. When the blood leaves the heart after each contraction, a certain pressure in the blood vessels is generated, known as systolic pressure. There is a period of rest between two contractions called cardiac relaxation, during which residual pressure in the blood vessels can be detected. This moment is known as diastole. In normal conditions, the systolic and diastolic pressures of an adult are less than 120 mmHg and 80 mmHg respectively.

1.1.1/ Heart Anatomy

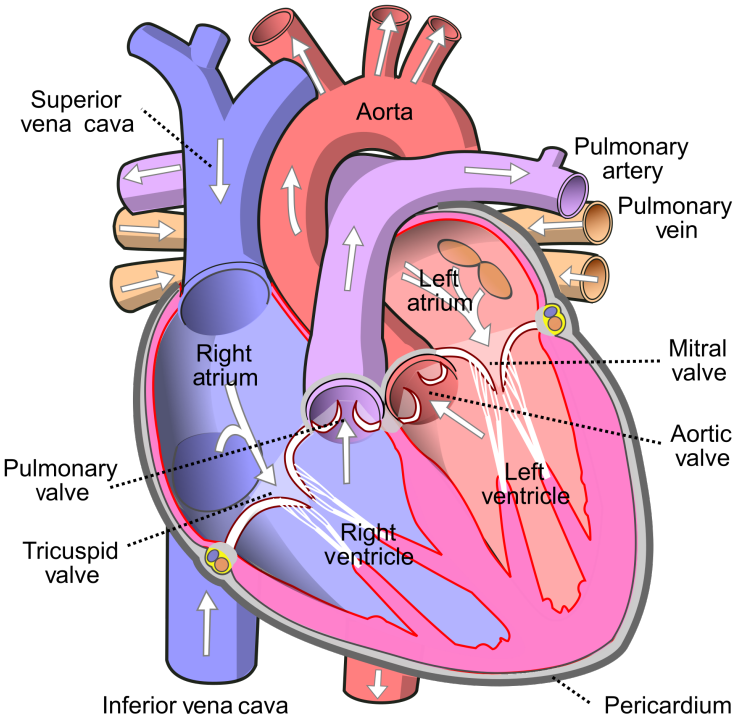

Figure 1.2: Sagittal section of the human heart. Credit: `wikimedia.org`

The heart is located in the thorax and is composed mainly of cardiac muscles. It is known as the pump of the cardiovascular system. Anatomically, the heart is di-

vided into two parts (right and left) by a wall known as the septum. There are four chambers in the heart, two called atria in the upper part and two called ventricles in the lower part. The atria are responsible for receiving the blood that enters the heart, and the ventricles deliver the blood to the different arteries. Each ventricle is equipped with a valve that ensures the unidirectional flow. Then, the blood flows in a single direction between the two unilateral chambers through the atrioventricular orifices (Figure. 1.2). The tricuspid valve is the right atrioventricular orifice valve named for its anterior, posterior, and septal cusps. This valve allows the body's blood circulating in the heart to reach the right ventricle, where it will be pumped to the lungs to receive oxygen. The mitral valve is composed of two leaflets and is located in the left atrioventricular orifice. At the exit of the right ventricle, the valve is called the pulmonary valve, and at the exit of the left ventricle, the valve is called the aortic valve. Through the pulmonary valve, deoxygenated blood and waste products exit into the pulmonary artery. Four pulmonary veins deliver oxygenated blood to the left atrium. The blood then passes into the left ventricle through the mitral valve.

1.1.2/ CARDIAC CYCLE

The cardiac cycle repeats about 70 times in one minute. It consists of a series of contractions and relaxations of the cardiac atria and ventricles during blood pumping (Figure. 1.3). The cycle begins with the right and left atria filling blood from the superior vena cava and pulmonary veins, respectively. When the pressure in the atria exceeds that of the ventricles, the atrioventricular valves open to allow blood to flow into the ventricles. Then, a ventricular contraction pushes blood out of the heart through the aorta and pulmonary artery. The pressure in the ventricles exceeds that in the atria inducing the closure of the atrioventricular valves to prevent blood return to the atria. Finally, the relaxation phase occurs, in which the ventricular pressure decreases until it is lower than the atrial pressure and leads to the atrioventricular valves opening to restart the cycle [31].

The key moments during the cardiac cycle are the end of diastole, where the volume of blood in the ventricles is at its maximum, and the end of systole, where the volume of blood in the ventricles is at its minimum.

1.1.3/ THE AORTA

The aorta is the largest artery in the body and is responsible for transporting oxygenated blood from the left ventricle to the rest of the body. The aorta begins at the aortic annulus and terminates at the bifurcation of the iliac arteries at the level of the L4 vertebra. This artery is divided into two regions, the thoracic aorta (TAo) and the abdominal aorta. The thoracic region is divided into ascending aorta (AAo), aortic arch and descending aorta (TDAo) [42] (Figure. 1.4). The aorta is composed mainly of elastic fibers, which allows it to have a relatively high

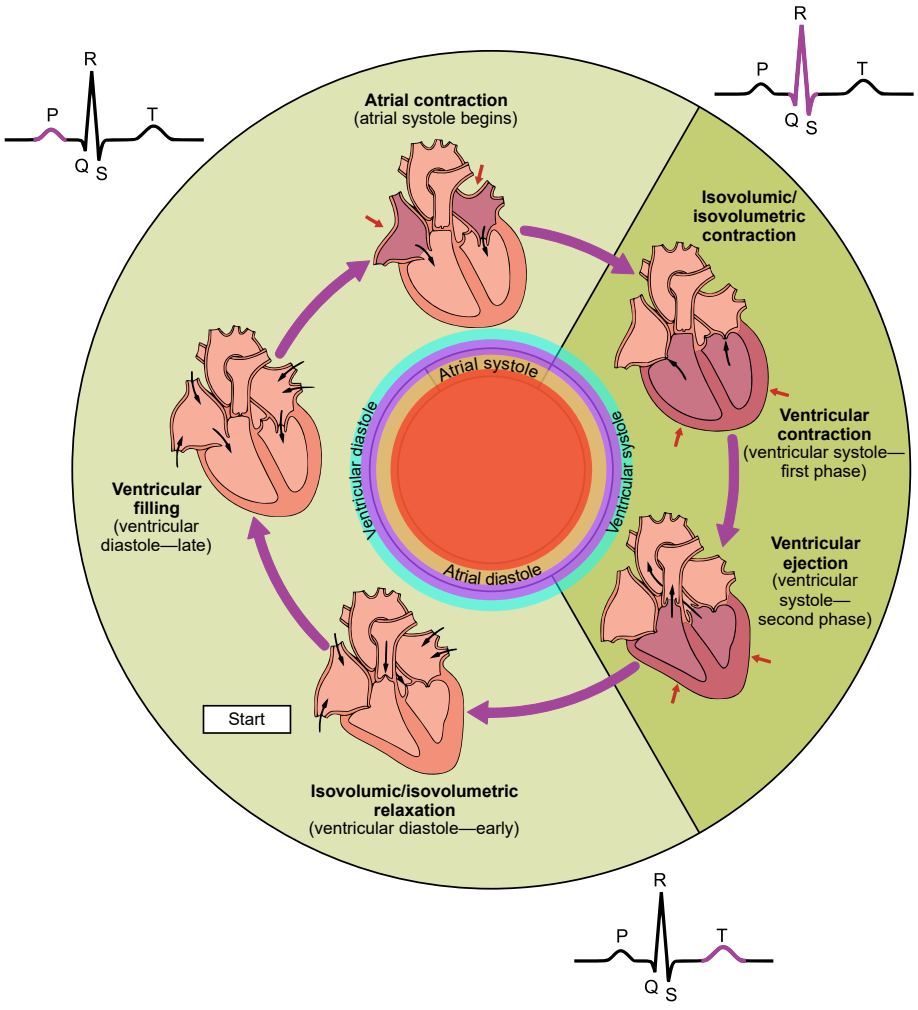

Figure 1.3: Phases of the cardiac cycle. Credit: `wikipedia.org`

compliance. The compliance allows the aortic wall to expand with each ejection of blood during the systolic phase, softening the impact of the pressure exerted by the blood flow on the aortic wall. During the diastolic phase, the aorta returns to its original position due to the absence of blood flow.

The aortic valve closes and opens to allow or restrict the passage of blood into the aorta. Usually, the aortic valve is composed of three movable leaflets or cuspids. However, it is possible to find unicuspid, bicuspid or quadricuspid aortic valves (Figure 1.5) due to congenital changes. Each of these leaflets assists in closing the valve and is composed of a rough surface facing the aorta and a smooth surface facing the ventricle. The aortic valve opens when the pressure exerted by the left ventricle exceeds the pressure of the aorta. This moment is known as the systolic phase and allows blood to flow from the left ventricle to the ascending aorta. The aortic valve leaflets close with the decrease in ventricular pressure during cardiac relaxation, initiating the diastolic phase. The valve leaflets are affixed to a structure known as the aortic annulus that lies between the outflow tract of the left ventricle and the beginning of the aorta.

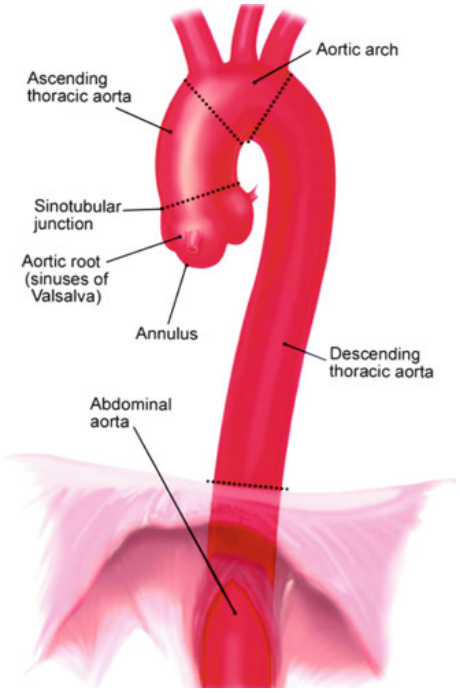

Figure 1.4: Regions of the aorta. Credit: Ladich et al. [63]

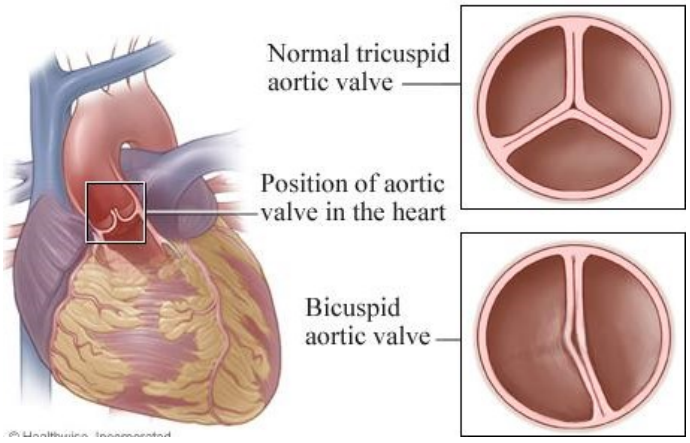

Figure 1.5: Tricuspid and bicuspid aortic valves. Credit: `www.umcvc.org`

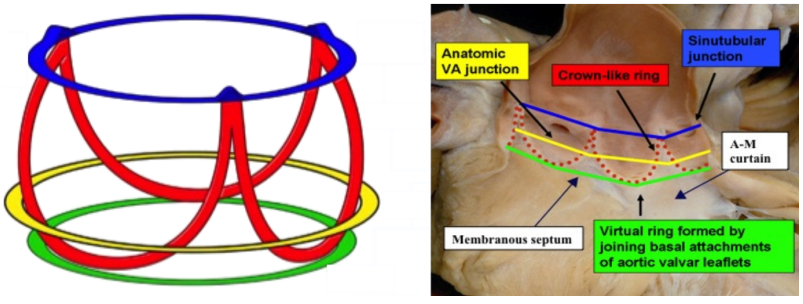

Figure 1.6: Three-dimensional illustration of the aortic root. Credit: `www.pcronline.com/`

The definition of the aortic annulus is controversial in the literature [83, 35]. From the surgeons' point of view, the aortic annulus is where the cusps communicates with the aortic wall. However, from the cardiologists' or radiologists' point of view, the aortic annulus is the virtual ring, which communicates the nadir of each leaflet joining in a circular shape [8, 64]. The aortic annulus certainly has a three-dimensional shape and an extremely complex function (Figure 1.6). The aortic valve annulus is composed of the virtual line that joins each leaflet nadir and the respective inter-leaflet triangles in the bottom part of this annulus. They are attached by the semilunar and the aortic leaflets. The main body of the annulus suspends from the sinotubular junction as an upper board. The entire system is integrated with the sinus of Valsalva, making it unique. The sinus of Valsalva is the three-dimensional space surrounding the aortic leaflets in the aortic root.

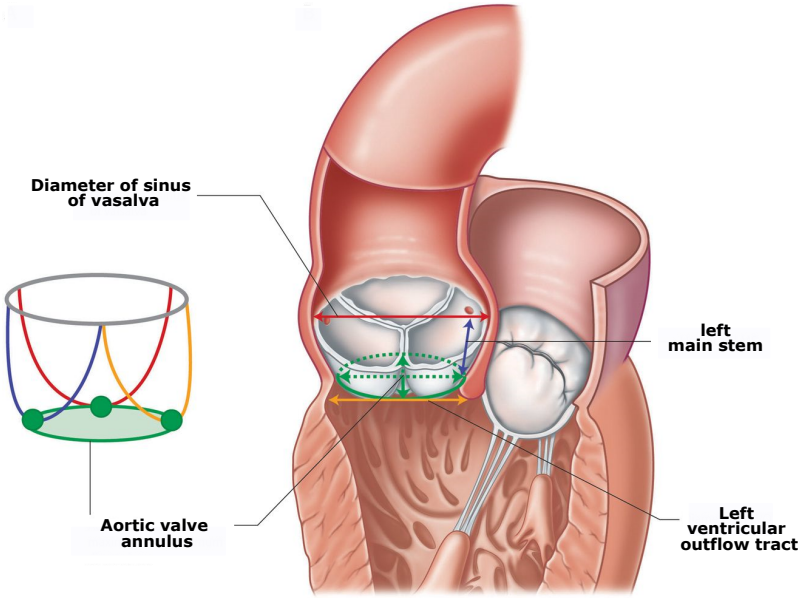

Figure 1.7: Three-dimensional illustration of the aortic root. Credit: `Kenny et al.` [51]

The supra-aortic ridge, also known as the sinotubular junction, is different from other parts of the aortic valve annulus. Sinotublar junction can be regarded as a hemodynamic annulus with a high ability to move with systole and diastole. The sinotubular junction is one of the key components of aortic root architecture and aortic valve function [15]. The sinotubular junction increases in diameter over time with age and hypertensive cardiomyopathy. A healthy, normal heart has sinotubular junction diameters of about 75% of the maximum diameter of the sinus of valsalva 1.7.

[23].

Definitions of Aortic Aneurysm[a]

Disorder/Recommendation	Description
Abdominal	
Aneurysm	>3 cm localized, segmental, full-thickness enlargement from diaphragm to bifurcation to right and left iliac arteries
Surgery recommended	Size >5.4 cm
Thoracic	
Aortic root dilation	>3.7 cm
Ascending aortic and arch aneurysm	>3.6 cm
Descending aortic aneurysm	>2.5 cm
Surgery recommended	Size >5.4 cm; elective surgery recommended for Marfan with size 4-5 cm

[a]Note that based on the source, these definitions can vary. Aortic dimensions are strongly and positively correlated with age, male sex, and body size. Normal cut-off values vary slightly, depending on the imaging modality used.

Figure 1.8: Definition of aortic aneurysm depending on region. Credit: Ehrman et al. [92]

1.1.4/ AORTIC ANEURYSMS

Aortic aneurysms can occur in different regions of the aorta. In the thoracic part they are called thoracic aortic aneurysms and in the abdominal part, they are called abdominal aortic aneurysms. Aneurysms are classified as an increase in the diameter of the aorta higher than or equal to 50% of the expected size [55]. The aorta' expected size might vary with factors such as age, sex, and even the region of the aorta. In the literature, the thresholds vary slightly. Figure 1.8 defines the diameters considered to be an aneurysm according to the region of the aorta. The increase in aortic diameter is highly risky since it can trigger a rupture or dissection of the aortic wall. However, early diagnosis of this pathology allows to provide treatments that improve the outcome [7].

Overall death rates related to aortic aneurysms or aortic dissection have increased from 2.49 per 100,000 in 1990 to 2.78 per 100,000 in 2010. Aortic aneurysms are often diagnosed by accident during medical imaging indicated for other pathologies. Therefore, the increase in the incidence of aortic pathologies may be due to advances in medical imaging techniques. Thoracic aortic aneurysms (TAAs) present a silent phase of growth in 95% of cases, so patients are asymptomatic until an acute event occurs. Acute events include aortic dissection, aortic ulcer, intramural hematoma and unstable or painful thoracic aortic aneurysm. The overall incidence per year of TAAs is 5 to 10 per 100,000 people.

About 60% of all TAAs occur in the aortic root or in the AAo [16]. TAAs are more common in men than in women. However, women have a less favorable outcome as a result of factors related to estrogen loss, which affects the flexibility of the aorta. Women also tend to have smaller aneurysms than men when it comes to acute aortic syndromes, such as dissection [95].

1.1.5/ Risk factors and causes of aortic aneurysm

Various pathologies and etiologies are associated with aortic aneurysms. The most common are atherosclerosis, connective tissue, and aortic valve disorders. Moreover, smoking and traumatic injuries can also be associated with increased aortic diameter.

Atherosclerosis: Arteriosclerosis occurs in the wall of the aorta and is one of the common causes of aneurysms. Specifically, it is an inflammation of the aortic wall due to hypercholesterolemia, a very high level of low-density lipoprotein cholesterol. [65]. It has been suggested that atherosclerosis induces the generation of aneurysms since changes in the aortic wall due to inflammatory mechanisms triggered by atherosclerosis also contribute to the development of aneurysms.

Aortic valve disorders: Bicuspid aortic valve (BAV) is a congenital condition in which the aortic valve has two instead of three cusps. About 26% of patients with BAV develop an aneurysm in the ascending aorta [37]. Another widely known problem of the aortic valve is stenosis, defined as narrowing the valve that restricts the passage of blood from the ventricle. 50% of ascending aortic aneurysms are associated with this pathology. On the other hand, the return of blood to the ventricle, known as aortic insufficiency, is present in 33% of patients with aneurysm [40].

Connective tissue disorders: Marfan syndrome is a systemic connective tissue disorder caused by a mutation in the fibrillin-1 gene [17]. This syndrome occurs in about three out of every 100,000 people. Almost all people with this syndrome develop one or more types of aortic disease, such as aortic aneurysm, aortic dissection, or rupture.

As with Marfan syndrome, Loeys-Dietz syndrome affects the connective tissue and is caused by a mutation, but in this case, in the transforming growth factor-beta (TGF-β) receptor. The clinical features of both syndromes are similar, but in general, the cardiovascular manifestations are more severe with Loeys-Dietz syndrome. For example, aortic dissection or rupture usually occurs in younger patients with smaller aortic dilatations [67]. The Myosin Heavy Chain 11 (MYH11)

syndrome has also been linked to the development of aneurysms because it generates a mutation of the MYH11 gene that affects a smooth muscle cell contractile protein [20].

1.1.6/ THE RISK ASSESSMENT

The management of patients with an aortic aneurysm consists of periodic follow-ups to establish the growth rate and diameter of the aneurysm. Based on this information, the decision is made to intervene surgically to replace the weakened tissue with a tube graft (Figure 1.9).

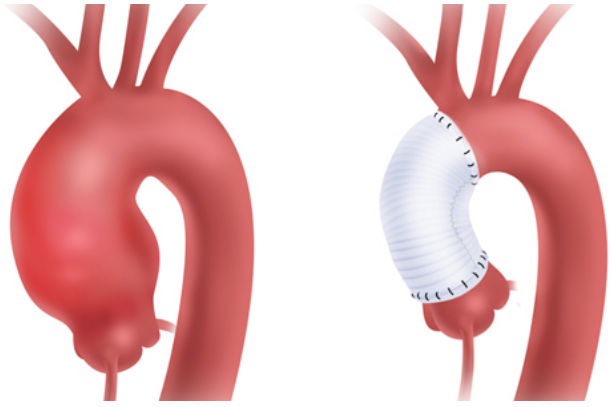

a) Pre-repair **b) Post-repair**

Figure 1.9: Replacement of aortic tissue weakened by a tube graft. Credit: `mainlinehealth.org`

The definition of a standard aortic diameter is problematic because it can increase with age, weight, and height. Therefore, some studies have proposed a relationship between aortic diameter with weight and height, rather than individual values [12, 11]. Some studies have suggested absolute values as thresholds for the indication for surgery under various criteria (Figure. 1.10). Coady et al. [5] provided the basis for the European guidelines [5]. They emphasize that aortic dissection or rupture can occur in aneurysms of different sizes but that the risk when the diameter is greater than or equal to 60 mm is extremely high. For this reason, the European guidelines recommend repair surgery for this pathology when the aneurysm reaches 55 mm.

In addition to aortic diameter, the following risk factors are also taken into account in decision making [5]:

- Growth rate ($\geq$ 5 mm per year)
- Connective tissue disorders
- Unicuspid or bicuspid aortic valve

- Arterial hypertension
- Family history of aortic complications.

Recommendations	Class[a]	Level[b]
Surgery is indicated in patients who have aortic root aneurysm, with maximal aortic diameter[c] ≥50 mm for patients with Marfan syndrome.	I	C
Surgery should be considered in patients who have aortic root aneurysm, with maximal ascending aortic diameters: • ≥45 mm for patients with Marfan syndrome with risk factors.[d] • ≥50 mm for patients with bicuspid valve with risk factors.[e,f] • ≥55 mm for other patients with no elastopathy.[g,h]	IIa	C
Lower thresholds for intervention may be considered according to body surface area in patients of small stature or in the case of rapid progression, aortic valve regurgitation, planned pregnancy, and patient's preference.	IIb	C

Figure 1.10: Recommendations on interventions on ascending aortic aneurysms. Class a is assigned when based on the evidence, surgery is recommended. Level of evidence b is assigned when data are acquired from a single clinical trial. Credit: Erbel et al. [43]

Pape et al. [22] analyzed the reliability of aortic diameter as a predictor of type A aortic dissection. Type A dissection involves the ascending aorta with possible progression to the descending TAo. In a cohort of 591 patients with type A aortic dissection, they found that 349 patients had an aortic diameter < 5.5 cm and 229 had a diameter < 5.0 cm at the time of aortic dissection. Following the current indicators proposed in the guidelines for aortic aneurysm repair surgery, 99% of the patients used in the study would not be included. Then, they concluded that aortic diameter is insufficient to decide on the timing of surgery and that new predictors are needed for a better care.

1.2/ MAGNETIC RESONANCE IMAGING

Magnetic resonance imaging (MRI) is a widely used technique for generating high-resolution and high-contrast medical images of soft tissues. MRI is a non-

ionizing modality used to image mainly water, a molecule composed of two hydrogen atoms and one oxygen atom (i.e. H_2O) an abundant molecule in the human body.

The images of the organ of interest are produced by a phenomenon called nuclear resonance, produced when the nucleus of the hydrogen atoms interacts with a magnetic field. Hydrogen atoms contain one negatively charged electron and a single positively-charged proton in the nucleus. The nucleus or proton is called a spin and can be seen as a small magnet that rotate around its axis. These spins are naturally randomly oriented (Figure 1.11 **A**), but in the presence of a strong magnetic field B_0, most are aligned parallel to the field and a smaller amount anti-parallel (Figure 1.11 **B**). Because of the ratio of spins aligned in both directions, it is the excess of parallel aligned spins that have the potential to produce a signal that can then be turned into an image. The main axis of the external magnetic field B_0 is the z-axis, and the spins precess around this axis. Considering Larmor's relation (Equation 1.1), the speed of precession of the spins is proportional to the strength of B_0.

$$v_0 = \gamma B_0 \tag{1.1}$$

where, γ is the gyromagnetic ratio. For the hydrogen nucleus $\gamma = 42.58$ MHz/T. Then, in the presence of a 1.5 Tesla magnetic field, the precessional speed is around 64 MHz.

As a result of the precession of the spins, a magnetic force M is produced in the z-axis direction. The magnetic resonance signal is created by moving the net magnetization vector M from the z-axis to the x-y plane. For this, a second magnetic field B_1 is applied for a short period (1-5 ms), which is considered a radio frequency (RF) pulse. B_1 is different from B_0 because it is not static and rotates at the same frequency as the spins but in the xy-plane. That is, B_1 must be in resonance with the spin precession. Since for M to go from rotating on the z-axis to rotating on the y-axis a $90°$ rotation occurs, B1 is known as $90°$ RF pulse (Figure. 1.11) [26].

After the deactivation of the RF pulse, an event called relaxation occurs. The recovery of the magnetic vector M on the z-axis is characterized by a relaxation time T_1. In the x-y transverse plane, the decay of the magnetization vector is characterized by a relaxation time T_2. Here, the magnetization decay is due to the presence of small magnetic fields in the tissues that cause the magnetic field to lose heterogeneity.

1.2.1/ RELAXATION T_1

T_1 relaxation, also known as spin-lattice relaxation occurs with the return of M to its original position. Thus, T_1 describes the time it takes for M to grow back

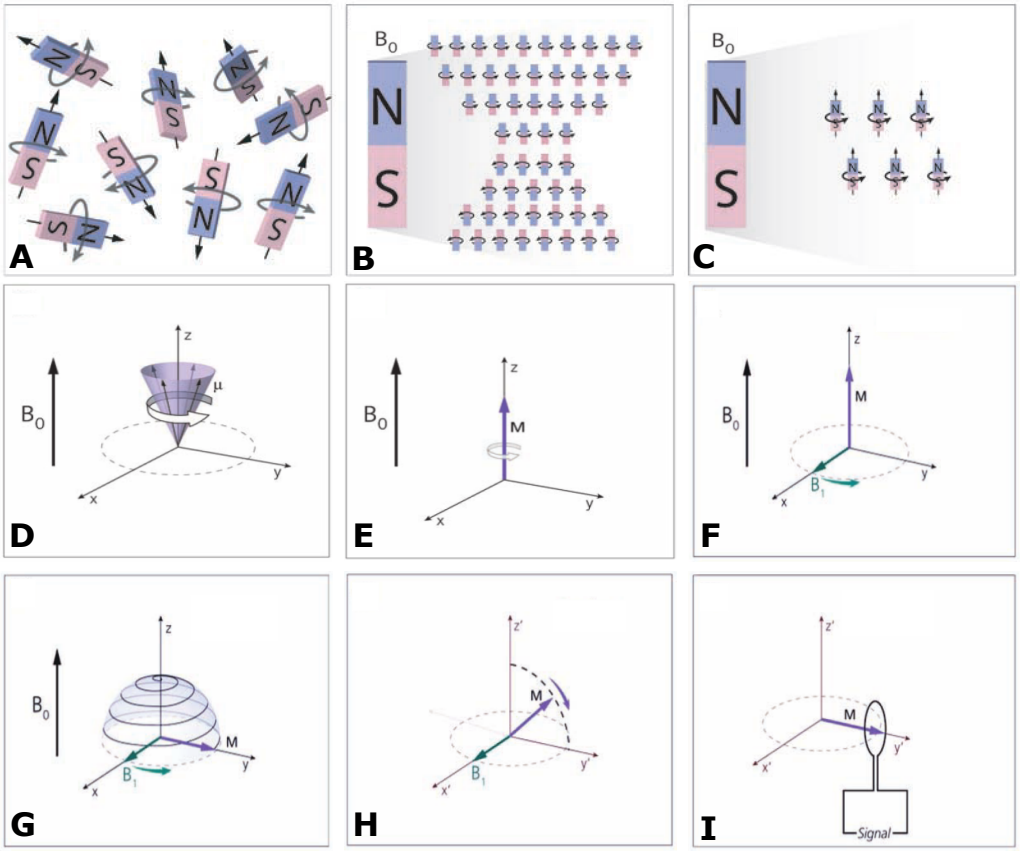

Figure 1.11: **A)** Randomly oriented spins. **B)** Spins in the presence of external magnetic field (B_0). **C)** Difference of spins oriented parallel and antiparallel to the B_0 field. **D)** Excess of spins precessing in the direction of B_0. **E)** Projection of the vectors in the z-axis to form the magnetization vector M. **F)** Activation of the RF pulse (B_1). **G)** Net magnetization precessing over B_1 and B_0 into the transverse x-y plane. **H)** B_1 rotates at the frequency of the spins, so it appears stationary. Then, M appears to rotate only about B_1. When M lifts the y-axis, B_1 is turned off to achieve a rotation of 90. **I)** The magnetization vector M produces a signal on a wire antenna. **Credit:** Raymond Y. Kwong [26]

to 63% of its original value, i.e. before the $90°$ RF pulse. The magnetization T_1 grows exponentially along the z-axis and reaches its maximum value after a long time (Equation 1.2). For the myocardial T1 is around 900 ms. After 3 T_1, the magnetization reaches 95% of its maximum value.

$$M_Z(t) = M_{Z(t=\infty)}[1 - e^{-t/T_1}] \tag{1.2}$$

1.2.2/ Relaxation T_2

The relaxation T_2 depends on the spin-spin relaxation process. This relaxation describes the decay of the magnetization vector M, with T_2 being the time it takes

for M to decay to 37% of its original value in the x-y plane. Equation 1.3 states that the magnetization in the transverse x-y plane at t=0 decays exponentially respect to the elapsed time t and a constant T_2. In the myocardium, T_2 is about 50 ms. The signal decays as a results of the inhomogeneities generated by the magnetic fields coming from the tissues.

$$M_{XY}(t) = M_{XY(t=0)}e^{-t/T_2} \tag{1.3}$$

1.2.3/ SIGNAL LOCALIZATION

Once the image generating signal is acquired, it is necessary to encode it to identify the location of the signal in 3D space. The signal is localized using three processes that provide a one-to-one correlation with other measurable features in the tissue. The three processes are slice selection, frequency encoding, and phase encoding.

1.2.3.1/ SLICE SELECTION

This step aims to select a slice and excite only the spins in this slice. Thus, instead of acquiring signals from the whole body, they are acquired in a region of interest defined by the slice. The objective is to obtain in this region of interest that the magnetization M rotates down to the y-plane and that at any other point of the body the magnetization remains oriented in the z-axis. Since only spins precessing at a frequency equal to the RF frequency generate a signal, magnetic fields (gradients) are added to or subtracted from B_0 to change its uniformity in a given region. For example, the gradient field along the z-axis causes spins in different planes parallel to the transverse to precess at different frequencies.

1.2.3.2/ FREQUENCY ENCODING

For frequency coding, gradient pulses are applied when the MR signal is acquired (readout gradient). This method allows the signal to be encoded in space so that the signal's origin can be determined. This phenomenon is because the readout gradient applied along the x-axis forces the magnetization at different points on the axis to precess at different speeds. Then, this collected signal masks the different frequencies to determine its spatial position. The signal is encoded in a Fourier plane for both frequency and phase encoding. These two processes allow defining the origin of a signal by locating the line and the position of the point in the Fourier plane that produces it.

1.2.3.3/ PHASE ENCODING

Although frequency coding works to determine where the signal originates from on the x-axis, the same type of coding cannot be used simultaneously for the y-axis. Phase coding is then used to overcome this problem. Phase encoding works on the principle that the angle (phase) of the magnetization vector M provides information about the signal's origin on the y-axis. For this, a gradient pulse is applied in the y-axis for a short time (after RF but before acquisition). Then, the M vectors precess at different velocities and will be at progressively larger angles with respect to the axis for that short period. In the end, the signal from each pixel in the image has a unique combination of phase and frequency.

1.3/ CARDIAC MAGNETIC RESONANCE IMAGING

In recent years, the development of multiple medical imaging techniques has made it possible to obtain anatomical and/or functional information about the heart and large vessels such as the aorta. In particular, images of the aorta are currently acquired using computed tomography (CT) or MRI techniques [59]. CT is widely used for the TAo study because it is commonly available in clinical practice and because its spatial resolution and acquisition time are lower than MRI. In cardiac applications, CT is used, for example, in shape and motion analysis of the heart and the aorta [88], for interventions planning [82] and for guiding thoracic endovascular repair [80]. For kinetic analysis of the aorta, electrocardiography-gated CT is recommended to avoid false flap related to the high pulsatility of the aortic root. However, this technique increases x-ray exposure, acquisition time and requires breath-hold. Moreover the use of iodinated contrast media is also a limitation of CT. Thus, MRI has become an option to replace CT in the study of the aorta.

Unlike other cardiac imaging techniques, cardiac magnetic resonance imaging (CMRI) has important advantages. They allow a qualitative and quantitative evaluation of blood and heart motion in a selected plane without ionizing radiation. CMRI performance is related to the choice of technical parameters during acquisition such as the acquisition time or the trade-off between spatial resolution and signal-to-noise ratio.

Compared to static organ MRI, CMRI faces a challenge in the high-definition representation of an organ contracting and moving in the thorax due to the respiratory cycle. Therefore, cardiac gating and respiratory gating are essential components of CMRI. CMR is not a real-time image. The signals in the Fourier plane are acquired line by line, which requires cardiac gating.

Cardiac gating Cardiac gating is essential to deal with the blurring of images due to heart contraction and the effect of pulsatile blood. For this purpose, image

acquisition is coordinated with the cardiac cycle. The most effective way is cardiac gating using electrocardiography (ECG). With this method, image acquisition is triggered after the detection of the R-wave. In this way, the resulting image seems static and matches the exact moment in the cardiac cycle.

Respiratory gating Respiratory gating is necessary because the heart is in the diaphragm, a muscle that manages the breath. Respiratory motion is one of the causes of image blur and artifacts in the phase encoding direction. The most common practice in standard cardiac sequences to avoid these artifacts is to hold the breath. Drawbacks of this method are, for example, the low breath capacity of a patient and the variation in the degree of breath-holding. Respiratory gating can be performed by following the respiratory cycle. Thus, acquisition can be performed at the end of the respiratory phase or by rejecting data acquired outside a specific respiratory window.

1.3.1/ MAGNETIC RESONANCE ANGIOGRAPHY

Magnetic resonance angiography (MRA) is a technique that allows the imaging of blood vessels. MRA can be acquired with or without a contrast agent and is used in clinical practice to detect abnormalities such as aneurysms or stenosis [27]. In recent years MRA has replaced X-ray angiography in evaluating aortic disease. Advances in the field of magnetic resonance imaging have made it possible to obtain MRA images in a single breath-hold. Although a contrast agent is used for MRA acquisition, the material used as contrast (Gd-DTPA) in this technique has a favorable safety compared to the iodine-based material used in X-ray angiography or CT acquisition. DTPA (diethylenetriaminepentaacetic acid) shortens the T1 of the spins, which provides an intense bright signal in the vessel lumen regardless of flow direction or velocity. The image quality depends on the concentration of the contrast agent within the artery. Therefore, synchronizing image acquisition with the concentration of Gd-DTPA inside the aorta is essential [26].

1.3.2/ 4D FLOW MRI

4D flow MRI, also known as phase-contrast 3D MRI (3D PC-MRI), is an MRI technique for quantitatively evaluating blood flow. Compared to 2D phase-contrast MRI, which allows the evaluation of blood flow in a single slice, 4D flow MRI provides temporal and spatial 3D information. Therefore, with the information obtained from 4D flow MRI it is possible to visualize the 3D flow and perform a retrospective quantification. [45].

PC-based MRI images take advantage of the direct relationship between blood flow velocity and the phase of the acquired MRI signal for image generation. For the acquisition of the raw data, four consecutive acquisitions are performed. One

acquisition is used as a reference, and the other three encode the velocity in x, y, and z axis by adding bipolar gradients along each axis to eliminate unwanted background phase effects [38]. This process allows the coding of the flow according to a specific direction. So, three phase images that encode the blood velocity values in the x, y, and z directions are obtained. Moreover, four magnitude images with anatomical information are reconstructed. Three encode undirected flow strengths at x, y, and z directions. The additional magnitude image is obtained by averaging the intensities of the latter (Figure 1.13).

An important parameter to be defined during the acquisition of 4D flow MRI is the velocity encoding sensitivity (Venc). This value represents the maximum flow velocity that can be acquired. Venc is defined by considering the flow patterns in the patient. The selection of Venc must be made carefully since if the flow velocity is higher than the set one, velocity aliasing may occur. Aliasing is a sudden change from high to low velocity in a flow region (Figure 1.12). Nevertheless, using a high Venc value to cover all flow velocities is not recommended because this will produce images with a lack of contrast.

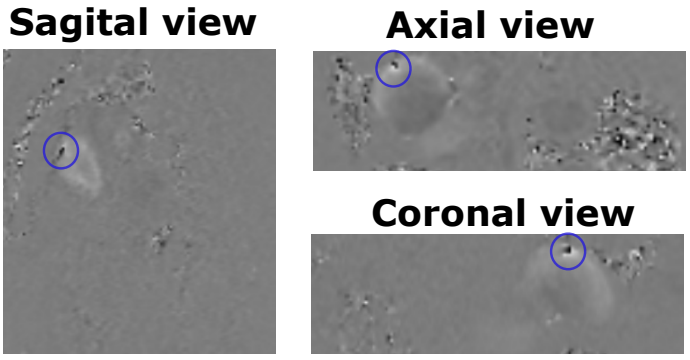

Figure 1.12: Example of aliasing in a patient with Venc equal to 450 cm/s. Aliasing appears when the blood flow velocity exceeds the VENC. Then, an inverted value appears in the image, meaning that the measured flow seems to be going in the opposite direction.

The potential of 4D flow MRI compared to angiography and 2D PC-MRI lies in the possibility of evaluating the hemodynamics of cardiovascular pathologies at a global and local level. However, the acquisition time of a 4D flow MRI is typically around ten minutes, considerably longer compared to the acquisition time of a 2D PC-MRI or MRA, which is about two minutes. Markers such as vessel diameter, mean velocities, and net flow are calculated in clinical practice by echocardiography. In addition to these markers, 4D flow allows exploring new and more advanced biomarkers related to fluid-structure interaction, such as, wall shear stress (WSS), pressure difference and turbulent kinetic energy (TKE) [60].

Some studies have suggested the diagnostic potential of 4D flow MRI. Rodriguez et al. [77] have evaluated the hypothesis that BAV promotes aortic dilatation due to abnormal flow impacting the wall. The results of this study suggested that hemodynamic flow abnormalities caused by BAV are associated with dilatation of the ascending aorta. Thus, they concluded that the flow pattern analysis might

help identify the risks of aortic pathology progression. WSS has been one of the most analyzed biomarkers in the evolutions of aortic diseases. Guzzardi et al. [49] were able to establish a correlation between WSS and aortic elastic fiber degeneration in patients with BAV. Soulat et al. [106] performed a five-year follow-up of 72 patients and found an association between WSS from 4D flow MRI and faster aortic growth. This could help determine which patients to follow more closely.

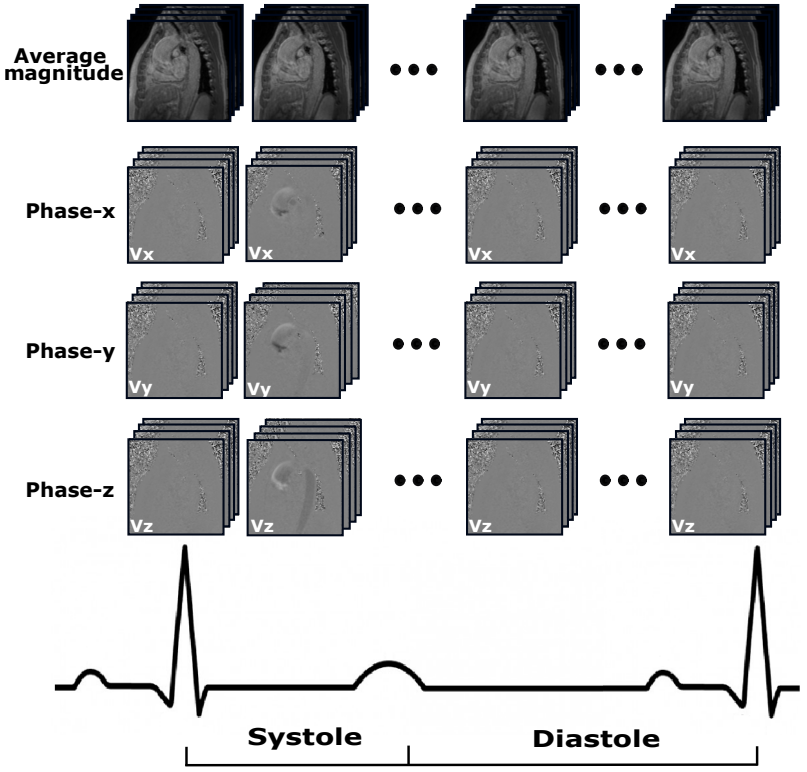

Figure 1.13: 4D flow MRI. Anatomical information is provided by the magnitude image. Functional information is provided by the phase images encoding the velocity in the x, y and z directions.

Despite the benefits of 4D flow MRI, this sequence is not widely used in clinical practice to generate hemodynamic markers to support decision-making. The challenges of 4D flow MRI are related to the lack of standardization in analyzing the information and the large amount of data to process. Particularly, the delineation of the region of interest is a challenging previous step to the analysis of the fluid-structure interaction. This process allows for the delineation of the flow velocity information to be retrieved. The delineation of the aorta from 4D flow MRI of subjects with cardiac pathologies is particularly complicated since image quality is usually reduced. This is generally due to cardiac arrhythmia and double systole peaks in the ECG that affect the acquisition, particularly when it is retrospective gating.

1.3.3/ 4D FLOW-BASED ANGIOGRAPHY

Despite the ability of MRA to provide detailed information on vascular geometry, this sequence does not provide information on the progression of blood flow during the cardiac cycle. Recently, the generation of 4D flow-based angiography has been proposed to obtain an image that, like MRA, enhances regions with high velocities.

Several similar algorithms have been proposed for the generation of 4D flow-based MRA from 4D flow MRI [21]. The different algorithms have in common that they merge different time/temporal information, e.g. Equation. 1.4. The temporal information is mixed, since applying this process to each frame independently would produce some frames in which the aorta cannot be differentiated from the background. The latter is because the visibility of the vessels depends on high velocities, and in diastole, the velocities are close to zero.

Moreover, due to the 4D flow-based MRA generation process, images may be generated where the artery wall is underestimated. The latter is due to flow patterns over the cardiac cycle leading to low velocities close to the vessel wall.

As an example, Figure 1.14 shows an acquired MRA and an angiography generated from 4D flow MRI for the same patient.

$$\text{4D flow-based MRA} = \frac{1}{T}\sum_{t=1}^{T} M_t^2 * (V_{x,t}^2 + V_{y,t}^2 + V_{z,t}^2) \tag{1.4}$$

where M is the magnitude image and V_x, V_y, and V_z the phase images for x, y and z directions, respectively. T is the number of temporal frames acquired over the cardiac cycle.

1.4/ CONCLUSION

In this chapter, we reviewed the clinical context of aortic pathologies, especially aortic aneurysms. Findings in recent years have shown that the information provided by 4D flow MRI is valuable and opens the door to the generation of new and more appropriate biomarkers for the prognosis of aortic pathologies. Thus, the exploration of hemodynamic biomarkers represents a great potential to support markers such as growth rate and diameter of an aneurysm that, although helpful, are not sufficient to decide the timing of a surgical intervention. However, before using the information provided by 4D flow MRI, it is necessary to segment the aorta in order to delimit the information to be used in the fluid-structure analysis.

The challenges of aortic segmentation from 4D flow MRI for biomarker computation are mainly associated with low image contrast and spatial resolution. In

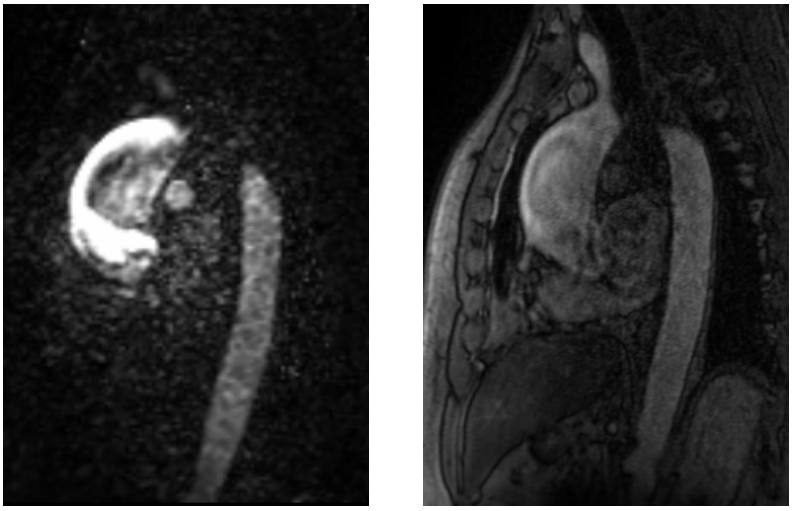

a) 4D flow based angiography **b) Magnetic resonance angiography**

Figure 1.14: **a)** Slice of a generated 4D flow based angiography. **b)** acquired magnetic resonance angiography for the same patient.

particular, segmentation of the aorta in patients may be more difficult since arrhythmia or double peaks in the ECG affect the gating of the sequence and, consequently, the image's resolution. Most of the studies have tried to overcome the lack of image contrast by generating images from 4D flow, such as 4D flow-based MRA, which, as mentioned above, mixes temporal information in its 3D version and suffers from a bias or dependence on registration quality in its 4D version.

2

State of the art

This chapter presents the methods proposed in the state-of-the-art for aortic segmentation from 4D flow MRI. First, the types of methods used in 3D aortic segmentation are presented. Then, the techniques covered for aortic segmentation over the entire cardiac cycle are presented. Finally, to understand the details of the implemented segmentation methods in this work, this chapter presents the fundamentals of multi-atlas-based segmentation and deep learning methods.

2.1/ Segmentation of the aorta from 4D flow MRI

Segmenting the structure for which a fluid-structure analysis must be performed is a necessary preliminary step that presents several challenges. Manual segmentation is time consuming, so it is not an option in this type of application. The approximate time required for segmenting one of the frames acquired in the cardiac cycle is 3.5 hours. Therefore, the generation of manual segmentations throughout the cardiac cycle is impractical. Moreover, manual segmentation is prone to intra- and inter-observer variabilities. In recent years, advances in semi or fully automated segmentation methods have opened up the possibility of exploring new biomarkers derived from 4D flow MRI. Aortic segmentation using 4D flow MRI has been achieved by several researchers. The following are the segmentation methods proposed in the state-of-the-art.

2.1.1/ 3D segmentation of the aorta from 4D flow MRI

Due to the difficulty of generating ground truths for implement and validate automatic segmentation algorithms, most of the previous works rely on a single frame segmentation from 4D flow MRI data. In addition, to reduce the effect of the low contrast of the magnitude images on the performance of the automatic segmentation, 4D flow-based MRA has been used. Although these approaches do not exploit the temporal information of 4D flow MRI, they have allowed the

evaluation of segmentation methods in these images and the analysis of the relationship between biomarkers such as wall shear stress and the evolution of aortic pathologies.

2.1.1.1/ REGION-BASED APPROACHES

To segment the aorta from 4D flow MRI, Hennemuth et al. [36] used a 4D flow based MRA image as input to a watershed transform-based algorithm. Here, the image is considered as a topological surface, in which high-intensity values (those belonging to regions with high flow) represent peaks and low intensities represent valleys. The algorithm is based on watershed identification and segmentation. Depending on the magnitude of the gradient, each pixel is assigned to a component in the segmentation, also called watershed. This algorithm requires seeds that are defined by a user inside or outside the object of interest. The watershed method may lead to an overestimation of the segmentation. Then, several regions may be generated as a part of the target segmentation.

Stalder et al. [41] implemented a segmentation algorithm based on unsupervised learning to contribute to the automatic visualization of 4D flow data. First, they calculated the phase contrast angiography, velocity magnitude, temporal standard deviation, and the spatial velocity gradient as features. After normalization, these features were used with a clustering algorithm to separate the voxels into three regions, lungs, static tissue, ventricles, and vessels such as the aorta. Although it is an automatic method, it does not allow for the differentiation of the vessel's wall.

2.1.1.2/ GRAPH-BASED APPROACHES

To improve the contrast of the magnitude image used for the segmentation, Kohler et al. [62] generated a temporal maximum intensity projection (tMIP) image by retrieving the maximum value per voxel along the temporal dimension. Then, they used the new 3D image to segment the aorta with a graph cut algorithm, considering regions marked by an expert as starting points. In this method, the number of points needed for a good segmentation performance is directly related to the quality of the image. Similarly, in [33], a graph cut was used to segment the carotid arteries, which arise from the aortic arch. In this case, a 4D flow -based MRA image was generated to calculate a center-line with points indicated by a user. Subsequently, the central line was taken as a starting point for a graph cut algorithm.

2.1.1.3/ MODEL-BASED APPROACHES

For the segmentation of large vessels, Van et al. [39] generated a temporal maximum velocity volume (tMSV) by taking the maximum blood flow velocity in each voxel. Unlike 4D flow-based MRA, only information from phase images is used in tMSV generation. An active surface model was used for segmentation, which requires an initial surface approximating the desired segmentation. The initial isosurface to initialize the algorithm was retreived by thresholding the generated tMSV image. In the segmentation process, the initial isosurface was adapted to the edge of the vessels by considering attractive forces. An attractor image was generated with features describing the boundaries between the vessels and the stationary tissue. This algorithm requires three parameters to be adjusted manually to control the balance of forces moving the isosurface.

Volonghi et al. [68] used only the phase images, previously filtered with an anisotropic diffusion filter. They initially generated 4D flow -based MRA image by calculating the magnitude of the velocity vector in the systolic phase. Using this image, they ran a marching cubes algorithm to generate an initial isosurface with a threshold equal to one-third of the maximum velocity. Finally, the extracted isosurface was used for level set-based segmentation.

Bergen et al. [47], applied the geodesic active contour algorithm for aortic segmentation. The input surface was generated by analyzing the behavior of the flow curve obtained for each voxel. Considering the mean and standard deviation of the distribution assumed as normal, thresholds were established to segment the voxels that meet the flow patterns within the aorta.

2.1.1.4/ DEEP LEARNING-BASED APPROACHES

The performance of deep learning models in medical image segmentation has recently enabled this approach to be explored with 4D flow MRI data. Deep learning segmentation is an end-to-end method where the model automatically learns image features to give each voxel a probability of belonging to the object of interest. Berhane et al. [90], a 3D U-Net network was used for aortic segmentation from 4D flow MRI data acquired from 1018 patients. The segmentation was generated from 3D 4D flow-based MRA previously computed for each patient. Similarly, 4D flow-based MRA images were also used in [104] to train an U-Net-based model to segment the aorta and pulmonary artery from 4D flow data from multiple centers. The effect of using data from multiple centers on segmentation performance was also examined. The performance of most segmentation methods has been evaluated by calculating flow-related parameters on a 2D plane, which makes a direct comparison between methods difficult. However, compared to the model-based method proposed by Volonghi et al. [68], both deep learning approaches outperformed it in term of the Dice overlap index.

2.1.2/ 4D SEGMENTATION OF THE AORTA FROM 4D FLOW MRI

The 4D segmentation of the aorta makes it possible to recover the position and shape of the aorta at each time step of the cardiac cycle. Moreover, 4D segmentation can be used to calculate biomarkers that describe blood flow interactions with the aortic wall throughout the cardiac cycle, eliminating the bias associated with the use of a 3D segmentation.

2.1.2.1/ GRAPH-BASED APPROACHES

Based on their previous work, Kohler et al. [85] initially generated a 3D segmentation in a tMIP image with a graph cut-based algorithm and user-input seeds. The resulting segmentation represents the moment of maximum aortic extension. For the propagation of the segmentation to the other time steps, they assume that the aortic diameter does not shrink more than 50% of its maximum value. Therefore, the voxels closest to the center line extracted from the 3D segmentation are considered to belong to the aorta for the algorithm's initialization. Graph cuts were executed independently for each time point.

2.1.2.2/ MODEL-BASED APPROACHES

Bustamante et al. initially proposed a segmentation based on one atlas [48] and then on multiple atlases [72], for the segmentation of the heart and large vessels. The atlas is composed of a set of images with their respective segmentation of the organs of interest. Initially, they computed a 4D flow-based MRA over the cardiac cycle for each patient in the database. For this purpose, a 4D flow-based MRA was generated independently for each time step. Then, a reference frame from the 4D flow MRI magnitude image was chosen to apply inter-patient registration with the remaining frames. The deformation applied to the magnitude images was propagated on the respective 4D flow-based MRA generated for each frame. With the result of this last step, a tMIP image was computed. Finally, to create the 4D flow-based MRA over the cardiac cycle, the inverse transform acquired in step one for each time step was applied on the tMIP.

In this work, images in the atlas were deformed to resemble the image of a new patient. Candidate segmentations were generated for the new patient by propagating the deformations to the corresponding segmentations. Finally, the new patient segmentation was computed by merging the candidate segmentations. Using this method, movement information between frames is preserved as long as the intra-patient registration is accurate.

2.1.2.3/ DEEP LEARNING-BASED APPROACHES

Bustamante et al. [102] have also proposed a 4D segmentation of the myocardium and great vessels from a 3D U-Net model. The segmentation was performed using the magnitude image as input to avoid biases related to the generation of images from 4D flow MRI (e.g. 4D flow-based MRA). Their previous segmentation work was based on multi atlases segmentation using 4D 4D flow-based MRA images. Perhaps the decision to use the magnitude image was based on the fact that 4D flow-based MRA images relays on the quality of the intra-patient registration. For the deep learning based approach, each time step of the cardiac cycle was treated as a training example. Thus, the network does not consider the temporal information and treats each frame as an independent image. In previous works on 3D segmentation, it has been shown that 3D neural networks outperform the 2D model-based segmentation strategy [86]. Therefore, the 4D segmentation approach based on a 3D strategy can be a baseline for comparison with 4D neural networks.

2.2/ SEGMENTATION PERFORMANCE EVALUATION METRICS

Metrics that measure the degree of agreement with an reference segmentation are required to evaluate the quality of automatic segmentations. The metrics provide information on the performance of the segmentation methods but are independent of the parameters calculated in clinical practice. Many metrics have been proposed to evaluate segmentation performance in medical imaging [79, 56]. Here we present two metrics widely used as quality criteria for automatic segmentation from 4D flow MRI.

2.2.1/ REGION OVERLAP

Metrics that measure overlap give global information on the quality of segmentation. The overlap indices are based on the four measures of a confusion matrix. In a confusion matrix, each column represents the number of predictions of each class, and each row shows the actual number of instances of each class (i.e. aorta and background). This matrix allows for identifying the number of hits and misses of the algorithm. Thus, the confusion matrix represents the number of true positives (TP), false positives (FP), true negatives (TN), and false negatives (FN). The overlap index between two segmentations A and B is known as the Dice similarity coefficients (DSC) [56] and is calculated with the equation 2.1.

$$DSC(A,B) = 2 * \frac{A \bigcap B}{|A| + |B|} = 2 * \frac{TP}{2TP + FP + FN} \tag{2.1}$$

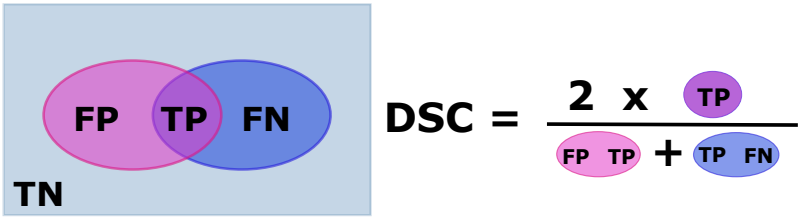

Figure 2.1: Representation of Dice similarity coefficient. TP represents the number of true positives predictions, FP and FN the number of false positives and false negatives, respectively

2.2.2/ SPATIAL DISTANCE BETWEEN CONTOURS

Metrics based on the measurement of the spatial distance between two segmentations provide information about the error on contours. The Hausdorff distance measures the maximum distance from each point in segmentation A to the closest point in segmentation B [53]. In the case of two finite point sets $A = [a_1, ...a_p]$ y $B = [b_1, ...b_p]$, the Hausdorff distance HD is defined as follows:

$$HD(A, B) = max(h(A, B), h(B, A)) \tag{2.2}$$

where

$$h(A, B) = \max_{a \in A} \min_{b \in B} ||a - b|| \tag{2.3}$$

and $||\cdot||$ is a measure of distance as the Euclidean distance. Thus, the function $h(A, B)$ identifies the point a farthest from any point of B. Then, it measures the distance from a to its nearest neighbor in B [3].

2.3/ FUNDAMENTALS OF THE METHODS USED FOR AUTOMATIC SEGMENTATION

2.3.1/ MULTI-ATLAS-BASED SEGMENTATION FUNDAMENTALS

MAS's objective is to apply transformations to establish a spatial correspondence between the image P to be segmented and a group of N ($N \in \mathbb{N}^*$) images called atlases. An atlas comprises a gray intensity image A_i and the image A_i^s (i=1, 2, ..., N) with the corresponding segmentation of the organ of interest. To infer the label of a voxel in P, a transformation T_i is first applied to deform the image A_i in the atlas and align it with P image coordinate space. Subsequently, the respective T_i transformation is applied to the associated A_i^s segmentation. Several candidate

segmentations C_i^s are generated for P by performing the previous process with all the images in the atlas ($C_i^s = A_i^s \circ T_i$ $(i \in 1, 2, 3, ...N)$). During the registration, the alignment quality is measured with a similarity measure S based on corresponding landmarks or the intensity of the images to be registered [50]. The registration problem is presented as an optimization problem in which a cost function C must be minimized (Equations 2.4 and 2.5).

$$\hat{T}_i = \underset{T_i}{arg\,min}\, C(T_i; P, A_i) \tag{2.4}$$

$$C(T_i; P, A_i) = -S(T_i; P, A_i) + \gamma R(T_i) \tag{2.5}$$

where R is a regularization term that constrains T_i and γ weighs similarity against regularity.

With MAS-based methods, the segmentation performance is directly related to the ability of the registration process to properly map the images. Therefore, it is essential to select the best parameters for the transformation considering the segmentation task and the imaging modality used.

The next step in the segmentation process is to merge the candidate segmentations C_i^s to generate a single target segmentation. The deformed image of the atlas most similar to P can be choose as the target segmentation. However, the merging process aims to include anatomical diversity by taking information from several candidate segmentations. The label fusion process can be performed with voting-based methods. Voting can be performed by giving equal relevance [18] to all candidate segmentations or assigning a global [24] or local weight [29] associated with the registration quality. Additionally, a family of probabilistic fusion methods has been proposed to incorporate prior expectations in the label fusion process [34, 14]. As a previous step to label fusion, selecting the candidate segmentations to be merged could be performed. The objective is to identify the atlases most similar to P after registration and avoid misguiding the fusion algorithm.

2.3.2/ DEEP LEARNING FUNDAMENTALS

Machine learning is a branch of artificial intelligence in which algorithms learn from data. Formally, the algorithm learns from experience E with respect to task T, such that the performance P improves with experience [6]. Machine learning algorithms can be supervised or unsupervised, which means that the algorithm may or may not require previously labeled data. Deep learning is a group of machine learning algorithms based on neural networks. Several tasks T can be addressed with deep learning, including image segmentation. The general goal of deep learning is to find a function f_M that solves the particular task. This function is also called model. In practice, the supervised model takes an input x and

generates a prediction $\hat{y} = f_M(x)$. So, the function f_M should approximate the prediction with the target y.

During the process, measuring the performance P_M that indicates how well the algorithm solves the task is necessary. Then, the performance of the model can be evaluated with a cost function J that takes the predictions $\hat{y}$ and the targets y (Equation 2.6) of the inputs.

$$P_M = J(y, \hat{y}) \tag{2.6}$$

Experience E is used to train the model. In supervised deep learning, the experience is a dataset of N_{train} examples with a respective target value, $X_{train} = \{(x_1, y_1), \cdots, (x_m, y_m)\}$. The deep learning model is trained to solve the task T, parameterized with weights ω_M. Then, the optimization problem is given by the equation 2.7.

$$\omega_M^* = \underset{\omega_M}{arg\,min} \sum_{i=1}^{N_{train}} J(y_i, f_M(x_i, \omega_M, h_m)) \tag{2.7}$$

where h_m are the hyperparameters of the model.

In the deep learning model design, the hyperparameters h_m are the ones that define, for example, the size of the input data or weights that are included in the cost function J to regulate the ability of the model to fit the data. The hyperparameters can be fixed by employing an optimization process. However, this increases the computational requirements. To overcome this problem, search ranges are set for each parameter, or according to previous experience, fixed parameters are chosen.

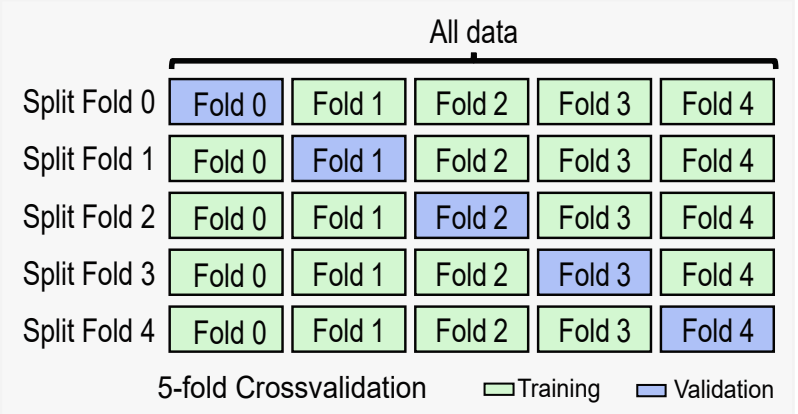

Figure 2.2: Representation of a 5-fold cross validation process

2.3.2.1/ MODEL TRAINING STRATEGIES

The objective is to produce a model with high performance on examples not seen during training, i.e. a model that generalizes well. The model's generalization capability is measured by generating predictions in a validation set X_{val} and a test set X_{test}.

The validation examples ($X_{val} \nsubseteq X_{train}$) are used to set the hyperparameters h_M. The test set ($X_{test} \nsubseteq X_{train}$ and $X_{test} \nsubseteq X_{val}$) is used to evaluate the performance of the algorithm. Although the performance of the model in X_{train} does not give information on the generalization capability, it is important because it shows whether the optimization allows the model to learn the task.

In clinical applications, access to data is limited, so datasets usually have few examples. In these cases, the selection of X_{train}, X_{val}, and X_{test} should not be random because it could lead to bias. To deal with short databases, a validation technique called cross-validation (CV) has been proposed. With CV, the database is divided into k-folds. Then, k deep learning models are trained by changing the data taken as training and validation (Figure 2.2). Unlike methods such as MAS, which can be implemented with a single patient in the atlas, the performance of machine learning algorithms is related to the number of training samples. Then, if the size of the database allows having testing data, these are isolated from the training process. When the number of k equals the number of samples in the database, the k-fold CV is called leave-one-out.

During the training of a machine learning model, the bias-variance trade-off should be followed to analyze the expected generalization error (Figure 2.3). Bias is the error that represents the model's inability to learn the relationship between the features and the target (underfitting). Variance is an error associated with the model's sensitivity to small fluctuations in the training data. Thus, the variance represents an over-fit of the model to the training examples.

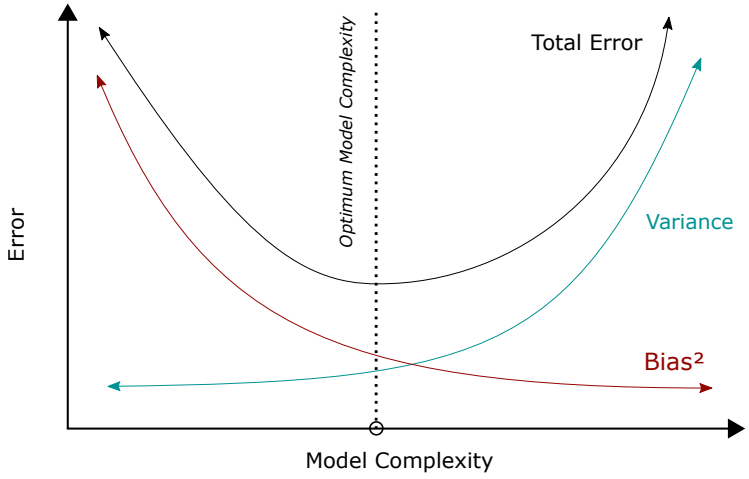

Figure 2.3: Bias and variance in machine learning models

2.3.2.2/ NEURAL NETWORKS

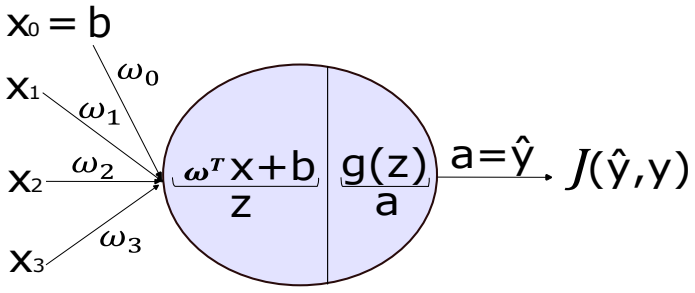

Figure 2.4: One neuron internal process. Where X represents the inputs, y the ground truth, ω the weights, b the bias, g the activation function, $\hat{y}$ the output, J the cost function.

Neural networks are algorithms containing units, known as neurons, that are interconnected to share information in a learning process. Each neuron receives one or more weighted inputs. An extra input with a value equal to one is added and is known as bias. The output of the neuron is called activation and is generated by evaluating the sum of the weighted inputs with a function g (Figure 2.4).

Weights and biases are trainable parameters. The weights determine the contribution of each input to the output. The biases determine in what proportion the output will be offset from the input. The activation function provides a signal indicating the neuron activation level. Nonlinear activation functions allow the model to learn complex representations to solve nonlinear problems. Commonly used activation functions are sigmoid or logistic, hyperbolic tangent (*tanh*), and Rectified Linear Unit (*ReLU*) (Figure 2.5).

There are three main types of neural networks: feedforward neural networks, convolutional neural networks, and recurrent neural networks. The fundamentals of the first two kinds of neural networks are presented below, considering they are related to the deep learning models implemented in this thesis.

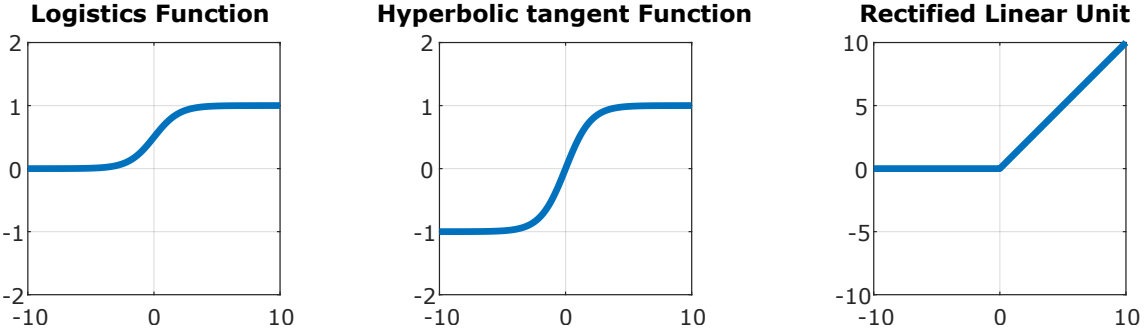

Figure 2.5: Examples of activation functions

2.3.2.3/ FULLY-CONNECTED NEURAL NETWORK

Feedforward or fully-connected neural network (FC-NN) are the simplest type of neural network and are the basis of advanced neural networks such as convolutional neural networks. FC-NNs are composed of several artificial neurons stacked together to form what is known as a single neural network layer. The neural network can be extended by adding layers, which generally increases the performance of the model. However, depending on the application, a model with many layers can lead to overfitting, resulting in poor performance on unknown data. The layers between input and output are called hidden layers. As the name suggests, in a FC-NN the neurons of each hidden layer are fully connected with the neurons of the previous layer and with those of the next layer (Figure 2.6). The input data is received and processed in each hidden layer based on the activation function. Finally, the activation is transferred to the next layer. For output to be generated, input data must only be fed forward.

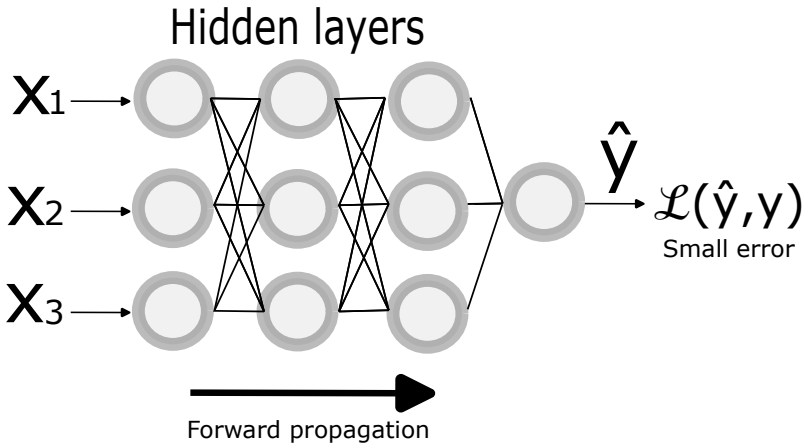

Figure 2.6: Representation of a fully-connected neural network

The neural networks are trained from the output generated in the forward by using the backpropagation algorithm [4]. To perform backpropagation, three essential tools are requested: a cost function, an optimization algorithm, and a learning rate (Figure 2.7). The cost function measures how far the actual output is from the target output. It measures the error when the network weights and biases are updated. The optimization algorithm finds the minimum value of the cost function. The most commonly used algorithm is gradient descent [66]. The learning rate controls how fast the model adapts to the problem; it indicates in what proportion the weights and biases are updated.

2.3.2.4/ CONVOLUTIONAL NEURAL NETWORKS

Convolutional neural networks (CNN) are an adaptation of FC-NNs for image processing. In the latter, the input data is a one-dimensional vector $X = \{x_1, x_2, ..., x_m\}$, and each value in the vector is connected to a neuron with an individual weight.

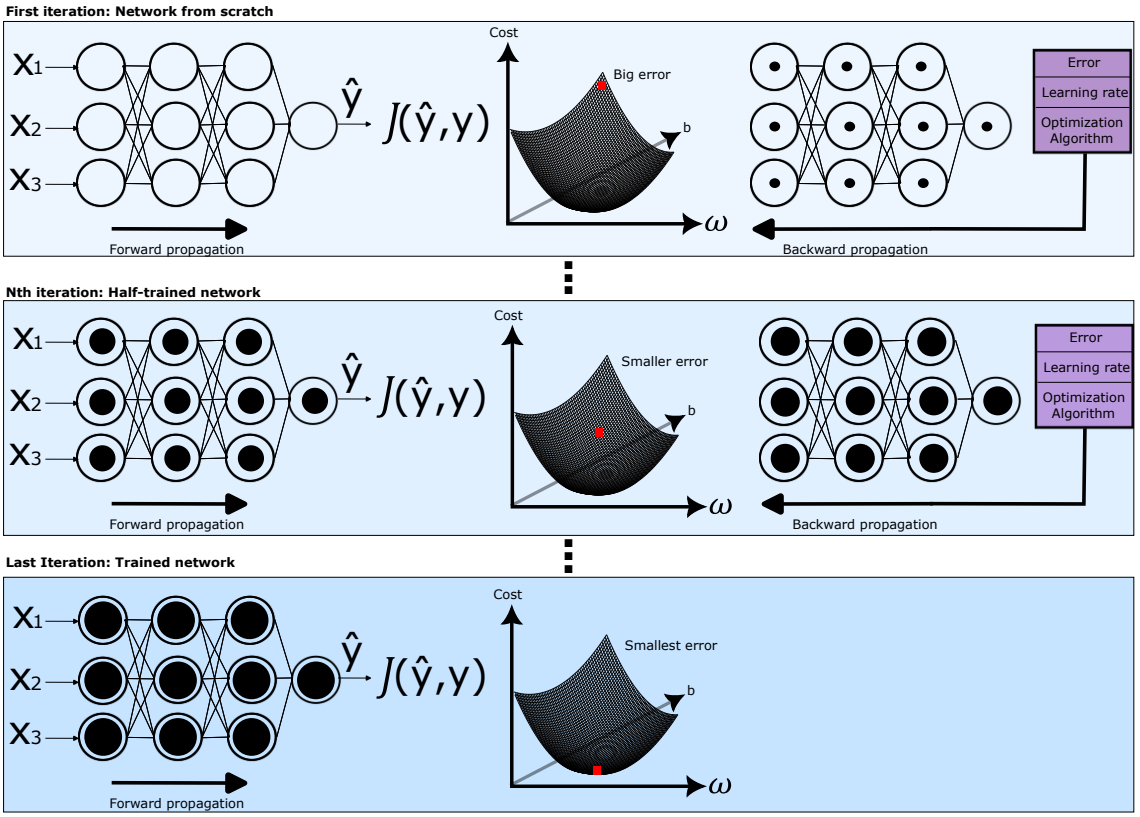

Figure 2.7: Neural network learning process. The black color inside the neurons indicates the level of knowledge about the context of the task.

If the input is a 2D or a 3D image, millions of weights are optimized, which is computationally expensive and can lead to overfitting.

To avoid these problems, in a CNN, the neurons have only a small receptive field $v \in \mathbb{R}^{k_1 \text{ x } k_2 \text{ x} \cdots \text{x } k_n}$. Therefore, they are connected to only a part of the input image. Parameters sharing among all neurons in a layer is enforced. Thus all the receptive fields v share the same parameters $K \in \mathbb{R}^{k_1 \text{ x } k_2 \text{ x} \cdots \text{x } k_n}$. The objective of this process is to reduce the number of parameters while learning the same type of features in each region of the image. Thus, instead of multiplying each value of the input with a matrix of weights ω, in CNN the operation can be imaged as the kernel K sliding over the image and performing a convolution operation. In classical image processing, kernels (also known as filters) are applied to enhance or smooth image characteristics. In this classic way, the kernels used are based on experience and knowledge of the particular task. In CNN, kernels are automatically learned from the data. A convolutional layer l receives as input a tensor $X^{l-1} \in \mathbb{R}^{d_1 \text{ x } d_2 \text{ x} \cdots \text{x } d_n \text{ x } n_c^{l-1}}$ from the preceding layer, where n_c represents the number of input channels. Then a kernel $K \in \mathbb{R}^{k_1 \text{ x } k_2 \text{ x} \cdots \text{x } k_n \text{ x } k_c^l}$ is used to produce k_c^l feature maps. Thus, The output of layer l is given by the tensor $X^l \in \mathbb{R}^{d_1 \text{ x } d_2 \text{ x} \cdots \text{x } d_n \text{ x } n_c^l}$ with $n_c^l = k_c^l$. To generalize the output of each convolutional layer, $k_c^l n_c^{l-1}$ individual convolutions are performed.

The n-dimensional convolution is denoted by equation 2.8, where $(q_1, \cdots, q_n)$ is

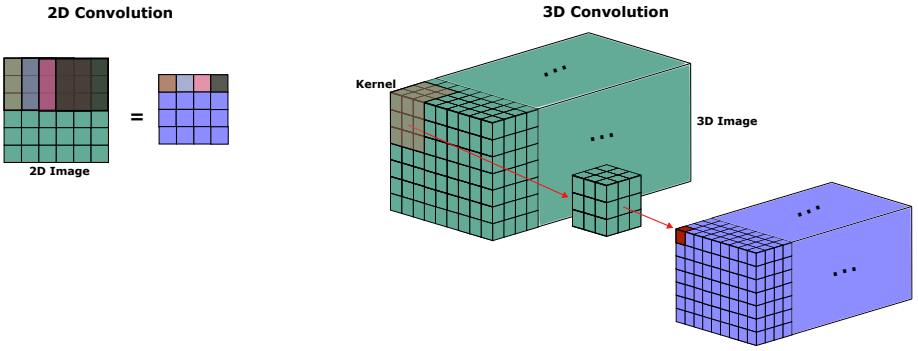

Figure 2.8: Convolution process

the location of a respective receptive field $v_{q_1,q_2,\cdots,q_n}$. If not all receptive fields are operated, a convolutional layer with strides is obtained by considering only on the $v_{r_1q_1,r_2q_2,\cdots,r_nq_n}$ positions. r are integers representing the magnitude of the stride in the respective dimension.

$$(K * X)(q_1, \cdots, q_n) := \sum_{i_1} \cdots \sum_{i_n} K(i_1, \cdots, i_n) \text{ X } (q_1 - i_1, \cdots, q_n - i_n) \tag{2.8}$$

Equation 2.9 is considered to calculate the size of each of the output dimensions of a convolutional layer.

$$d_{out\_axis} = \frac{d_{input\_axis} - d_{k\_axis}}{r\_axis} + 1 \tag{2.9}$$

where d_{input_axis} and d_{k_axis} denote the size of the image and kernel in the desired dimension. r_axis is the applied stride applied over the considered dimension.

2.3.2.5/ DEEP LEARNING-BASED SEGMENTATION FOR MEDICAL IMAGES

Segmentation based on deep learning consists of building a model, usually of convolutional type (CNN) [78]. This model is trained to extract low and high-level features from the images and produce the probability for each voxel to be part of the organ to be segmented. Globally, a convolutional network comprises convolution, pooling, and fully connected layers. The convolution layers are responsible for extracting features by convolving kernels with the input data. The output of a convolutional layer is considered an activation map that highlights the effect of a filter applied to the input. In a CNN model, this layer is followed by an activation function that applies non-linearity to the activation map. Generally, pooling layers can be added between the convolution layers to reduce the output size. The features computed through these layers are inputs to fully connected layers to perform a high-level abstraction and prediction of the class to which each pixel belongs, i.e. organs of interest or background [84].

One of the widely known models used in the field of medical image segmentation is called U-Net [54]. This model is composed of two paths, one for analysis and one for synthesis, known as encoder and decoder, respectively. The encoder path follows the structure of a CNN, so it is composed of convolutional and pooling layers that spatially contract the image while capturing the contextual information. The decoder path allows a precise location reconstruction by expanding the output to recover a full-resolution segmentation probability map. Shortcut connections between the layers of equal resolution in the encoder path and the decoder path are one of the essential properties of U-Net. The expansion layers benefit from the high-resolution features transferred by these shortcut connections [57].

2.4/ CONCLUSION

For the generation of hemodynamic biomarkers from 4D flow MRI, one of the challenges to be addressed is the segmentation of the region of interest. In our case, segmentation of the aorta is essential to delimit the information and the region of fluid-structure analysis. Manual segmentation not feasible in clinical practice because it is time-consuming, especially in a 4D sequence. Moreover, it is prone to inter- and intra-observer variability. Thus, it is essential to address this problem to expand the use of 4D flow MRI in the study of aortic pathologies.

In this chapter, we reviewed the segmentation methods available in the state of the art to delineate the aorta from 4D flow MRI. Most of the proposed methods focus on 3D aortic segmentation. Moreover, to improve the contrast of the aorta with the background, they generate images such as 4d flow-based MRA. However, these pre-processing methods do not provide reliable information about the position of the aorta in each cardiac cycle phase.

Inspired by the possibilities and weaknesses of methods from state-of-the-art for automatic aortic segmentation from 4D flow MRI, we show in the upcoming chapters our contributions in 3D and 4D aortic segmentation using a home built database of patients with thoracic aortic aneurysm. In our work, we approach the automatic segmentation using the magnitude image from 4D flow to avoid the biases inherent to 4D flow based MRA generation.

II

CONTRIBUTION

3

DATASET

In this chapter we present the studied population from which the 4D flow MRI images were acquired. Subsequently, the parameters established for acquiring the images and the details about manual segmentations are provided. The identification of the systolic and diastolic phases is necessary for multiple analyses. Therefore, this chapter also introduces the process of identifying the time steps corresponding to these phases.

3.1/ POPULATION

The population included in this work belongs to the research project MECATHOR 2018-A02010-55, developed in the University Hospital of Dijon, France. This study was approved by the French national ethics committee and is registered on ClinicalTrials.gov. After receiving written information about the study, each subject underwent a 4D flow MRI.

Among the included population in the MECATHOR project, 36 4D flow MRIs were used in this thesis to implement and evaluate the automatic aortic segmentation algorithms (Table 3.1). The study cohort consisted of subjects with an average age of 60 years and with an aneurysm at the level of the ascending aorta. Twenty six of the 36 patients were men, and ten were women. Furthermore, 13 men and five women had BAV.

3.2/ IMAGING PROTOCOL

The patients in the database presented an aneurysm at the level of the ascending aorta. Therefore, 4D flow MRI acquisition targeted the thoracic aorta. The acquisitions were performed on a 3 Tesla Siemens scanner (Siemens Healthineers, Erlangen, Germany) with a phased thoracic coil. The complete MRI protocol for the study of thoracic aneurysms consists of several sequences. Initially, cine-MRI is acquired, followed by 2D flow MRI in the x, y, and z directions. After the ECG-

Table 3.1: Patients characteristics. TAV and BAV refer to tricuspid and bicuspid aortic valves, respectively.

Patient	Sex	Age	Valve type	Max diameter
1	M	68	BAV	50
2	M	59	BAV	51
3	F	78	TAV	54
4	M	40	BAV	45
5	M	71	BAV	53
6	M	44	TAV	54
7	M	70	TAV	50
8	M	43	BAV	52
9	M	68	TAV	53
10	M	68	BAV	50
11	M	74	TAV	51
12	F	37	BAV	49
13	F	67	TAV	46
14	F	64	BAV	42
15	M	72	BAV	46
16	M	72	TAV	57
17	F	51	BAV	58
18	M	72	TAV	49
19	M	79	BAV	47
20	M	37	BAV	47
21	F	26	TAV	53
22	M	59	TAV	55
23	F	74	TAV	46
24	M	52	BAV	52
25	M	75	BAV	46
26	M	72	TAV	54
27	M	72	TAV	55
28	F	39	BAV	51
29	F	65	TAV	54
30	F	74	BAV	47
31	M	66	BAV	47
32	M	68	TAV	54
33	M	74	TAV	56
34	M	72	BAV	51
35	M	40	TAV	52
36	M	64	TAV	50

triggered MRA with gadolinium as a contrast agent, the 4D flow MRI is acquired. In the following, we provide the parameters of the sequences used in this thesis.

The 2D cine-MRI sequence was of Fast Low Angle type. The acquisition was

performed during breath-hold in a plane perpendicular to the aorta at the level of the pulmonary trunk. From this sequence, 35 phases of the cardiac cycle were acquired with a temporal resolution between 20 and 34 ms. The spatial resolution was set between 1.25x1.25 and 1.9x1.9 mm^2. The echo and repetition time were equal to 3.42 and 34 ms, respectively.

4D flow MRI was acquired after the acquisition of an MRI angiography with the injection of Gadolinium contrast agent. All 36 subjects underwent our 4D flow MRI protocol, in which the acquired volume covers the thoracic and the proximal abdominal aorta in a sagittal-oblique orientation. The parameters established were: Venc between 200 and 800 cm/s, a spatial resolution of 2x2x2 mm^3, and temporal resolution of 24-52 ms to generate 25 cardiac phase with retrospective gating. In addition, echo and repetition time were set between 2.1-2.3 ms and 38.5-40 ms, respectively. The acquisition was performed during free breathing with ECG and respiratory gating. The duration of the scan was 10-15 minutes for the 4D flow MRI acquisition.

3.3/ SYSTOLE AND DIASTOLE IDENTIFICATION

In 4D flow MRI analysis, identifying the different cardiac phases is essential because it allows the calculation of metrics and the localization of the time steps to be analyzed.

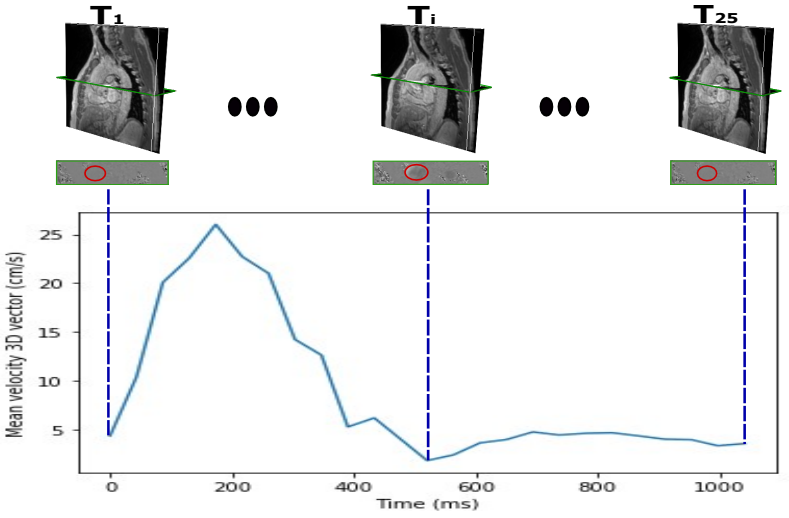

Figure 3.1: Representation of cardiac phase identification by locating a plane at the level of the ascending aorta at each time step. The average velocity vector in the extracted plane is calculated to identify the times with the maximum and minimum velocity, corresponding to systoles and diastole, respectively.

To identify the systolic and diastolic phases for each patient, we started with the manual identification of a 2D plane perpendicular to the ascending aorta. For each time step, the 2D plane is localized at the same position. Subsequently,

the ascending aorta is manually segmented in the generated 2D+time images. Finally, using the components of the velocity vectors provided in the phase images (according to the x, y, and z directions), the average norm of the vectors at each time step is calculated. For each patient, an average velocity evolution curve over the time is obtained, which allows for locating the maximum (systole) and minimum (diastole) average velocity in the cardiac cycle (Figure 3.1).

Before computing the average norm of the vectors to identify the cardiac phases, the phase images containing gray intensity information are processed to find the corresponding velocity value for each voxel. The relationship between the minimum and maximum velocities and intensities is linear and is given by the equation 3.1. Then, as can be seen in the Figure 3.2 the slope m of the line was calculated to perform the linear scaling to convert the intensity values from phase images to velocity. The maximum and minimum velocity values correspond to Venc and -Venc, respectively. The minimum and maximum intensity values were retrieved with the following Dicom tags: Rescale intercept, Rescale slop, and stored bits.

$$velocity = m * sv \tag{3.1}$$

where sv is the stored value.

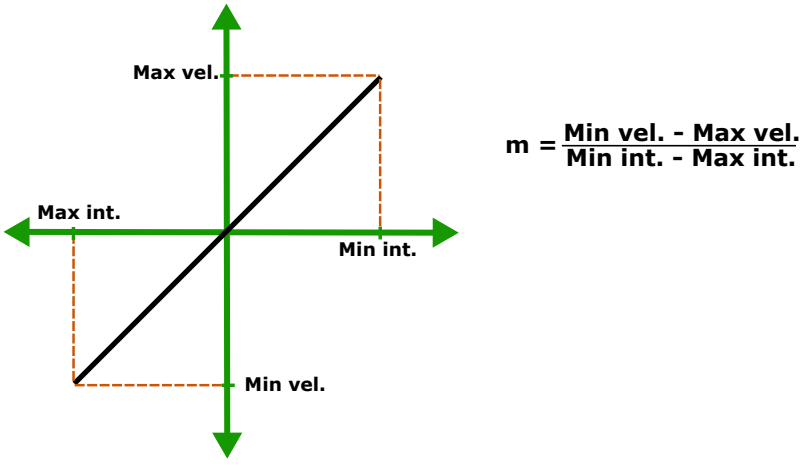

Figure 3.2: Slope m of the line representing the linear relationship between a gray intensity value and velocity in phase images.

3.4/ MANUAL LABELLING

For the implementation and performance evaluation of the algorithms used in this thesis, reference segmentations were generated manually for the 36 patients. ITK-SNAP software [19] was used for this purpose.

The segmentation of the aorta from 4D flow involves several challenges, between them, the definition of the shape of the valve and of the vessels that arise in the

aortic arch: brachiocephalic artery (BA), left common carotid artery (LCCA) and left subclavian artery (LSA). In this regard, two rules were established for manual segmentation. First, the arteries mentioned above were not included because it is very complicated to accurately identify their boundaries. Second, at the level of the valve, a plane perpendicular to the direction of the valve at the level of the aortic sinuses was considered because it is difficult and questionable to establish the exact or approximate shape in 3D (Figure. 3.3).

In order to perform both global and local evaluation of the automatic segmentation performance, the aorta was thereafter divided into three regions: ascending aorta with the aortic arch (AAo+Arch), TDAo and proximal abdominal aorta (PAAo). The ascending aorta and the arch are considered as a single region since it was no possible to identify the beginning of the BA as a landmark to establish the beginning of the arch.

For the implementation of automatic algorithms for 3D segmentation, two image analysts segmented blindly a frame corresponding to the systolic phase for each patient. The manual segmentation of each frame took an average of 3.5 hours. Subsequently, a probabilistic estimate of the true segmentation was generated using the STAPLE (simultaneous truth and performance level estimation) algorithm [14]. The resulting segmentation was used for implementing the 3D algorithms but also to evaluate the inter-operator variability.

Since manual segmentation is time-consuming, for the implementation of 4D segmentation algorithms, only one of the image analysts completed a total of five manually segmented frames for each patient. For this purpose, the first time step was segmented for each patient since it is a frame corresponding to the end of diastole. After, we considered the respective frame in systole phase per each patient. The remaining three frames were taken from time steps 15, 20, and 25 to have a relatively constant distribution over the cardiac cycle. For these last three frames, the previously segmented diastole was taken as a reference to initiate segmentation. This was done to reduce the time required for manual segmentation by refining the initial segmentation. Both 3D and 4D segmentations were reviewed by a clinical expert.

3.5/ DISCUSSION

This chapter presented the database constructed for implementing and validating automatic segmentation methods of the aorta with thoracic aneurysms. The cohort of patients and the standards followed for the manual segmentation of the magnitude image were described. To deal with challenges in aortic segmentation, the manual segmentation was performed without including the brachiocephalic trunk, and a flat segmentation was drawn at the level of the aortic valve sinuses due to the difficulty in accurately defining the 3D shape.

In contrast to what was proposed by [36, 39, 68, 72] using the magnitude images

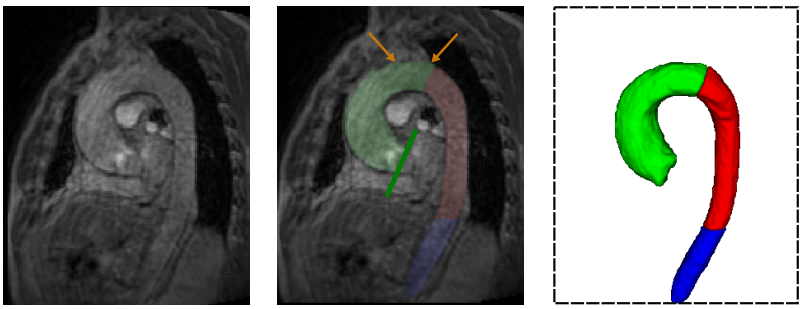

Figure 3.3: In **a)** a slice of the raw image for a patient is presented. In **b)** the manual segmentation of the raw image is displayed, which does not include the brachiocephalic arteries located in the position indicated with the yellow arrows. The green line represents the plane perpendicular to the valve inlet, used to denote the beginning of segmentation at this level. **(c)** shows the 3D rendering of the segmentation.

allowed us to avoid the biases included in the segmentation from new images generated from 4D flow MRI.

At present, fully automatic segmentation from 4D flow MRI magnitude images has been addressed only by Bustamante et al. [102] However, the reference segmentations were generated with an automatic algorithm based on multiple atlases. In our case, the segmentations were completely manual, reflecting what the image analyst considered from the beginning as the aorta or background and avoiding transferring possible errors from the automatically generated references to the different segmentation algorithms evaluated. Among the 36 patients, a total of 180 frames were manually segmented, which is important given the unavailability of databases with annotations of the aorta from 4D flow MRI.

4

3D SEGMENTATION OF THE AORTA FROM 4D FLOW MRI

This chapter focuses on the methods and pipelines implemented for segmenting the aorta in the systolic phase from 4D flow MRI. Most of the previously proposed aortic segmentation methods are implemented using 3D images generated from 4D flow MRI. Unlike these approaches, we evaluated the performance in aortic segmentation from magnitude images. For this purpose, we used two fully automatic methods with the potential to be implemented later in 4D. In particular, a multi-atlas-based method and a deep learning-based method were explored. For each method we showed a detailed evaluation with respect to segmentation metrics and a biomarker based on computational fluid dynamics. Thus, an evaluation of segmentation performance using DSC and HD is provided. Then, the aortic wall pressure was obtained from a manual segmentation and compared to those obtained from each automatic model. From these results, we aimed to define the type of algorithm to be used for segmenting the aorta over the entire cardiac cycle.

4.1/ ALGORITHMS TRAINING AND VALIDATION

The segmentations with multi-atlas-based and deep learning-based methods were carried out by applying the leave-one-patient-out strategy. Thus, to segment one patient with the multi-atlas method, the delineated images of the remaining ones were used as atlases. For deep learning, the same images were used for training, and the patient to be segmented for validation. Leave-one-out is not a validation technique used in large databases due to the increased computation time. However, since our database is small, we can take advantage of the potential of this method to train the models with as many training examples as possible and reduce the bias in the result by learning the diversity of the database. The degree of agreement of each algorithm with manual segmentation was measured with DSC and HD. Moreover, the metrics were evaluated globally and locally in the regions established during manual segmentation (i.e., AAo+Arch, TDAo, and PAAo) to identify error-prone regions during automatic segmentation.

4.2/ Pre-processing and post-processing for segmentation Algorithms

Before training the algorithms, the magnitude images were normalized independently between 0 and 1. Automatic segmentations from multi-atlas-based and deep learning-based methods were post-processed. First, the largest connected component was identified and selected as the aorta segmentation. Then, we used a morphological opening filter to smooth out irregularities. A ball structuring element of radius 3 mm was used.

Figure 4.1 shows the before and after post-processing applied for one patient in the segmentations generated with deep learning and multi-atlas-based segmentation.

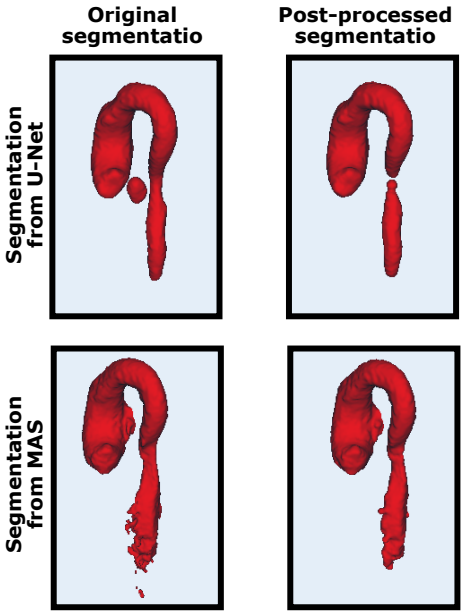

Figure 4.1: Example of the postprocessing result on the segmentation from U-Net and MAS for the same patient.

4.3/ Multi-atlas-based segmentation

The multi-atlas-based segmentation method (MAS) has been successfully used in medical imaging for different segmentation tasks. Bustamante et al. [72] previously evaluated this algorithm for heart and thoracic vessel segmentation but on PCMRA images generated from 4D flow MRI. This method was selected since it presented encouraging results in aortic segmentation from PCMRA and because the nature of the technique makes it feasible for use in small datasets. We evaluated MAS on the segmentation of the aorta in the systolic phase from the 4D flow MRI magnitude image. Bustamante et al. [72, 48] presented the results of

the method concerning the stroke volume or net flow calculated in a 2D plane at the level of the ascending aorta. In our work, we present a 3D evaluation of global and local performance concerning DSC and HD. Moreover, we compared the maximum diameters of the aorta obtained from automatic and manual segmentations.

4.3.1/ MULTI-ATLAS-BASED SEGMENTATION SETUP

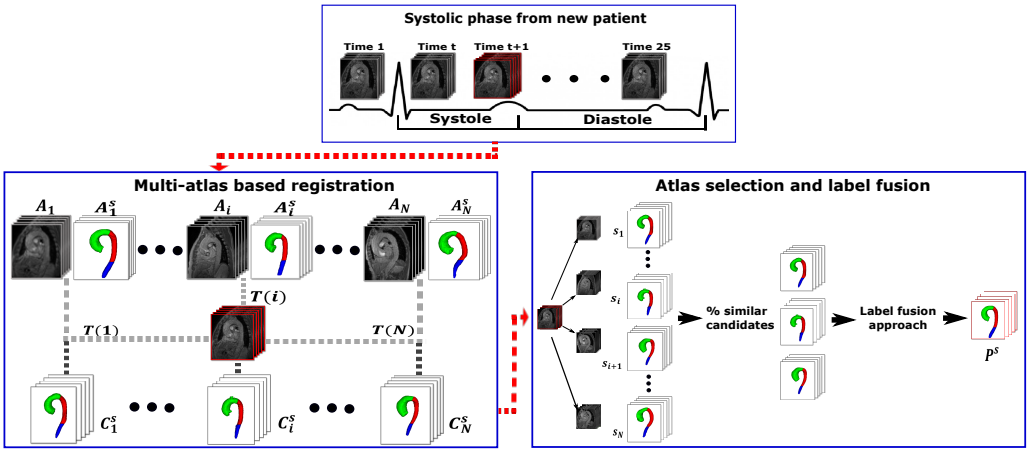

Figure 4.2: Pipeline of the multi-atlas-based method to segment the aorta in the systolic phase from 4D flow MRI. The images A_i in the atlas are mapped to the target image P (highlighted in red) with a transform T_i to produce candidate segmentations C_i^s that are merged after a Candidate segmentation selection process to generate the target segmentation P^s.

Automatic segmentation of the aorta in the systolic phase from 4D flow MRI was generated with MAS for 32 patients. For the registration process, affine and B-spline transformations were used to first map linearly P to A_i and then apply local deformations for a better spatial alignment.

The affine and B-spline registration best hyper-parameters were identified with an exhaustive search. The tested affine parameters were the type of image pyramids (Gaussian pyramid or Gaussian scale space), the number of pyramid resolutions (from one to four), and the similarity metrics used in the cost function (normalized correlation coefficient, mean squared difference, mutual information, and normalized mutual information). For the mutual information metric, 16, 32 and 64 number of bins were tested to compute the histograms. In total, 64 affine registrations were carried out per patient. The search for the best B-spline parameters was based on the optimization of the grid spacing value which is the most important parameter because it controls the flexibility of the local deformations. We varied this parameter from 10 mm to 46 mm with a step of 6 mm in each dimension independently. For the other registration parameters, we used a Gaussian pyramid with three resolutions and the normalized correlation coefficient as similarity measure. In total, 343 B-spline registrations were carried out per patient.

The 64 affine registration tests were initially run with the different hyper-parameter sets. Then, MV was used for label fusion without atlas selection to determine the best hyper-parameters set. The best hyper-parameters were the ones that provided the best average performance with respect to DSC and HD. The different parameter sets for the B-spline transformation were evaluated on the images resulting from the affine deformation with the respective best hyper-parameters. As for affine registration, the best hyper-parameters for B-spline transformation were identified considering the average DSC and HD in the database when using MV as the label fusion method. The registrations were performed using the Elastix software version 5.0 [30].

In the proposed registration pipeline (Figure 4.2), structural similarity index (SSI) [13] was used to select the candidates segmentations before performing the label fusion. The SSIM index provides a value between 0 and 1, where 1 indicates perfect structural similarity between two identical sets of data and 0 indicates no structural similarity.

Considering the SSI value between the deformed image $(A_i \circ T_i)$ and P, the inclusion criterion in the equation 4.1 was established to select the segmentations to be fused.

$$\{C_i^s, \forall i \in 1, ..., N, SSI(P, A_i \circ T_i) > (max(SSI_T) - min(SSI_T)) * d + min(SSI_T)\} \tag{4.1}$$

where d is a number between 0 and 1 that indicates the percentage of atlases with the lowest SSI to be discarded and SSI_T is the group of similarity metrics measured between P and the N deformed images.

The three label fusion methods evaluated in this thesis for the MAS-based segmentation pipeline were Majority voting (MV), Weighted majority voting (WMV) and Patch weighted majority voting (PWMV). The global or local SSIs between the deformed images and P were used in the fusion algorithms that require a weight, i.e., WMV and PWMV.

Majority voting: Majority voting is the most straightforward label fusion method and uses a global strategy giving to all candidate segmentations the same relevance. For the target segmentation P^s, the most frequent label l ($l = 1, ...L$, with L = number of labels) is assigned to each voxel x, such as

$$P^s(x) = \underset{l \in 1,...,L}{arg\ max}\ p_l(x) \tag{4.2}$$

where $p_l(x) = \frac{1}{N} \sum_{i=1}^{N} O_{i,l}(x)$ with $O_{i,l}(x) = 1$ if $C_i^s(x) = l$ and 0, otherwise.

Weighted majority voting: Weighted majority voting uses a global weight w_i proportional to the similarity measure between $A_i \circ T_i$ and P, to calculate the probability of a voxel x to be the label l as follows

$$p_l(x) = \frac{\sum_i^N w_i \cdot \delta[l, C_i^s(x)]}{\sum_i^N w_i}, \quad \forall\ l \in L \tag{4.3}$$

where $\delta[\cdot]$ is the Kronecker delta function. The segmentation P^s is then generated with Eq. 4.2.

Patch weighted majority voting: Patch weighted majority voting is a local extension of WMV, where a different weight is assigned to each voxel x. This weight is proportional to a similarity measure calculated between a patch or kernel (a kernel size of 11x11x11 was used in this work) centered on the voxel x of P and a patch of the same size and at the same position in $A_i \circ T_i$.

4.3.2/ MULTI-ATLAS-BASED SEGMENTATION EVALUATION

Segmentation performance was measured locally and globally using DSC and HD. In order to evaluate the reliability of the automatic segmentation, the statistical significance of the differences in the maximum diameter between manual and automatic segmentations was assessed. The Vascular Modeling Toolkit (VMTK) was used to calculate the diameter. VMTK extracts the centerline from the aortic valve to the abdominal aorta and measures the aortic diameter using normal planes at each centerline segment. For the analysis, a t-test was applied after checking the normality of the two groups with the Shapiro–Wilk test. The correlation and agreement between the diameter obtained with manual and automatic segmentations were also computed.

4.3.3/ MULTI-ATLAS-BASED SEGMENTATION RESULTS

Table 4.1: Average performance of MAS method on 32 patients with the best set of parameter and leave-one-patient-out strategy

Method	AAo+Arch		TDAo		PAAo		Full aorta	
	DSC	HD [mm]	DSC	HD [mm]	DSC	HD [mm]	DSC	HD [mm]
MAS	0.88 ± 0.04	18.21 ± 7.68	0.90 ± 0.034	7.43 ± 2.64	0.78 ± 0.12	22.58 ± 13.03	0.88 ± 0.03	26.62 ± 11.19

The best parameters for the affine transform were the Gaussian pyramid with three resolutions and the mutual information metric with a 64-bin histogram. For B-spline transforms, the best segmentation results were achieved with a grid spacing of 22 mm, 40 mm, and 10 mm in x, y, and z axes, respectively. The average segmentation performance achieved with each set of hyper-parameters are presented in A.2. The time required to obtain automatic segmentation for a patient was 20-25 minutes on a laptop workstation Dell Precision 7540 with Intel Core i7-9850H at 2.60GHz processor.

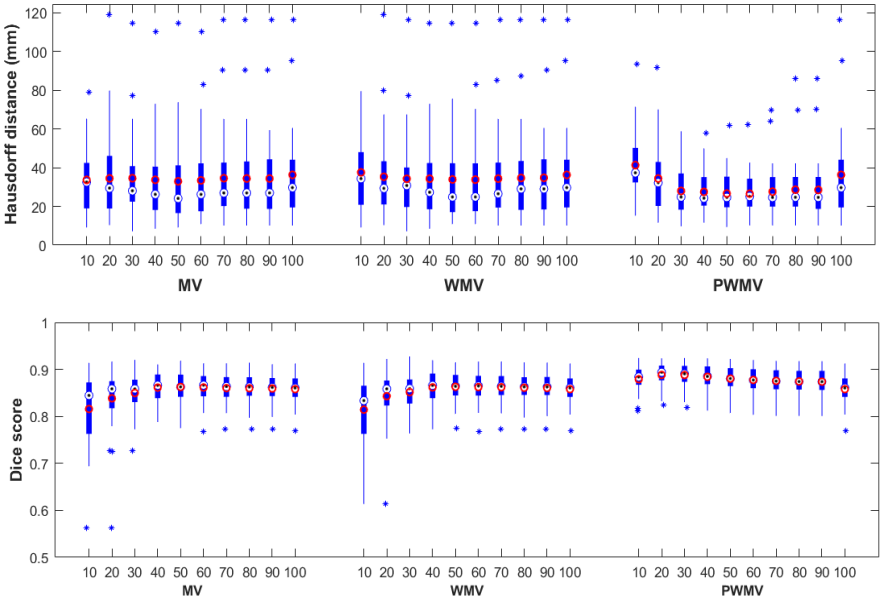

Figure 4.3: Comparison of label fusion strategies with atlas selection. The boxplots display the median, maximum and minimum performance values for global DSC and global HD achieved with MV, WMV and PWMV and as functions of the percentage of atlases preserved. The red circle on each boxplot represents the average segmentation performance.

Figure 4.3 shows the results of the evaluation of the different fusion methods with respect to the number of candidate segmentations used. It can be observed that both in DSC and HD, the PWMV fusion strategy reduces the number of outliers and minimizes to a large extent the HD. The best PWMV performance is achieved with the use of about 50% to 60% percent of the most similar atlases with respect to the range of SSIs obtained for each patient. The performance of the method with the best parameter set and PWMV is presented in Table 4.1. The performance at the AAo+Arch and TDAo is higher compared to the performance computed in the complete aorta. This behavior represents the impact of the error at the level of the abdominal aorta on the global segmentation performance. By visually inspecting the distance maps of all patients, it was found that in 75% of the patients, the highest error corresponding to the HD occurred in PAAo.

From the evaluation of the maximum diameter, a p-value of $p = 0.8$ was obtained for t-test, approving the null hypothesis that there is no statistically significant difference between the maximum diameters measured with manual segmentation and the maximum diameters measured with automatic segmentation obtained with 50% of the most similar candidates segmentations and PWMV algorithm. Figure 4.4 shows a correlation graph of the diameters obtained with manual segmentation and the diameters obtained with automatic segmentation, in which a low dispersion of the data can be observed, obtaining a r^2 (i.e: correlation coefficient) equal to 0.86. The Bland-Altman analysis showed a mean difference of the maximum diameter obtained with automatic and manual segmentations equal to -0.14 ± 1.7 mm. Considering that the resolution of the images is 2 mm cubed,

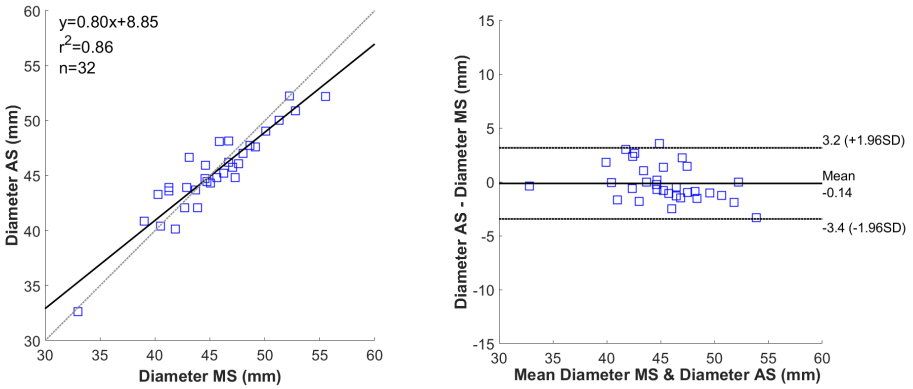

Figure 4.4: Scatter plot with regression line (a) and Bland-Altman plot (b) of maximum diameters obtained with manual (MS) and automatic segmentations (AS)

an average difference of -0.14 mm is considered low. In addition, 97% of the measurements fall within the limit of agreement.

4.4/ DEEP LEARNING-BASED SEGMENTATION

Over the past two decades, deep learning has been widely used for task automation using medical images. Promising results in different medical image segmentation tasks have made this method the first choice for automatic segmentation [84]. We selected a deep learning-based method because it has recently outperformed several previously proposed segmentation methods [69, 70]. In addition, in a future application, the time for segmenting a new patient could be considerably less than the one required by methods such as MAS. 3D segmentation of the aorta from 4D flow MRI using deep learning has been proposed in [90] and [104]. However, as in the MAS-based method proposed by Bustamante et. al. [72], the segmentation task was performed from a generated 3D PCMRA. In our work, deep learning-based systolic phase segmentation was performed using 4D flow MRI magnitude image. Due to the high blood flow in the aorta, the choice of the systolic phase provides better border definition and the crucial blood flow information at the inlet at this time point.

4.4.1/ 3D U-NET SETUP

Automatic segmentation of the aorta in the systolic phase from 4D flow MRI was generated with a U-Net model for 36 patients. In the convolution layers of the implemented four levels U-Net architecture [75], kernels of size 3x3x3 were used. After each convolutional layer, batch normalization was performed to stabilize the learning process and improve the performance. After each BN process, the rec-

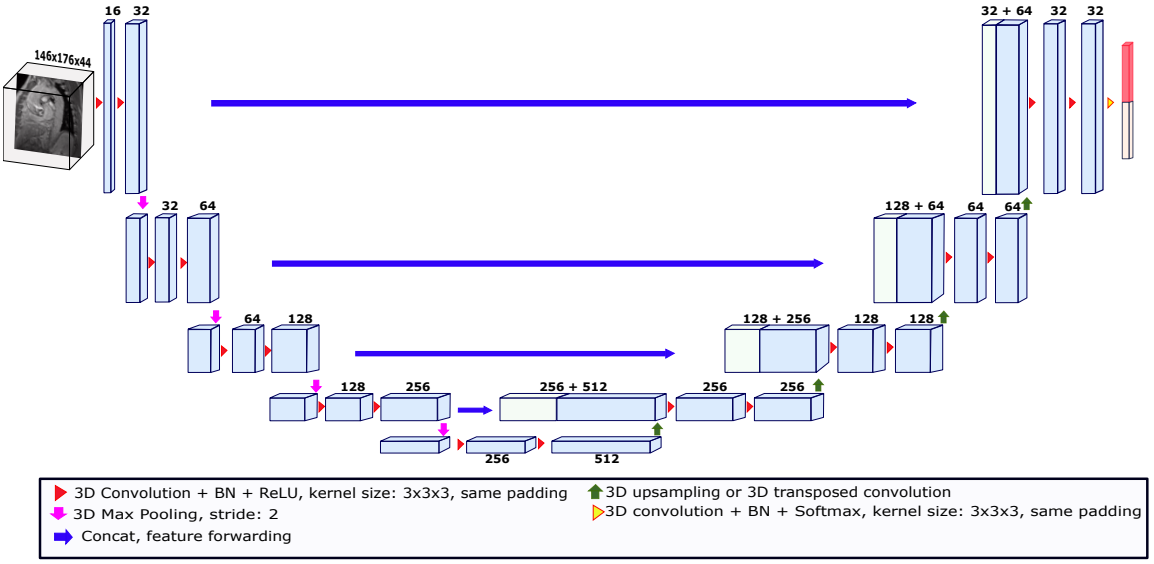

Figure 4.5: 3D U-Net architecture used. The numbers above the blocks indicate the number of feature maps.

tified linear unit (ReLu) activation function was applied. The expansion in the decoder path can be done with up-sampling operations or transposed convolutions, so we evaluated both techniques (Figure 4.5). To set the network input, the images were cropped or padded based on the median size of the x and y axes and the maximum size of the z axis across the entire database. Thus, the input size of the 3D U-Net in this work was 146x176x44 voxels.

To find the best hyper-parameters, the two 3D U-Net versions were trained with several combinations of batch size (two, four or six) and loss function (Dice loss computed on all the batch, average of the Dice loss computed for each image in the batch and a loss function that combines Dice and binary cross-entropy losses). Additionally, the models were trained for 850 epochs setting the initial learning rate equal to 0.01 and reducing it by a factor of ten when the validation loss stops improving.

4.4.2/ 3D U-NET RESULTS

The best performance was obtained using the average of the Dice loss computed for each image in the batch, a batch size equal to four and the model that applies up-sampling operation on the decoder path. Performance in the whole aorta was 0.92 ± 0.02 and 21.02 ± 24.20 for DSC and HD. Concerning the local performance an average HD of 9.41 ± 3.45 mm, 5.68 ± 6.23 mm and 16.18 ± 13.27 mm and an average DSC of 0.93 ± 0.02, 0.93 ± 0.02 and 0.84 ± 0.08 were reached respectively for AAo+Arch, TDAo and PAAo. The tests were run on a computational cluster with GPU NVIDIA Tesla V100. 3D U-Net training with the leave-one-patient-out strategy took approximately 2 hours per fold. After training the model, the inference of a new patient took about 2.5 seconds on a laptop workstation Dell Precision 7540

with Intel Core i7-9850H at 2.60GHz central processing unit (CPU).

4.5/ MULTI-ATLAS-BASED SEGMENTATION VS. 3D U-NET BASED SEGMENTATION

After the encouraging results obtained with the evaluation of MAS and 3D U-Net in aortic segmentation from 4D flow MRI, both methods were compared to establish a path towards 4D aortic segmentation. Both methods were implemented with their respective best parameters on 36 patients. The performance of the algorithms was first compared in terms of DSC and HD (Tables 4.2 and 4.3). We evaluated the statistical significance of the performance differences of the automatic segmentation methods. The evaluation was performed for both DSC and HD. The same procedure was performed for each metric. First, the Shapiro-Wilk test [2] was used to independently evaluate the normality of the measurements obtained with MAS and with U-Net. Then, when verifying that the measurements obtained with at least one of the methods were not normally distributed, the Wilcoxon signed rank test with a 95% confidence level [1] was applied to compare the differences between the metrics obtained with MAS and 3D U-Net. The Wilcoxon signed rank test performed globally showed a statistically significant difference between the automatic methods for both the DSC ($p\text{-}value < 0.0001$) and the HD ($p\text{-}value = 0.001$). Locally, except for the HD in PAAo, a statistically significant difference was also obtained for DSC and HD ($p\text{-}values < 0.001$). It can be said that for DSC and HD at TAo, deep learning outperforms MAS with a significant improvement in segmentation.

Table 4.2: MAS segmentation performance in the systolic phase from 4D flow MRI magnitude imaging

MAS local performance					
AAo+Arch		**TDAo**		**PAAo**	
DSC	**HD [mm]**	**DSC**	**HD [mm]**	**DSC**	**HD [mm]**
0.89±0.03	16.33±6.30	0.90±0.04	7.67±2.94	0.78±0.13	20.61±12.75
MAS global performance					
Thoracic Ao			**Whole Ao**		
DSC		**HD [mm]**	**DSC**		**HD [mm]**
0.89±0.02		16.27±6.26	0.88±0.03		26.04±16.63

For further evaluation of the methods, we compared the segmentation performance with those obtained from the inter-subject variability analysis. Moreover, the dependence of the algorithm's performance on the amount of data was assessed. In addition, aortic wall pressure was calculated using the manual and the automatic models. Pressure results were analyzed to identify the automatic method that provides values similar to those obtained from manual segmentation.

Table 4.3: U-Net segmentation performance in the systolic phase from 4D flow MRI magnitude imaging

U-Net local performance					
AAo+Arch		**TDAo**		**PAAo**	
DSC	**HD [mm]**	**DSC**	**HD [mm]**	**DSC**	**HD [mm]**
0.93±0.02	9.41±3.45	0.93±0.02	5.86±6.23	0.84±0.08	16.18±13.27
U-Net global performance					
Thoracic Ao		**Whole Ao**			
DSC	**HD [mm]**	**DSC**	**HD [mm]**		
0.93±0.02	11.49±8.98	0.92±0.02	21.02±24.20		

4.5.1/ INTER-OBSERVER VARIABILITY EVALUATION

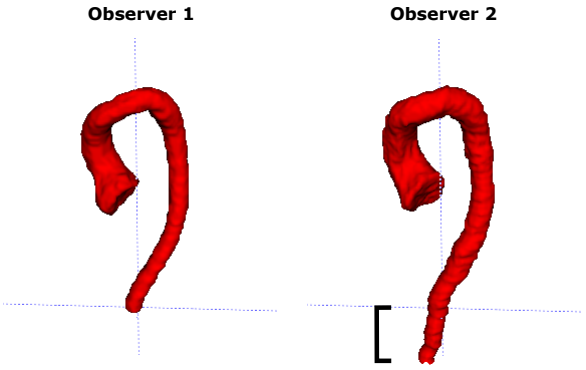

Figure 4.6: Segmentation for one patient generated by two image analysts. The bracket covers the difference between the two observers at the level of the abdominal aorta.

The inter-observer variability analysis was carried out to compare the performance of the automatic methods with those obtained by experts. Based on the inter-observer evaluation approach proposed by Klein et al. [25], the average DSC and average HD between the segmentations performed by the two image analysts were calculated. The average of the values obtained in the whole database was compared with the average performances of the automatic segmentation algorithms trained with the leave-one-out strategy (Table 4.4).

As for the algorithms, the inter-observer mean variability is higher in the PAAo than at AAo+Arch and TDAo. At the PAAo level, inter-patient performance is mainly related to the length of the aorta each observer takes (Figure 4.6). For the algorithms, it could be related to the degradation of the image quality in this region due to the thoracic coil's distant location and the decrease of the homogeneity of the magnetic field.

Table 4.4: Variabilidad inter-observador en la segmentación local de la aorta

Local inter-observer variability					
AAo+Arch		TDAo		PAAo	
DSC	HD [mm]	DSC	HD [mm]	DSC	HD [mm]
0.87±0.04	11.31±3.18	0.84±0.05	8.68±3.65	0.67±0.12	23.70±22.65
Global inter-observer variability					
Thoracic Ao			Whole Ao		
DSC	HD [mm]		DSC	HD [mm]	
0.86±0.04	11.76±3.56		0.83±0.05	25.24±21.81	

4.5.2/ DATA AMOUNT DEPENDENCY EVALUATION

The influence of the amount of training data on the method's performance was evaluated with a cross-validation strategy. For this purpose, the 36 patients were split into six folds. The segmentation algorithms were carried out by increasing the number of folds used for training and always keeping the same fold for validation. This experiment was replicated six times, changing the validation fold used to evaluate the influence of the examples taken as validation (Fig. 4.7).

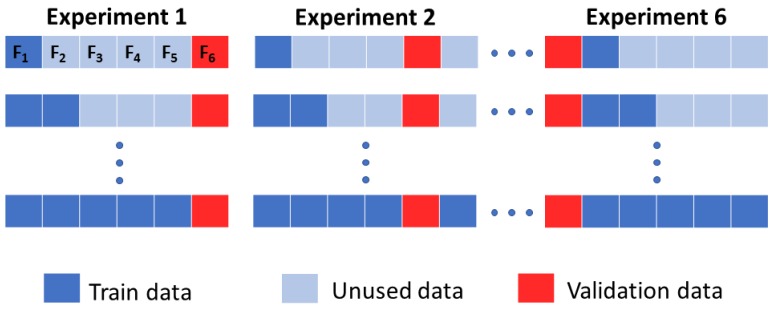

Figure 4.7: Data partitioning for cross-validation to assess the dependence of MAS and U-Net on the amount of training data and the data chosen for validation.

From the influence of training data amount analysis, an overall tendency was observed to continuously improve performance when training data was added for both methods. For HD, MAS constantly outperforms 3D U-Net. However, with respect to DSC, the MAS outperformed 3D U-Net only when between six and eighteen patients were used for training. After this number, a slight improvement of 3D U-Net with respect to MAS was observed. Figure 4.8 shows the average performance between the experiments as a function of the amount of data included for training.

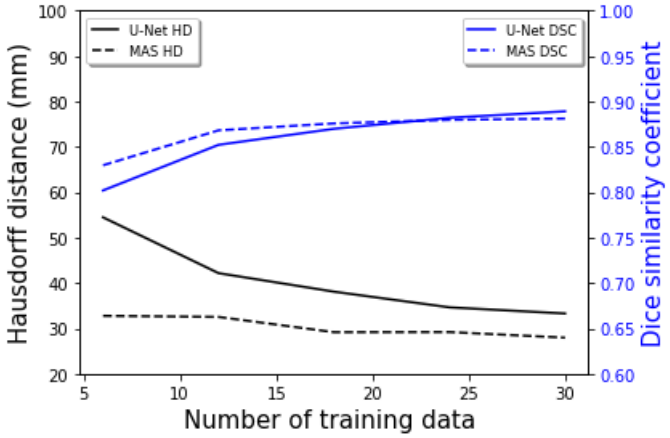

Figure 4.8: Performance of MAS and U-net with respect to the amount of training data. The graph represents the average performance of the experiments as a function of the number of training data used.

4.5.3/ Evaluation of 3D automatic segmentations in aortic wall pressure computation

After segmentation of the aorta, the valuable information provided by 4D flow MRI can be used for the generation of different markers. In addition to widely used biomarkers such as aortic diameter or peak velocities in a 2D plane, the aim of segmenting the aorta from 4D flow MRI is to compute hemodynamic biomarkers. In this sense, fluid dynamics biomarkers obtained with numerical simulation contribute to the analysis of the progression of TAA [45, 60]. Hemodynamic parameters can be computed using Computational Fluid Dynamics (CFD) [10]. However, the accuracy of the segmentation can influence the results. For this reason, CFD was used to assess the impact of differences in automatic segmentation on aortic wall pressure. Aortic wall pressure is a relevant index for understanding the evolution of the aneurysm since the high wall pressure corresponds to high intramural stress exerted on the wall [61, 71].

The manual and automatic segmentations of each patient were converted to meshes. Then, the meshes were discretized before CFD to be able to compare the pressure obtained from manual and automatic models. The discretization was performed by applying mesh morphing [91]. Mesh morphing was adopted to build iso-topological patient-specific meshes, having the same number of nodes and the same connectivity to introduce the missing parts of the segmentation as the three supra-aortic vessels. The discretization process with mesh morphing is performed independently for each patient. It starts by adapting a mesh generated for a single baseline model to the manual segmentation. Then, this new deformed mesh is adapted to the automatic models generated with MAS and U-Net. In particular, each manually segmented model was used in a two-step morphing procedure: a first step in approaching the segmented surface and a second projection step to completely fit the target geometry. Once a new patient-

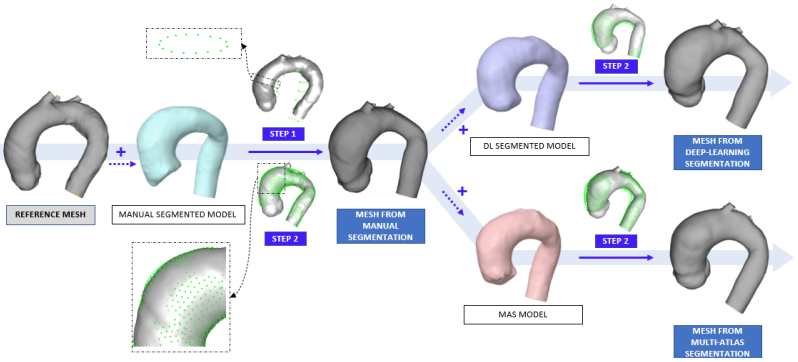

Figure 4.9: Mesh morphing workflow: the reference mesh is morphed in two steps to reach the manually segmented STL model: for step 1, the final SP positions arranged in circles perpendicular to the centerline and obtained on the STL to be fitted are shown in green. For step 2, the updated SPs are shown for the final projection onto the STL. Then, starting from this new deformed grid, only the projection step 2 is carried out to correctly represent the geometry resulting from deep-learning (upper branch) and multi-atlas segmentations (lower branch).

specific mesh was obtained with the projection on the manually segmented aorta, only the second step was required to correctly fit both MAS and 3D U-Net models which were already close to the deformed starting mesh (Figure 4.9).

The starting reference mesh, which includes the three supra-aortic vessels and adapted each time to the new segmented geometry, was generated in ANSA pre-processor (BETA CAE Systems, Switzerland). To obtain an accurate high quality starting discrete domain, the mesh was created using a segmentation derived from a CT-scan (OPTIMA CT660, Siemens Healthcare GmbH; 0.63 mm slice thickness, 0.5 mm in-slice pixel size) belonging to one of the patients in the dataset. The latter was chosen as a reference because it has the smallest deviation in terms of maximum diameter (53.2 mm) of the ascending tract from the median value of 52 mm of the whole MRI dataset. In fact, this is the criterion that generally allows to minimize the distortion of the elements during their stretching or compression to fit a new segmented model [32, 100] . The rigid alignment between the segmented models and the reference mesh was performed with the Iterative Closest Point (ICP) algorithm using 100 iterations in $Meshlab$, an open-source system for processing and editing 3D triangular meshes. Only the TAo was considered (i.e. AAo+Arch and TDAo) because the lower the number of elements in the mesh, the lower the computational cost of the simulation and because all patients in the database had aneurysms only at the AAo level. For analysis, the tracts of the three supra-aortic vessels were isolated from the rest of the aorta.

After the mesh morphing procedure, three CFD simulations were carried out for each patient with the same computational setup. As part of this work, steady state simulations were set up and the effect of the external body forces were considered to be zero. After the evaluation of the Reynolds number, a Reynolds-averaged Navier–Stokes (RANS) turbulent model was applied. The fluid was considered Newtonian with a dynamic viscosity of 0.0035 $Pa{\cdot}$s and a density of 1056 $\frac{kg}{m^3}$. Ves-

sel walls were assumed rigid with a no-slip boundary condition. Considering a plane perpendicular to the centerline of the aorta at the level of the sino-tubular junction, the CFD inlet was retrieved from the phase images of the 4D flow MRI. This task was automatically performed using an in-house tool based on ITK and VTK libraries. From the velocity values obtained on each pixel, the average was computed for the simulation inlet. Since in a lumped parameter model (LPM) compliance only affects transient flow, the total resistance was only included for the peak systolic flow. A capillary pressure P_0=2.4 kPa [9] was introduced to modulate the relationship defined by $Q = (P - P_0)/R$ between the flow rate Q, the outlet pressure P and the total resistance R for the downstream peripheral vessels. As the three upper outlets were not visible from the MRI images, the values of R for the TDAo, BA, LCCA and LSA outlets were arbitrary chosen ensuring for each patient a flow split ratio of 70%, 20%, 5% and, 5% respectively, as reported in [94]. Numerical simulations were performed using the commercial CFD solver ANSYS Fluent and the convergence criteria threshold for the residual errors was set to 1.0×10^{-4}.

4.5.3.1/ AORTIC WALL PRESSURE ANALYSIS

To evaluate and compare the aortic wall pressure, the results were analyzed globally and separately/locally into AAo+Arch and TDAo. The simulated pressures were analyzed with different methods to identify the automatic segmentation that provides robust biomarkers compared to those obtained with the manual segmentation. By exploiting the invariance in the number of nodes and grid connectivity, the intra-patient average Root Mean Square Error (RMSE) between the pressure values obtained with the manual contouring and each automatic method was evaluated. A Bland-Altman analysis was also performed on the average pressures obtained globally and locally, i.e. for each part of the aorta. Finally, to evaluate the predictive capacity of each automatic method with respect to the pressure values obtained from the manual segmentation, a linear regression analysis was performed with co-variance adjusted per cluster, i.e. per patient. For this, we reported the regression coefficient, r^2 and the confidence interval of each regression model obtained between the pressures derived from the manual and automatic segmentations.

4.5.3.2/ AORTIC WALL PRESSURE RESULTS

Concerning the morphing, the quality of the grid generated after the procedure was evaluated for each patient. One model derived from multi-atlas-based segmentation reported a Skewness above 0.99 after mesh morphing. This model was excluded from the analysis of the results since the simulation did not reach convergence. All the remaining models had a Skewness below 0.95 except for one which had a skewness of 0.97. No convergence problems were detected for them and therefore, the comparative analysis of the simulated wall pressures was

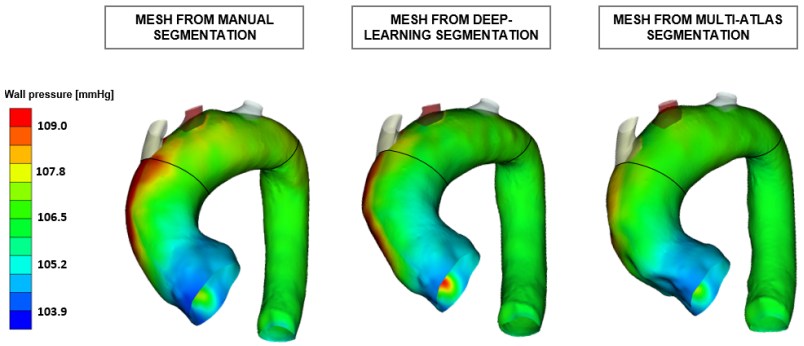

Figure 4.10: Wall pressure distribution for a patient with the manual and automatic methods

Table 4.5: Average RMSE of the aortic wall pressure computed for all the patients using the manual and automatic models

Method	AAo + Arch [mmHg]	TDAo [mmHg]	GLOBAL [mmHg]
MAS	2.13±2.19	1.12±1.6	1.90±2.0
U-net	1.61±0.68	0.72±0.5	1.41±0.6

carried out on 35 of 36 patients. An example of wall pressure distribution for a patient is shown in Figure 4.10.

Table 4.5 shows the average RMSE values on patients, obtained by comparing the pressures computed with the manual models and each of the automatic models. From the results it can be seen that MAS produces the highest RMS in the three regions evaluated.

From the Bland-Altman analysis a mean of 0.06 ± 0.63 mmHg was obtained when comparing the average pressures for the entire aorta of the manual model with the average pressures from U-Net. When the Bland-Altman analysis was performed for MAS, the mean pressure was -0.34 ± 2.32 (Fig. 4.11).

Locally, the mean differences for U-Net were 0.06 ± 0.71 mmHg in the AAo+Arch (Figure 4.12) and 0.04 ± 0.049 mmHg in the TDAo (Figure 4.13). For these same regions, the mean differences with MAS were -0.37 ± 2.58 and -0.27 ± 1.14, respectively. Overall, the average difference with U-Net was lower than that of MAS. Moreover, MAS presents two data far outside the limits of agreement in all cases.

The linear regression between the manual pressures and those obtained with U-Net gives a correlation coefficient of 0.97, with a 95% confidence interval of [0.93, 1.00]. Additionally, the r^2 for the regression was 0.94. In contrast, the coefficient obtained from the regression between the manual pressures and those obtained from MAS was 0.83 with 95% confidence interval of [0.65, 1.00] and a r^2 equal to 0.82.

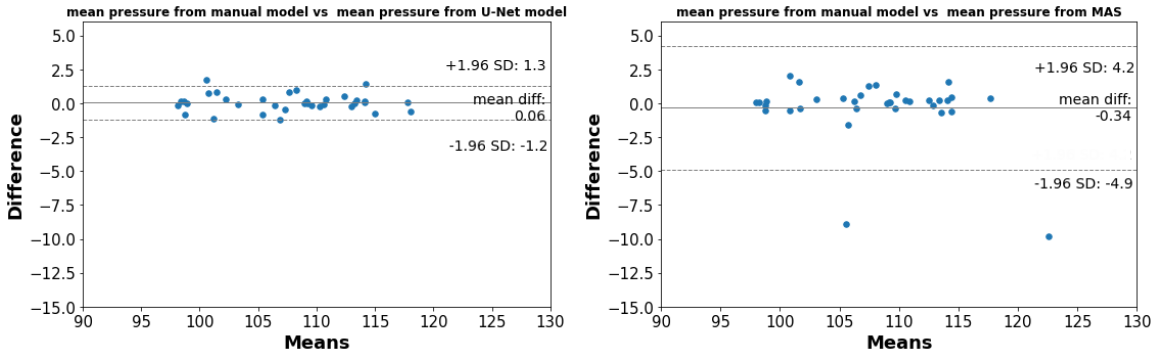

Figure 4.11: Bland-Altman plots of the average pressures obtained in the complete aorta by using the manual and the automatic models.

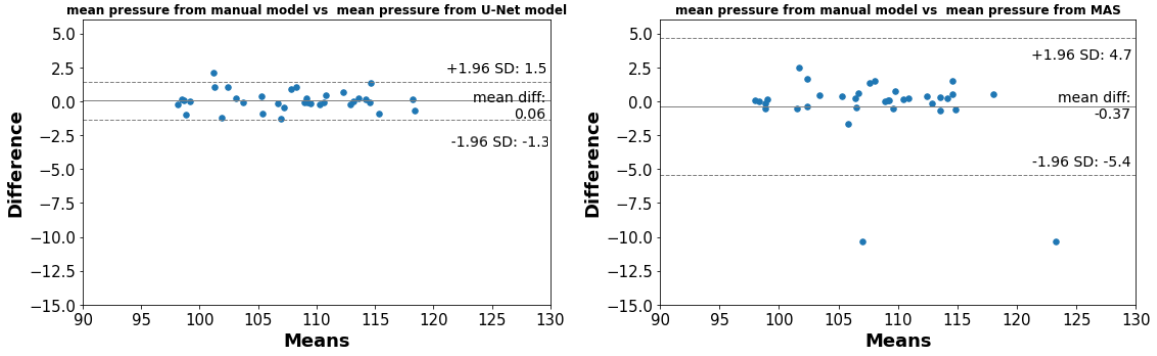

Figure 4.12: Bland-Altman plots of the average pressures obtained in the AAo+Arch by using the manual and the automatic models.

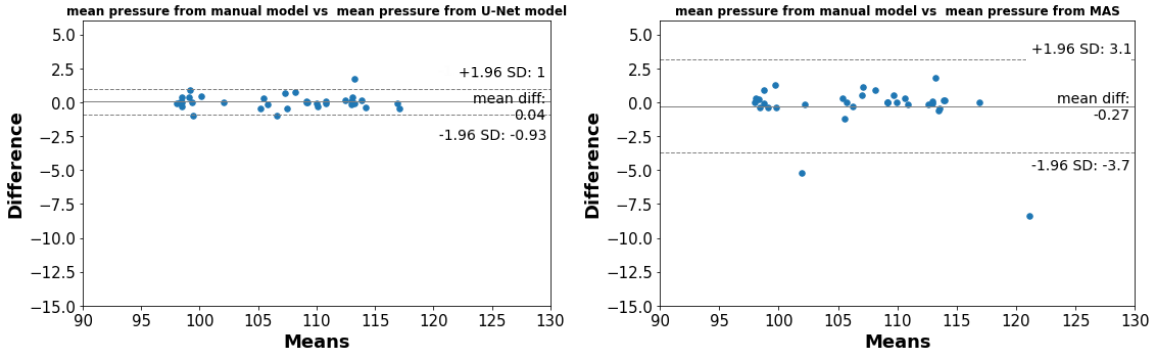

Figure 4.13: Bland-Altman plots of the average pressures obtained in the TDAo aorta by using the manual and the automatic models.

4.6/ DISCUSSION

In this chapter, we evaluated a MAS method and a deep learning-based method to segment the aorta in 3D from 4D flow MRI magnitude images. Initially, each method was implemented and evaluated independently on a set of patients to identify the best set of parameters. Later, both methods were compared in terms

of DSC, HD, and aortic wall pressure to consider both image and biomarker-based metrics.

We evaluated the MAS method's performance with DSC and HD 3D metrics and maximum diameter. Previous works evaluated the MAS performance by calculating the blood volume with a 2D plane located manually or automatically in the AAo [48, 72]. However, the blood volume calculation is highly sensitive to the orientation of the plane [96]. Moreover, the 2D-plane-based evaluation does not allow for establishing a 3D segmentation performance.

It was observed that in the tested MAS pipelines, label fusion methods with local weighting reached a better performance than globally weighted methods. This finding is consistent with previous studies, which showed that local weighting outperforms global weighting [28]. Using a too-small set of atlases or the entire set of atlases in the label fusion step decreased the segmentation performance. This behavior may be due to the fact that there were not enough candidate segmentations or that some of them were not relevant for decision making and misguided the process. The best segmentation performance was obtained using the PWMV label fusion strategy with 50% of the candidate segmentations. Analyzing the results locally, it could be observed that the part of the aorta with the lowest performance is the PAAo due to signal-to-noise ratio degradation in that region. In contrast, the error of the automatic segmentation at the level of the TDAo was the lowest (Table 4.1), because in this region the borders of the aorta are better defined than in the other regions, which can better guide the registration. Segmentation errors at the level of the AAo+Arch were generally related to the difficulty in recognizing the shape of the valve from 4D flow MRI. Moreover, errors in the lateral region of the AAo were identified. It may be explained by the fact that MAS tends not to accurately estimate the aorta in this region since the objective function optimized with MAS is based on intensities. Then, the algorithm is sometimes limited in recognizing the boundaries between the aorta and the superior vena cava.

The 3D U-Net-based segmentation also presented a lower performance at the PAAo level compared to the other two regions. In particular, this method was affected by a patient with a notable signal loss between the TDAo and the PAAo. For this patient, the algorithm generated a segmentation of the aorta divided in two connected components: a first connected component with the TAo and a second one with the PAAo. Consequently, the PAAo of this patient was deleted with the post-processing. To address this problem, the implementation of strategies that constrain the 3D U-Net to generate a single connected component should be considered. To address this problem, a constrained cost function based on the topological characteristics of the aorta was implemented. The results obtained from applying this approach to our data are presented as appendices in A.1.

Previous methods based on deep learning were implemented using PCMRA. In comparison, our DSC results are slightly better than those reported in [97], i.e. DSC$\approx$0.90. However, this study includes multi-institution data, which should be considered in future evaluation of our method. The results were also comparable

with those obtained with the method proposed by Berhane et al. [90] for aortic segmentation from 3D PCMRA using deep learning. In particular, they obtained a median DSC of 0.95. For HD, errors at the PAAo level degraded our 3D U-Net performance. However, HD measured at AAo+Arch and TDAo were generally good. Figure 4.14 shows the HD map computed for the outlier patient who presented the highest error concerning this metric. Berhane et al. [90], obtained regular segmentations performances with HD around 28.7 mm and poor segmentations with HD of 43 mm. In their work, this problem was related to the degradation of the aorta shape during 3D PCMRA generation. One of the limitations of the 3D U-Net-based method is the size of the database used for training. However, as is natural in this approach and as shown with the evaluation regarding data amount (Fig. 4.8), better results could be reached by increasing the size of the database.

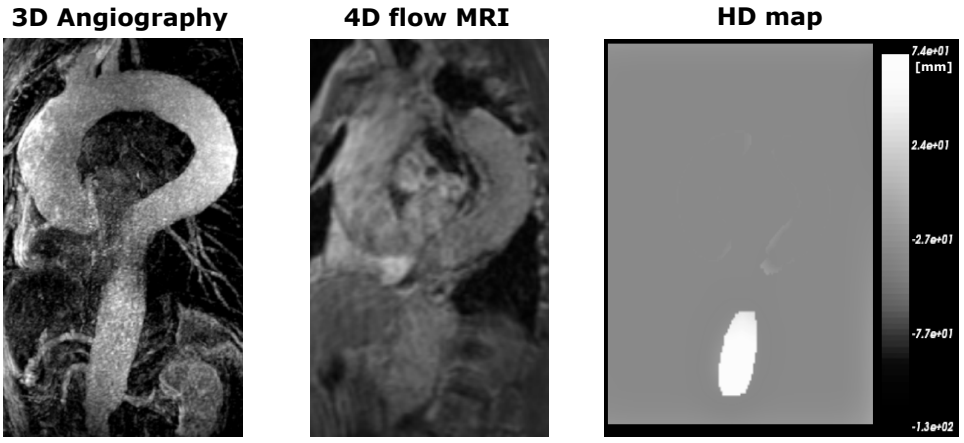

Figure 4.14: One slice of the HD map from the patient with the poorest performance for the 3D U-Net-based segmentation

From the comparison of MAS and 3D U-Net with 36 patients, the segmentation results showed that the best performance concerning DSC and HD was achieved by the 3D U-Net algorithm when trained on 35 patients. However, with less training data (Figure 4.8), the MAS algorithm usually gave better results. Although no overfitting was present in the U-Net models, the variance of the model is increased when less than 24 samples are used for training.

The inter-observer performance is also lower in the PAAo because each observer takes a different length of the aorta in this region. It is important to note that, except for the HD with the MAS algorithm, the two automatic segmentation methods outperform the inter-observer results. Juffermans et al. [99] also evaluated the inter-observer reproducibility of aortic segmentation. Each observer performed a semi-automatic segmentation refining the segmentation of an algorithm based on deformable models, using 4D flow MRI velocity images as input images. As a result of the proposed approach, the authors concluded that segmentations are reproducible without major limitations. However, semi-automatic segmentation is subject to bias since the observer's perception is influenced by the initial segmentation generated. On the other hand, using deformable-models-based algorithms on phase images can lead to inaccuracies in segmenting the aortic wall when

noise or low velocities are present. Still, the differences between segmentations generated by different experts from magnitude images should be further investigated.

Finally, the objective of comparing the aortic wall pressure results was to investigate the impact of the automatic methods on the computation of CFD-based biomarkers. The pressure differences from the U-Net segmentation compared to those from manual segmentation were smaller than those from manual segmentation compared to MAS segmentation. However, it should be noted that comparable performance with respect to DSC and HD in different regions, e.g. U-Net performance in AAo+Arch and TDAo, does not necessarily mean comparable performance on the computation of wall pressure. Indeed, an improvement in the segmentation performance allows to obtain pressures closer to those obtained with manual models. Nevertheless, whatever the segmentation method, the pressure differences are about twice as high at the AAo + Arch as the pressure differences at TDAo. This effect is due to turbulence and high velocities that mainly impact the AAo. Then, small segmentation error in the valvular area or in the sinus area can significantly alter the results [98].

To summarize, it can be concluded that the deep learning segmentation method should be preferred as it gives the best results. Then, deep learning approaches could be further explored to segment the aorta over the cardiac cycle.

5

4D SEGMENTATION OF THE AORTA FROM 4D FLOW MRI USING A 3D DEEP LEARNING MODEL

This chapter presents a pipeline for 4D segmentation of the aorta from 4D flow MRI magnitude images. The 4D segmentation of the aorta is essential since it allows the exploration of markers resulting from analyzing flow patterns over the cardiac cycle. A 4D segmentation of the aorta would then enable the examination of biomarkers obtained from 4D flow MRI to evaluate the progression of aortic aneurysms. Following the results obtained in the 3D segmentation of the aorta, a 4D segmentation approach based on 3D U-Net is implemented. The performance is analyzed with DSC and HD. In addition, the maximum and minimum surfaces obtained in a 2D+time plane at the level of the AAo are compared with those obtained from 2D+time cine-MRI. These metrics are important because they reflect the aorta elasticity and the capacity of the segmentation method to adapt to the aorta changes during the cardiac cycle.

5.1/ 4D SEGMENTATION BASED ON 3D U-NET

For the segmentation of medical images with more than two dimensions, approaches based on deep learning have been proposed to overcome computational limitations and to increase training samples. For example, 3D image segmentation has been addressed by segmenting each slice independently [74] or by segmenting three images perpendicular to each axis [44]. Extending this idea to 4D images, Bustamante et al. [102] recently proposed a 4D segmentation of the heart and great vessel from 4D flow magnitude images. In particular, they used a 3D U-Net model to independently segment these organs from each frame.

Standardizing a 4D segmentation method of the aorta from 4D flow MRI is still a problem that needs to be addressed to extend the use of this imaging modality in the analysis of flow patterns over the cardiac cycle. Here, we segmented the aorta in all phases of the cardiac cycle using the 3D U-Net model proposed in

section 4.4. The training of the model for this task was similar to that proposed by Mariana et al. [102]. However, they used a different patient population with ischemic heart diseases or mitral valve regurgitation but no aneurysm at the level of the TAo. On the other hand, for training and validation of the algorithm they used a fully automatic segmentations generated in two frames and propagated to the others thanks to an intra-patient registration algorithm. Due to the direct relationship between the registration quality and the segmentations quality, this method of generating ground truth includes errors in the position of the aorta at every time step. Unlike them, we use manual 4D segmentations reviewed by a clinical expert to implement and evaluate the algorithm.

5.1.1/ 3D U-NET BASED 4D SEGMENTATION SETUP

The model was trained with 500 epochs with the same best hyper-parameters as for the 3D aortic segmentation task: batch size equal to four and Dice loss function with an initial learning rate equal to 0.01. The training strategy was leave-one-out, and the manually delineated frames for each patient were treated as an independent sample. The model was trained using the five manually delineated frames for 35 patients (i.e., 175 frames) and validated with the five frames from the patient left out. To feed the network, the images were padded or cropped as in section 4.4.1 to obtain a size of 146x176x44. Later, the spacing of the images was modified to 4x4x4 mm^3 to speed up the training process and for comparison with a 4D neural network model. So the model was fed with images of size 73x88x22 voxels. To obtain the segmentation for all the time steps, the trained model is used to predict the remaining 20 frames.

All the automatic segmentations were post-processed with a morphological opening filter to smooth out irregularities. A ball structuring element of radius 1 mm used. In addition, the largest connected component was identified and selected as the final aorta segmentation. To take into account the soft temporal displacement of the aorta from diastole to systole we lastly apply a morphological opening filter on the 2D+time segmentation extracted from the 4D segmentation. A ball structuring element of radius 2 mm was used.

5.1.2/ 3D U-NET BASED 4D SEGMENTATION EVALUATION

As with the 3D segmentation methods, performance was evaluated locally and globally with the DSC and HD. Furthermore, the maximum and minimum surfaces were compared at the level of the pulmonary trunk with the ones obtained from axial 2D+time cine-MRI. These parameters are important because they represent the dynamic expansion of the aorta exerted to soften the pressure on the wall caused by the dynamic blood flow. In the presence of aortic pathologies, the elasticity of the aorta could be affected. The minimum and maximum surfaces over the cardiac cycle were computed in a 2D+time image extracted from the 4D

segmentation of the aorta, taking as reference the pulmonary trunk. For comparison, the minimum and maximum reference surfaces were computed from the 2D+time cine-MRI with an automatic algorithm based on the method described by Miteran et al. [76]. Pearson correlation of the minimum and maximum surface area values obtained with the two approaches, and after testing the normality of the samples with the Shapiro-Wilk test, a paired sample t-test was performed to assess the statistical significance of the results. A mean equal to zero is assumed as the null hypothesis. T-test was performed at both 95% and 99% confidence levels. Finally, the maximum and minimum surface areas were compared using Bland-Altman analysis.

The DSC was also calculated in 4D and frame by frame. However, the average in the database was equal, and the standard deviation difference was less than 0.03. Then, the results for DSC and HD are presented as the average of the measured values frame by frame.

5.1.3/ 3D U-NET BASED 4D SEGMENTATION RESULTS

The average global segmentation performance over the 180 frames was 0.9±0.02 and 17.76±16.78 mm for DSC and HD, respectively. Considering only TAo, DSC and HD were 0.92±0.02 and 10.07±5.99 mm, respectively (Table 5.1). The Figure 5.1 shows the patients with the best and worst segmentation results.

Table 5.1: 3D U-Net segmentation performance over the cardiac cycle

U-Net local performance					
AAo+Arch		**TDAo**		**PAAo**	
DSC	**HD [mm]**	**DSC**	**HD [mm]**	**DSC**	**HD [mm]**
0.9±0.02	8.75±3.00	0.9±0.02	7.19±6.03	0.80±0.07	15.38±15.44
U-Net global performance					
Thoracic Ao			**Whole Ao**		
DSC		**HD [mm]**	**DSC**		**HD [mm]**
0.90±0.02		10.07±5.99	0.90±0.02		17.76±16.78

The results concerning the maximum and minimum surface area obtained from 4D flow MRI and cine-MRI showed a high correlation with a correlation coefficient r of 0.85, and 0.86 respectively. The regression plots are presented in Figures 5.2 and Figure 5.3. The Bland-Altman analysis between the maximum surface measured with cine-MRI and 4D flow MRI showed an average difference of -82.12+174.63 mm^2. For the minimum surface, the average difference was 43.56+171.25 mm^2 (Figure 5.4).

The paired t-test with 95% confidence level showed a difference between the maximum and minimum surface area values obtained with 4D flow and cine-MRI. A p-value of 0.0097 [CI: -142.95 -21.22] was obtained for the maximum surface areas. When comparing minimum surface areas, a p-value of 0.15 [CI: -16.25 103.16]

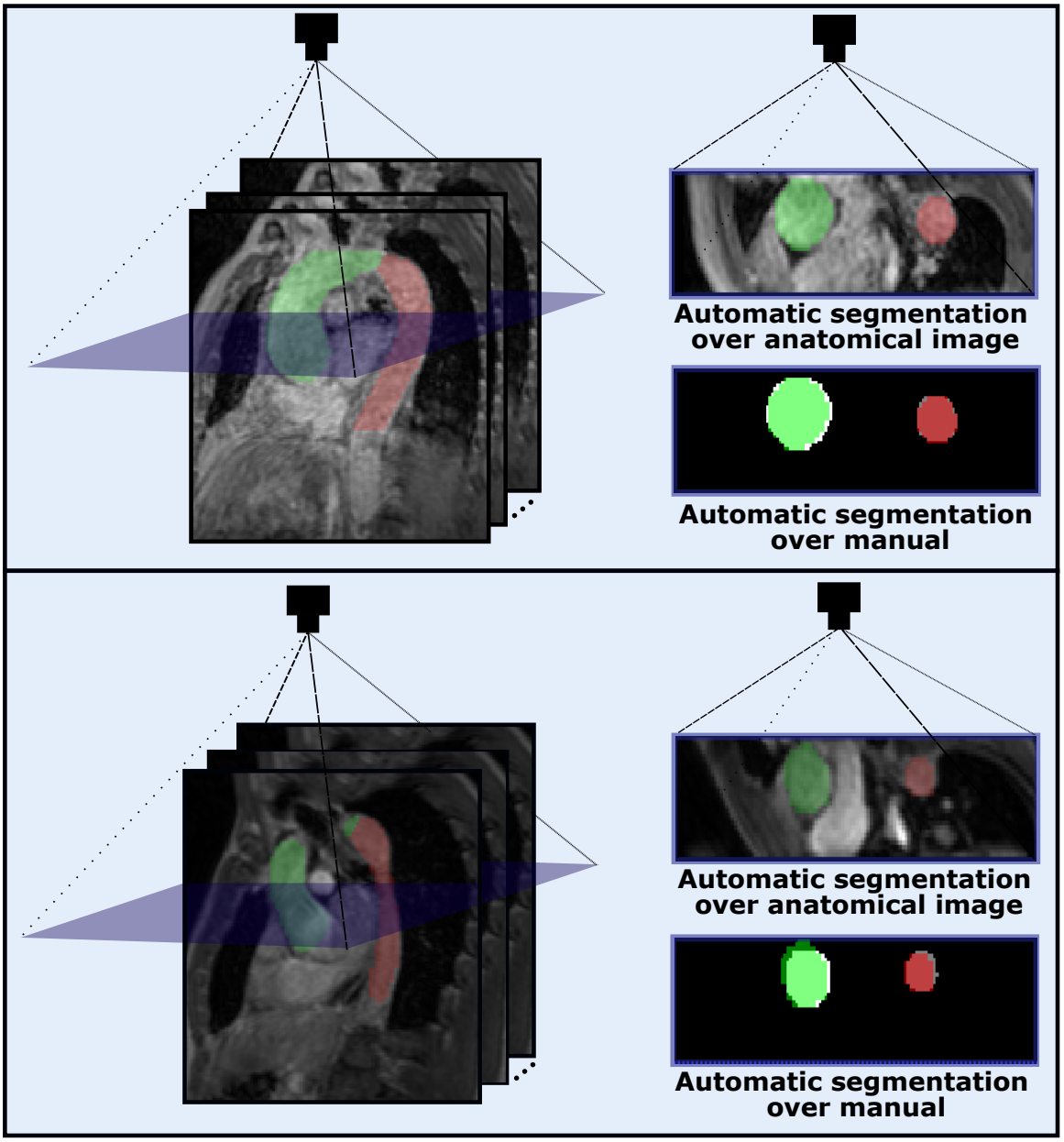

Figure 5.1: Slice the from patients with the highest (top image) and lowest (bottom image) performance. On the right is the automatic segmentation superimposed on the image at the level of the plane shown in blue. In addition, the automatic segmentation is superimposed on the manual segmentation in the same plane.

was obtained. Taking into account the difference in the acquisition protocol of 4D flow MRI and cine-MRI, a less stringent confidence interval (CI) was established by doing the t-test with a confidence level of 99%. Thus, p-value=0.0097 [CI: -163.82 -0.37] and p-value=0.15 [CI: -36.70 123.62] were obtained for the maximum and minimum surface area, respectively. Considering the significance level of 0.01, the t-test shows that for the minimum area, the average score does not differ significantly across the samples. The p-value is very close to the threshold for the maximum area, but zero is not included in the CI.

The training of the U-Net model took about one hour for each patient. The prediction of the 25 frames for each patient took only about 10 seconds on a laptop workstation Dell Precision 7540 with Intel Core i7-9850H at 2.60GHz CPU. In comparison, manual segmentation from scratch of a single frame takes about three hours.

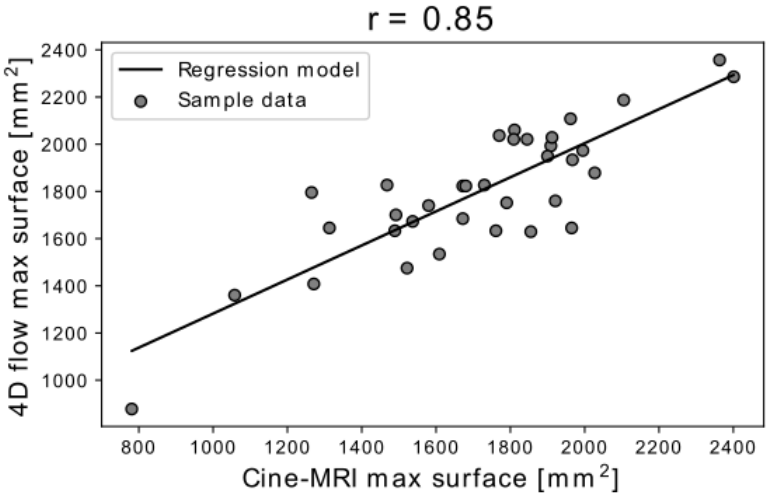

Figure 5.2: Correlation of the maximum surface calculated from cine-MRI and from 4D flow MRI.

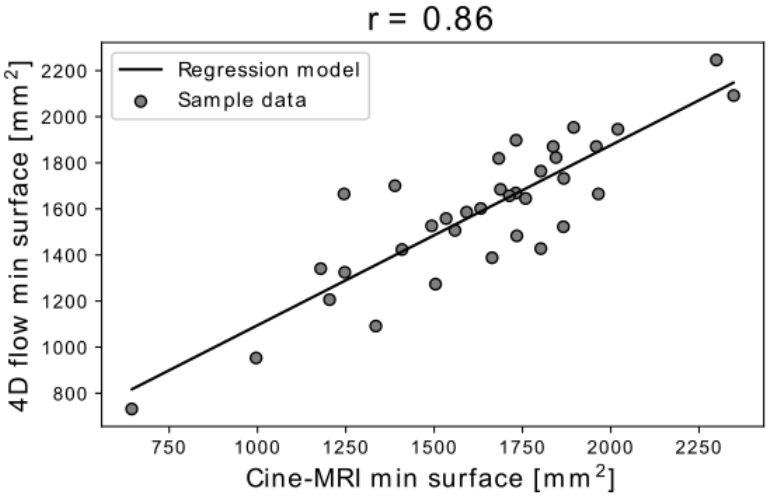

Figure 5.3: Correlation of the minimum surface calculated from cine-MRI and from 4D flow MRI.

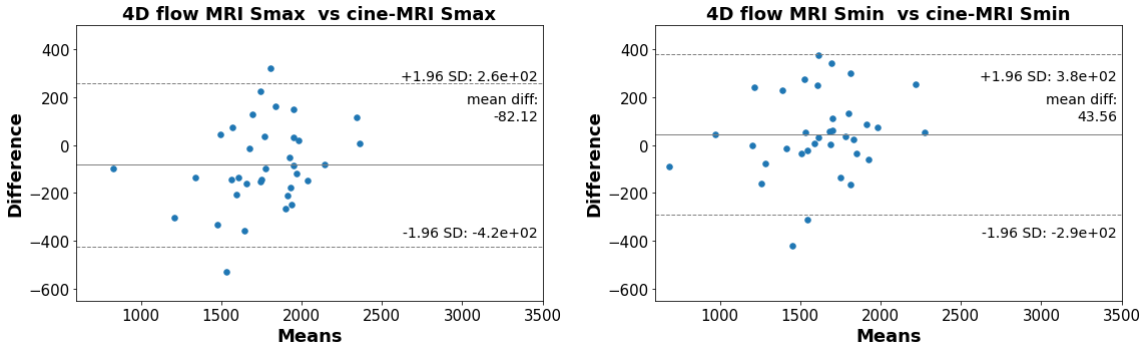

Figure 5.4: Bland-Altman plots of the maximum and minimum surface areas obtained at the level of the ascending aorta during the cardiac cycle.

5.1.4/ Discussion

In this chapter, we segmented the aorta over the cardiac cycle in patients with aneurysms by using a method comparable to the one proposed by Bustamante et al. [102]. Dilated aorta segmentation is more challenging than segmentation on healthy patients due to image degradation. The reduction in quality is generally caused by cardiac arrhythmia and extra-systole that affect the acquisition being ECG-gated with a retrospective gating. Thus, the aim of evaluating this approach was to contribute to the standardization of automatic 4D aortic segmentation techniques from 4D flow MRI by presenting the segmentation results of a 3D-based method in a dataset of patients with TAA.

For each time point of the cardiac cycle, the aorta was segmented using a 3D U-Net model on a magnitude image from 4D flow MRI. By doing so, we avoid the biases inherent in pre-processing to generate new images from 4D flow MRI, such as 4D flow-based PCMRA. On our dataset, the method evaluated gives promising results. The average DSC value computed on 180 volumes was 0.9 ± 0.02, comparable to those obtained by Bustamante et al. [102] (average DSC=0.93 ± 0.03) with a larger database without this type of pathology. However, as when segmenting the systole magnitude image frame from 4D flow MRI (section 4.4.2), the same degradation of performance was observed at the PAAo level. It is important to note that the way we have constructed our ground truth differs from Bustamante et al. [102]. In their case, an inter-patient multi-atlas based segmentation method was used to segment the end of systole and diastole before applying an intra-patient registration algorithm to segment the other time frames. The quality of the ground truth generated with this method is related to the parameters chosen by the user for the registration, which are generally not adequate for all patients. Segmentation may even fail for some patients, as it was the case for about 4% of the patients in the database of Bustamante et al. In our case, for all patients, we segmented manually five time frames and these segmentations were all reviewed by an expert. In this way, the model's performance is directly compared to that of an expert, thus avoiding the propagation of errors from automatic ground truth generation to the 3D U-Net.

Concerning 3D PCMRA aortic segmentation methods, Berhane et al. [90] achieved a slightly better performance than ours, obtaining a median of 0.95 for DSC. Although segmentation from PCMRA is facilitated by contrast enhancement between the aorta and the background, the position of the aorta during the cardiac cycle is questionable. In addition, generating this image can result in PCMRAs with degradation of aorta shape, mainly at the level of the aortic valve. With our approach, the lowest performance was in a frame corresponding to diastole. The low performance was directly related to signal loss during acquisition in the distal TDAo. However, in this frame, the degradation did not affect the AAo+Arch or the proximal TDAo, and a low HD were obtained in these regions (Figure 5.5). Therefore, this result does not affect the subsequent analysis of the maximum and minimum surface areas at the AAo level.

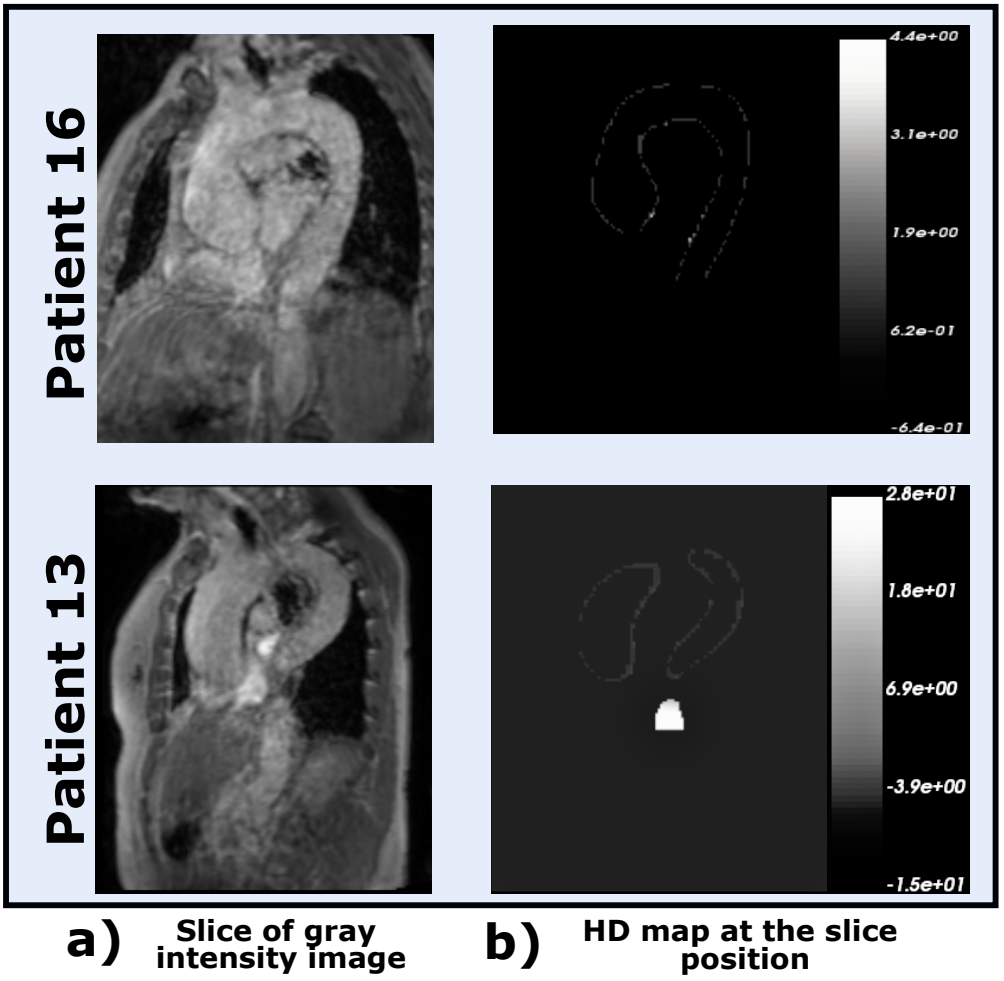

Figure 5.5: Patients with the lowest and highest Hausdorff distance a) Slice of the gray intensity image. b) HD map computed between the manual and automatic segmentation for the slice of the gray image.

In general, discrepancies between manual and automatic segmentations occurred at the level of the aortic valve or at the level of the the aortic arch (Figure 5.6). In these regions, the differences were generally in the order of five voxels (for 87% of the samples). This difference is relatively low considering particularly

the challenges in drawing the valve both manually and automatically. Specifically, the discrepancies at the level of the aortic valve might be due to the manual segmentation which is flat at this location. At the level of the aortic arch, the automatic segmentation sometimes includes voxels belonging to the brachiocephalic arteries. These voxels are considered as segmentation errors since they are not present in the manual segmentation.

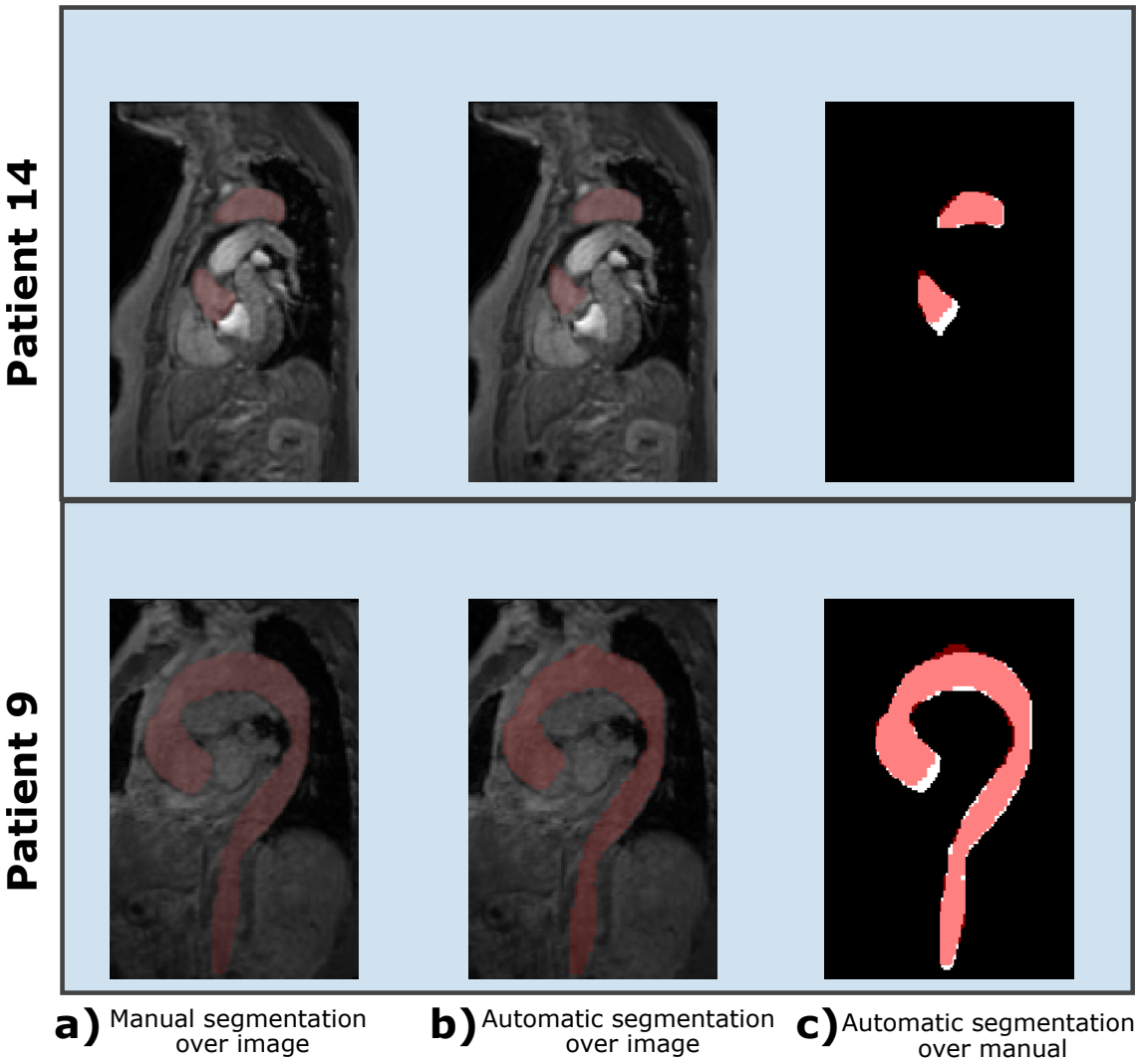

Figure 5.6: Two patients with the common types of errors at the level of the thoracic aorta. The errors occur at the level of the valve for the ascending aorta and at the level of the brachycephalic vessels for the aortic arch. a) shows for each patient the manual segmentation superimposed on a slice of the image. b) shows the automatic segmentation superimposed on the same image slice. c) shows the automatic segmentation superimposed on the manual one.

Implementing a 3D U-net model to segment the entire cardiac cycle can be considered a type of data augmentation since the training went from 35 samples (one per patient) when only the systole was segmented to 175 samples (five per patient) in this approach. The performance of the two approaches is not entirely

comparable, but it can be noted that with the 35 samples from systole, 3D-UNet achieved achieved slightly better results than when trained on 175 samples. This may be related to the inclusion of more frames belonging to the diastole, in which the definition of the aortic borders is lower, due to the low blood flow and then the lack of signal.

For further analysis of the behavior of the segmentation method in the temporal dimension, its ability to adapt to the different shapes of the aorta during the cardiac cycle was evaluated. For this purpose, the maximum and minimum surfaces calculated in 2D+time images extracted from the 4D segmentation was compared with the ones from 2D+time cine-MRI. Both 2D+time images were located taking as reference the pulmonary trunk and the maximum and minimum surfaces were calculated at the AAo. For both surfaces, a strong correlation (correlation coefficients > 0.85) between the two methods was obtained. It should be noted that the highest difference between the two methods is obtained when computing the maximum surface area. The t-test with a confidence level of 99% showed no difference between the minimum surface area calculated from 4d flow MRI and cine-MRI. However, the t-test performed for the maximum surface showed the confidence interval to be close to zero but did not include it. This may be related to the different physiological conditions during acquisition and the kind of imaging protocol for cine-MRI and 4D flow MRI. In particular, a force is exerted on the thorax by holding the breath during the cine-MRI acquisition. On the contrary, 4D flow MRI is a free-breathing acquired sequence. Moreover, the temporal resolution of cine-MRI sequence is better than 4D flow MRI.

Standardization of automatic 4D segmentation of the aorta from 4D flow MRI is vital to extend the use of this imaging modality. In this sense, with the evaluation of a similar method to the one proposed by Bustamante et al. [102], we obtained comparable results for subjects with TAA. Evaluation of the results shows that the 3D model adapts to the various shapes of the aorta during the cardiac cycle. This technique of 4D aortic segmentation from 4D flow MRI could contribute to the expanded use of this imaging in the analysis of pathologies such as TAA. In addition, the results encourage the exploration of hemodynamic biomarkers. The 4D segmentation allows the generation of biomarkers typically computed using static segmentation, such as wall shear stress, including bias in the result. Previous findings show that for 3D image segmentation, a 3D deep learning model represents spatial features better than 2D and 2.5 models [52]. So, it also raises the question of whether 4D segmentation benefits from a 4D model that allows to analyze spatial and temporal information at the same time.

6

4D SEGMENTATION OF THE AORTA FROM 4D FLOW MRI USING A 4D DEEP LEARNING MODEL

This chapter covers the 4D segmentation of the aorta using a 4D deep learning model. The results of the previous chapter showed promising performance for 4D segmentation of the aorta based on a 3D model. However, analyzing the effect of treating the temporal information provided by 4D flow MRI in the segmentation process could be interesting. For comparison purposes with the 3D U-Net-based 4D segmentation technique, the segmentation performance was measured with DSC, HD, and maximum and minimum surfaces at the level of the AAo.

6.1/ 4D DEEP LEARNING

As discussed in the previous chapters, 4D segmentation of the aorta has been generally addressed using 3D segmentation methods. Although we obtained promising results with the approach evaluated in the chapter 5, exploring segmentation techniques that consider the temporal information in 4D flow MRI is necessary. In the 3D medical image segmentation problem, it has been observed that 3D deep learning models interpret the spatial characteristics of the 3D image better than 2D and 2.5D models [52]. Based on this, it is necessary to evaluate whether a 4D model benefits the 4D segmentation performance and allows a better segmentation of challenging image regions.

Segmentations based on 4D deep learning models have rarely been explored. This is due, in part, to the fact that the deep learning frameworks (e.g. Pytorch or Tensorflow) have not developed layers for straightforward implementations of 4D models. Furthermore, the generation of 4D ground truth by an expert is a limitation since it is a highly time-consuming task.

In this chapter, we evaluated the performance of a 4D CNN model in aortic segmentation of patients with TAA using 4D flow MRI magnitude imaging. For this

purpose, we implemented a modified version of the 4D CNN architecture proposed by Myronenko et al. [87]. They implemented a residual 4D CNN that follows a conventional encoder-decoder structure for semantic segmentation. The model is composed of blocks in which convolution operations are performed with 3x3x3x3 kernels along with group normalization followed by the ReLU activation function. A skip-connection follows each block. In the encoder path, convolutions with stride two are used to reduce the spatial resolution of the output and move to the following representation level in the model. In this step, the dimension of the feature maps is doubled. One block is used for level zero, two blocks for level one, and four blocks for level two (Figure 6.1). In the segmentation task addressed by Myronenko et al. [87] the input 4D images were composed of 16 frames with a spatial resolution of 96x96x64 voxels. Thus, the smallest spatial resolution achieved with the initially proposed model was 24x24x16. In the decoder path, only one block is used for each level, and the up-sampling operation is performed with 4D nearest-neighbor interpolation after a 1x1x1x1 convolution. In addition, skip connections are used between the levels.

The objective of the architecture modification was to reduce the computation time without affecting the predictive capacity of the model. Thus, to reduce the number of parameters of the initially proposed model, we eliminated level two of the encoder path. Considering that the spatial resolution of our input images is 73x88x22 voxels, the smallest spatial resolution achieved is 37x44x11 voxels (Figure 6.2). The 323,274 trainable parameters with the original model were reduced to 115,162 with the proposed modification. Regarding computational time, the training time for each patient was reduced by 8.86%. Thus, for the leave-one-out strategy, the training on the entire database took about six days less.

In our 4D segmentation strategy based on a 3D model presented in chapter 5, it is only possible to use for training the frames for which a manual segmentation has been generated, and manually labeling all frames over the cardiac cycle is unfeasible. Myronenko et al. [87] defined a sparse loss function for the training of the original model. The purpose of this function is to allow the inclusion of unlabeled frames during training to take advantage of the inclusion of all temporal information. The cost function includes a temporal regularization that allows the model to learn temporal correlations while limiting abrupt changes over time. In our implementation, a normalized version of the original cost function was implemented to maintain the range ratio between the chosen metric and the time regularization term. In the following section, we present the details of the implemented residual 4D CNN network architecture.

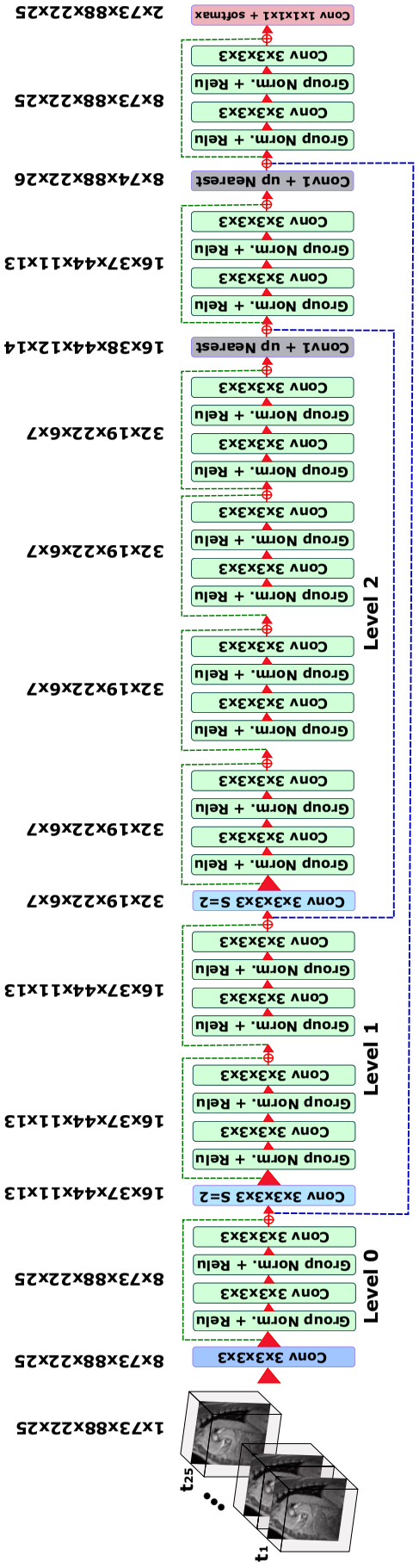

Figure 6.1: Original 4D residual convolutional neural network architecture

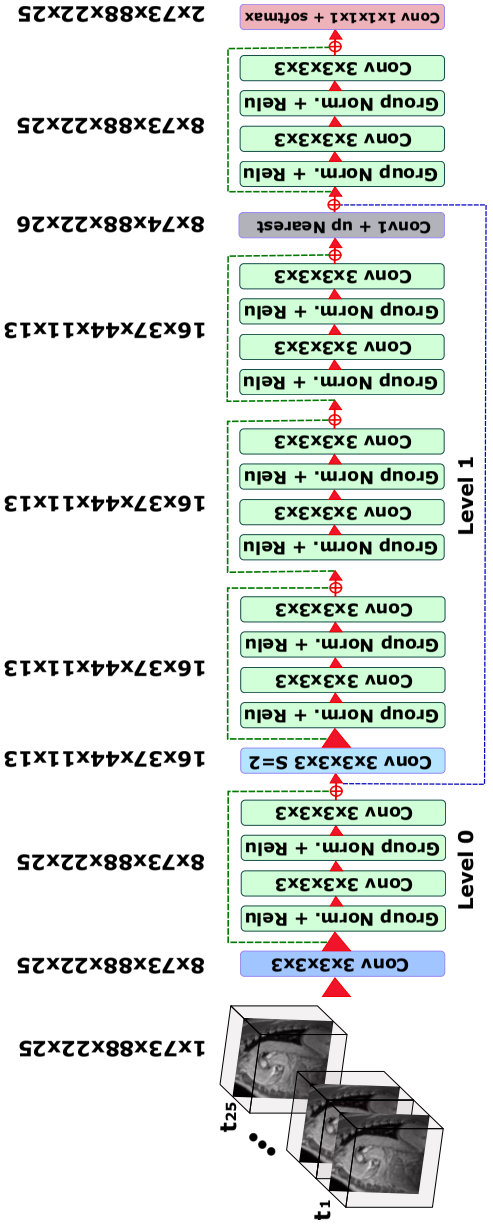

Figure 6.2: Proposed 4D residual convolutional neural network architecture

6.1.1/ 4D NETWORK FUNDAMENTALS

In the implementation of the 4D residual CNN network model, oversampling, convolution and normalization operations are performed in the different layers of the architecture. Model implementation was performed in Pytorch, and this section describes how existing tools in this framework were adapted to construct the 4D deep learning model.

6.1.1.1/ CONVOLUTIONS 4D

In a 4D convolutional layer l, let $X^{l-1} \in \mathbb{R}^{n_t \text{ x } n_h \text{ x } n_w \text{ x } n_d}$ be the input feature maps of four dimensions, n_t represents the size of the temporal dimension and n_h, n_w, n_d the spatial resolution. Let $K^l \in \mathbb{R}^{k_t \text{ x } k_h \text{ x } k_w \text{ x } k_d}$ be the kernel used in the convolution process. The 4D convolution is performed from the native Pytorch 3D convolution operation nested in two loops, as shown in the algorithm 1.

ALGORITHM 1: 4D convolution with native 3D convolution

Input : $X^{l-1} \in \mathbb{R}^{n_t \text{ x } n_h \text{ x } n_w \text{ x } n_d}$ – Input feature maps

$K^l \in \mathbb{R}^{k_t \text{ x } k_h \text{ x } k_w \text{ x } k_d}$ – Kernel

p_t – padding applied to each side of the temporal dimension

r_t – Stride for the temporal dimension ($r_t \in \mathbb{N}^*$)

Output: $X^l \in \mathbb{R}^{d_t \text{ x } d_h \text{ x } d_w \text{ x } d_d}$ – Output feature maps

$X^l[d_t,\ d_h,\ d_w,\ d_d,\ d_c] = 0$
$limit_{sup} = \text{floor}((n_t + p_t\text{x}2 - k_t)/r_t + 1)$
for i $\leftarrow 0 : k_t$ **do**
  for j $\leftarrow 0 : n_t + p_t\text{x}2$ **do**
    $out\_index_t = j - (i - \text{floor}(k_t/2)) - \text{floor}(n_t + p_t\text{x}2 - d_t)/2 - (1 - k_t\%2))$
    if $out\_index_t < 0$ **or** $out\_index_t >= limit_{sup}$ **then**
      continue
    end
    $X^l[out\_index_t :] += Conv3D(X^{l-1}[j :], K[i :])$
  end
end

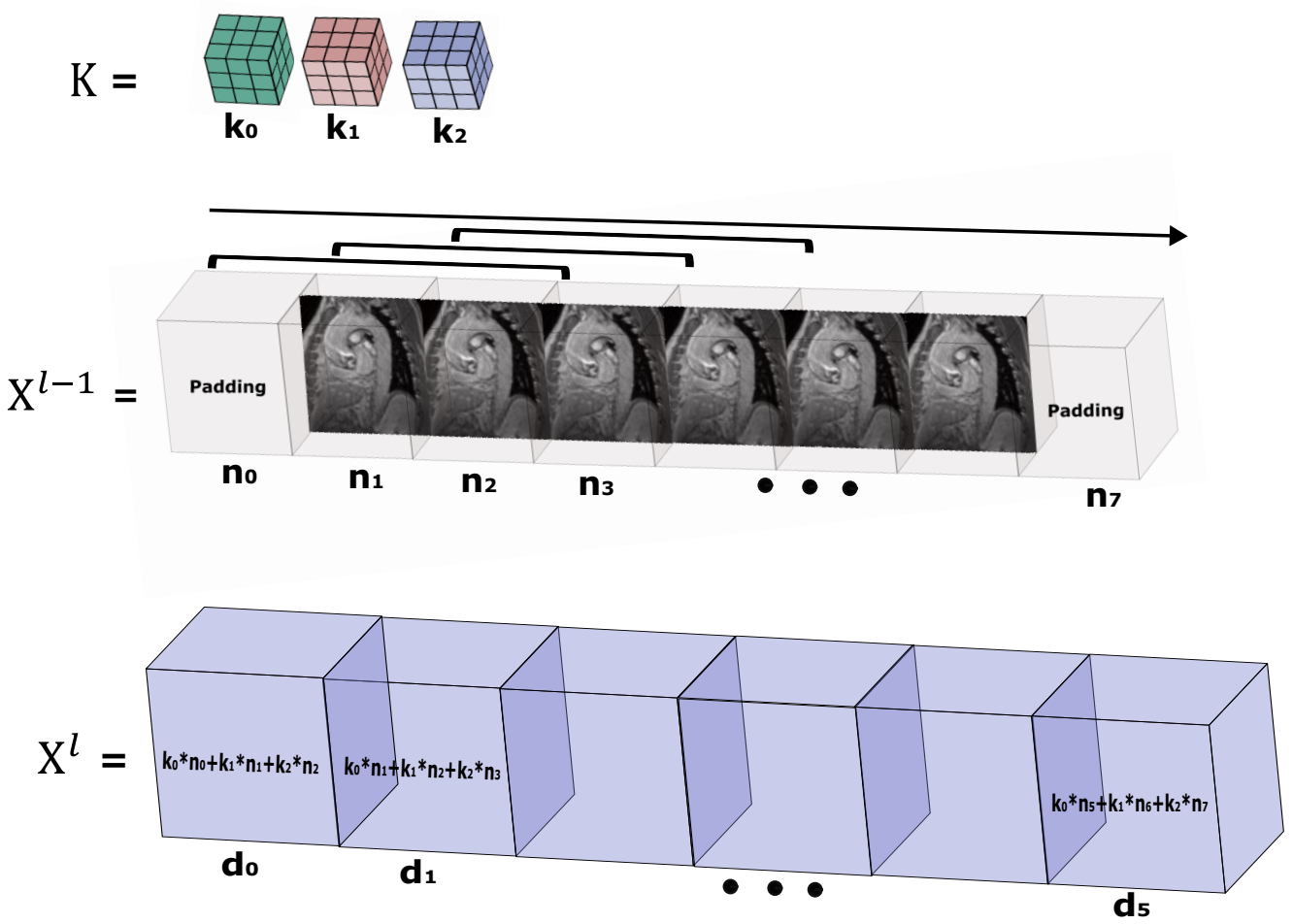

Figure 6.3: Representation of 4D convolution based on 3D convolutions. The representation shows the convolution of a 4D image X^{l-1} with padding and a kernel K of size 3x3x3x3. The symbol $*$ represents the 3D convolution operation between a frame and one of the temporal components of the kernel.

6.1.1.2/ GROUP NORMALIZATION

In neural network implementation, batch normalization (BN) is a widely used technique to facilitate optimization and hence model convergence. During the batch normalization process, the feature maps of a mini-batch are normalized using the mean and variance calculated on it. Despite the advantages of applying BN, it has been found that the statistics are inaccurate when the batch is small. Thus, decreasing the batch size results in an increase in the error. A large batch size in training consumes a lot of memory. Considering a 4D CNN model, using large batch size is not possible. Therefore, a group normalization (GN) technique was used in the implemented architecture. In the GN process, the channels are divided into groups within which statistics are calculated, and normalization is performed across these groups. Figure 6.4 represents the BN and GN processes.

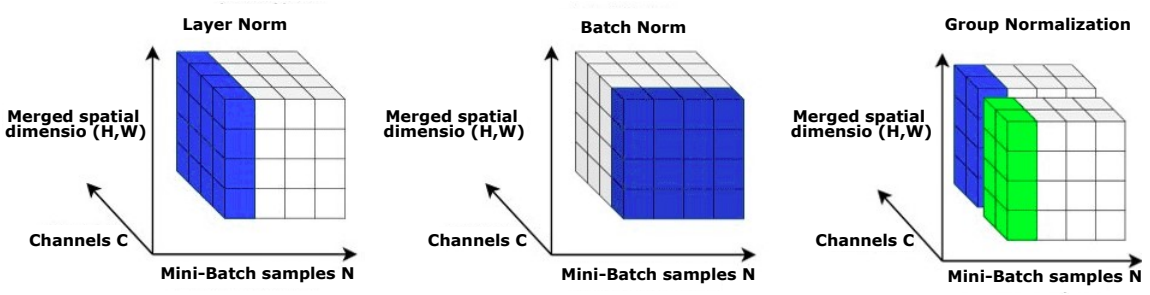

Figure 6.4: Representation with 2D data of the group normalization process

6.1.1.3/ UP-SAMPLING 4D

Sampling operations are used in image processing to change the resolution of the images. Due to the computational cost of deep learning models, particularly 4D models, this technique is used to reduce the output of the layers while keeping the relevant information. In the implemented model, the down-sampling in the encoder path is performed with a stride two convolution. Then, to retrieve the original resolution in the decoder path, it is necessary to use a 4D up-sampling operation. The 3D nearest-neighbor interpolation was applied twice in each of the temporal dimension frames. Thus, the image size is recovered both spatially and temporally.

ALGORITHM 2: 4D up-sampling with native 3D up-sampling

Input : $X^l \in \mathbb{R}^{d_t \text{ x } d_h \text{ x } d_w \text{ x } d_d \text{ x } d_c}$ – Input feature maps

f – scaling factor for up-sampling operation

Output: $X^l_{up} \in \mathbb{R}^{d_t\text{xf x } d_h\text{xf x } d_w\text{xf x } d_d\text{xf}}$ – Output feature maps

$X^l_{up}[d_t\text{xf},\ d_h\text{xf},\ d_w\text{xf},\ d_d\text{xf}] = 0$

t_factor = d_t / $d_t$xf

for i ← 0 : $d_t$xf **do**

  $input\_index_t$ = floor(i x t_factor)

  $X^l_{up}[i :]$ = upsample_nearest3D ($X^l[input\_index_t :]$, f)

end

6.1.1.4/ SPARSE LOSS FUNCTION

The loss function used for training the 4D residual CNN is considered sparse because it uses sparse labeled data in the time dimension. Thus, it is possible to include during the training of the model the 25 frames of each 4D flow MRI image to take advantage of the temporal information during the cardiac cycle. We proposed a normalized version of the loss function originally proposed by Myronenko et al. [87]. The normalized loss function allowed us to obtain proportional ranges of the error contributed for each part that composes it (i.e., Dice loss and time regularization). Equation 6.1 shows the proposed normalized loss function.

$$L = \lambda_1 * \frac{\sum_{i \in label} D(p^i_{true}, p^i_{pred})}{\#label} + \lambda_2 * \frac{\sum_{i=0}^{t-2}(\left\| p^{i+1}_{pred} - p^i_{pred} \right\|)/(h \text{ x } w \text{ x } d)}{t-1}, \tag{6.1}$$

where $\lambda_1 + \lambda_2 = 1$. D represents the soft Dice loss between the target p_{true} and the prediction p_{pred} over the labeled frames images in the 4D flow MRI. t represents the total number of frames acquired over the cardiac cycle (25 in our case) and h, w, and d the spatial resolution. The soft Dice loss function is defined by equation 6.2

$$D(p_{true}, p_{pred}) = 1 - \frac{2 * \sum p_{true} * p_{pred}}{\sum p^2_{true} + \sum p^2_{pred} + \varepsilon}, \tag{6.2}$$

where ϵ is a small value included for numerical stability, in our case, $\epsilon = 1e^{-6}$. p_{true} and p_{pred} represent the manual segmentation and the segmentation generated by the network, respectively.

6.2/ 4D RESIDUAL CNN SETUP

The training of the proposed 4D CNN model is memory-consuming. So, the images were resized to train the model without exceeding the memory limits of the NVIDIA Tesla V100 GPU. We started cropping or padding the images based on the median image size of all patients for the x and y axes and the maximum size on the z-axis. Then, the spacing of the image was modified from 2x2x2 mm^3 to 4x4x4 mm^3, obtaining images of 73x88x22x25 voxels as input to the model. Thus, the voxel-wise predictions per patient was reduced from 28,265,600 voxels to 3,533,200 voxels.

The hyperparameters of the model were established by taking as reference the parameters reported for the original model. Thus, we guarantee the training's convergence while simultaneously avoiding increasing the computational time by performing an exhaustive search for the best set of hyperparameters. In particular, each model was trained for 500 epochs, with an initial learning rate of $1e^{-3}$. A learning rate scheduler strategy was adopted to decrease the learning rate by 10 when validation loss stops improving for 50 epochs. Given the capacity of the used GPU, the batch size was set to four.

As mentioned above, there are two parts in the cost function, each part can be weighted to increase or decrease its contribution during training. Myronenko et al. [87] established a balanced contribution of both terms. Here, we evaluated the influence of establishing different contributions between the two terms by including the parameter λ in the equation. For this purpose, we set a value for λ_1 between zero and one and λ_2 is equal to $1-\lambda_1$. Then, five trainings with the leave-one-patient-out strategy were performed by assigning to λ_1 a value equal to 0.1, 0.2, 0.3, 0.4, or 0.5.

All the automatic segmentations were post-processed frame by frame with a morphological opening filter to smooth out irregularities. A ball structuring element of radius 1 mm was used. In addition, the largest connected component was identified and selected as the final aorta segmentation.

To compare the results of the 4D CNN model with those obtained in chapter 5, the maximum and minimum surface areas in a plane perpendicular to the ascending aorta were calculated in the same way. Pearson correlation of the minimum and maximum surface area values obtained from 4D flow MRI and 2D cine-MRI were calculated, and after testing the normality of the samples with the Shapiro-Wilk test, a paired sample t-test was performed to assess the statistical significance of the measured surfaces. In addition, a one-sample t-test was performed with the differences measured between the surfaces from 4D flow MRI and from cine-MRI. A mean equal to zero is assumed as the null hypothesis. As in the previous chapter, t-test was performed at both 95% and 99% confidence levels. Finally, the maximum and minimum surface areas were compared using the Bland-Altman analysis.

6.3/ 4D CNN SEGMENTATION RESULTS

The training performance curves for three patients with the original model and the proposed model using the same setup are showed in Figures 6.5-6.7. It is important to note that for the three patients, after reaching stability the validation error was lower with the proposed model than with the original one. It can be seen that the performance is comparable and convergence is achieved with both models. A trade-off between bias and variance (Figure 2.3) is obtained even when the second level is removed from the original architecture. The difference in the validation error obtained between the original and proposed models was around 0.01 for two patients and 0.03 for the third one. In particular, Figure 6.7 shows the positive influence of reducing the complexity of the model. For this patient, the variance is increased when the original model is used.

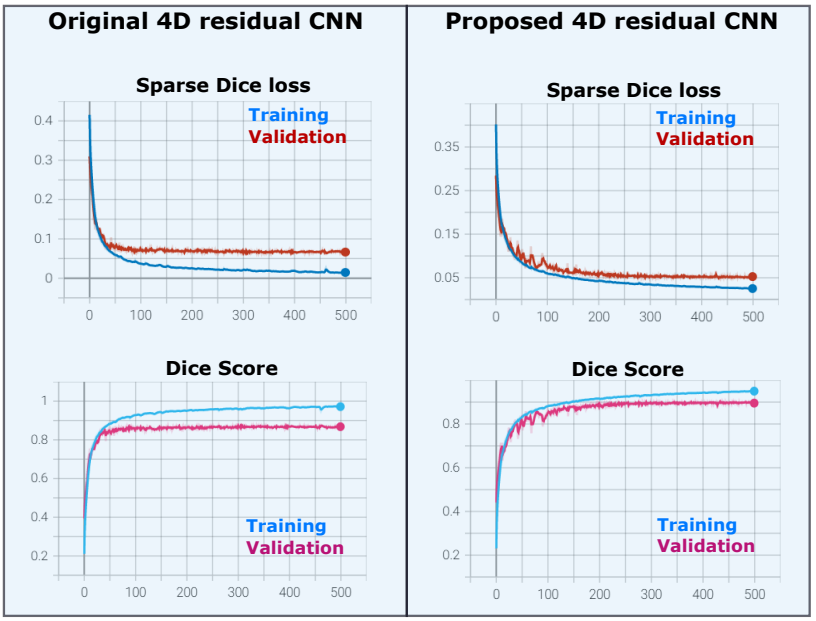

Figure 6.5: Performance of the original and proposed model for patient one

As in the previous chapters, the performance of the 4D CNN model was measured locally and globally with the DSC and the HD. Table 6.1 shows the segmentation result obtained with the different values of λ_1 tested. The best average performance in the database was obtained by giving a higher contribution to the time regularization parameter in the cost function. Precisely, when $\lambda_1 = 0.4$ and $\lambda_2 = 0.6$ were set. Thus, the best overall average DSC obtained was 0.85 ± 0.03, and the best overall average HD was 30.79 ± 29.58. As in the 3D and 4D segmentation methods evaluated in previous chapters, the abdominal aorta is the region with the lowest performance. Considering only the thoracic aorta, an average DSC and HD of 0.86 ± 0.04 and 15.66 ± 13.93 were obtained, respectively (Table 6.2).

Compared to the 4D segmentation results obtained from the segmentation approach applied in chapter 5, poorer results are obtained for both metrics with the 4D CNN model. The prediction time with the trained model is about one minute.

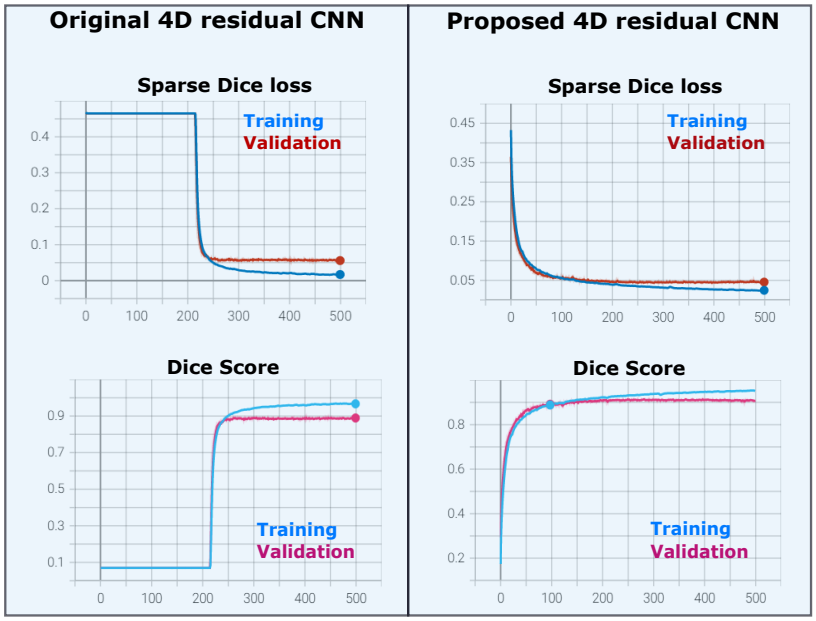

Figure 6.6: Performance of the original and proposed model for patient two

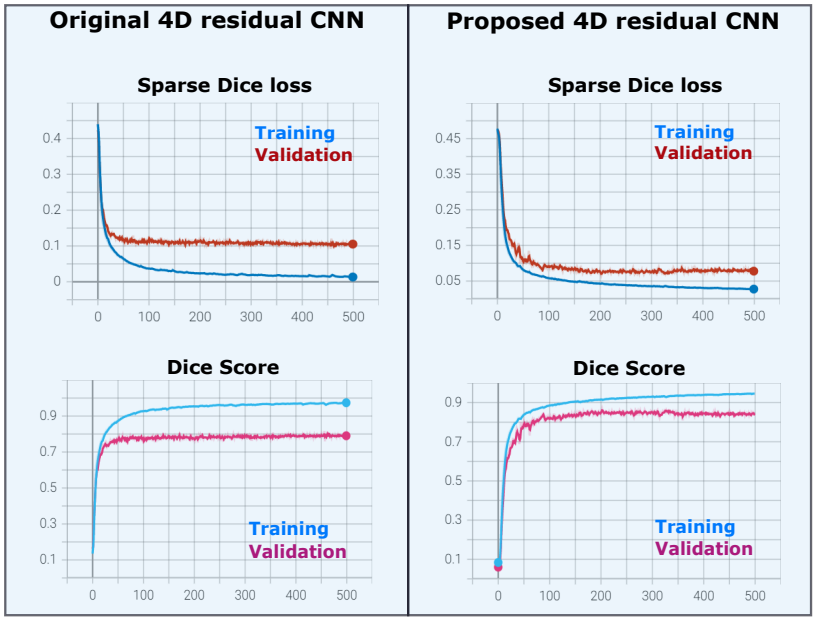

Figure 6.7: Performance of the original and proposed model for patient three

It is important to recall that machine learning algorithms benefit from a large number of training samples. As shown in the analysis of the influence of the amount of training data (section 4.5.2), the 3D U-Net model has the potential to achieve higher performance in aortic segmentation by increasing the number of training samples. Then, 4D CNN could have a lower performance than the 3D U-Net model because the first one is trained with 35 samples and the latter with 175 samples.

For a fairer comparison of 4D CNN performance in terms of number of training

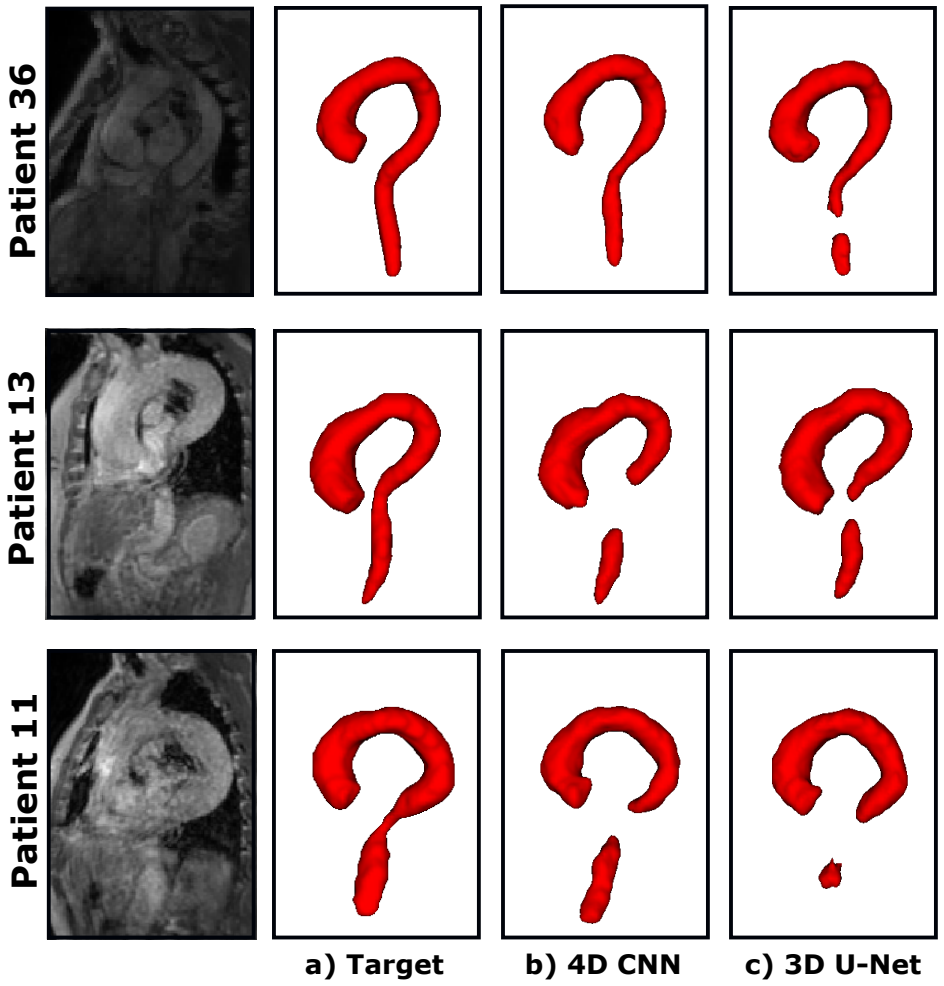

Figure 6.8: 4D CNN and 3D U-Net automatic segmentation results for three patients in a frame of the diastolic phase.

samples, the 3D U-Net model was trained again on 35 samples using leave-one-out validation. For this purpose, the diastolic cardiac phase (frame one) was used as labeled image since, for each patient, at least three of the five segmented frames for 4D CNN training belong to this cardiac phase. This statement is based on the fact that the 4D flow MRI acquisition begins at the end of the ventricular diastole. Systole appears in the first frames of the sequence, and since it lasts for about 30% of the cardiac cycle, it rarely appears in frame 15 and frames 20, and 25 certainly belong to diastole.

Table 6.2 shows the segmentation result of 4D CNN and 3D U-net in frame one, corresponding to the diastole. In addition, the average performance of 4D CNN between the 5 frames is presented. From the results it can be seen that the segmentation performance of 4D CNN and 3D U-net in frame one is comparable with respect to HD and slightly better with U-net with respect to DSC. Particularly, at the PPAo level an improvement is seen in the segmentation performed with 4D CNN. This improvement can also be seen reflected in the average HD obtained in the whole aorta.

Table 6.1: Average performance of the 4D residual CNN with different weights for the loss function.

λ_1	AAo + Arch		TDAo		PAAo		GLOBAL	
	DSC	HD [mm]	DSC	HD [mm]	DSC	HD [mm]	DSC	HD [mm]
0.1	0.85±0.13	15.93±20.35	0.85±0.05	11.05±12.38	0.68±0.19	25.81±21.76	0.84±0.06	36.28±34.15
0.2	0.87±0.03	13.55±8.6	0.83±0.14	10.9±12.72	0.68±0.22	21.62±18.35	0.84±0.06	33.72±34.41
0.3	0.86±0.07	13.77±12.65	0.85±0.05	12.76±14.09	0.63±0.23	28.22±25.58	0.84±0.04	40.86±37.79
0.4	**0.87±0.03**	**12.34±6.87**	**0.85±0.04**	**10.75±13.51**	**0.69±0.18**	**23.15±18.26**	**0.85±0.03**	**30.79±29.58**
0.5	0.87±0.04	12.31±5.7	0.84±0.05	11.55±14.54	0.69±0.18	25.56±20.46	0.84±0.04	33.86±31.99

The automatic segmentation of the aorta with the different deep learning models can be generated with two connected components due to, for example, signal loss at the boundary between TDAo and PAAo. With the post-processing applied to the segmentation the smaller connected component representing the aorta is eliminated. For this reason, during the calculation of the metrics, patients in whom the automatic segmentation for the evaluated region was not present were tracked. With both 4D CNN and 3D U-Net, the PAAo of patients 11 and 13 were generated in a connected component that was removed in post-processing. Additionally, with 3D U-Net this same problem occurred for patient 36. Figure 6.8 shows the rendering of the automatic segmentation for these three patients. It can be noticed that despite the problem described above, for patient 11 4D CNN defines better than 3D U-Net the abdominal aorta. Moreover, 4D CNN segmentation for patient 36 was generated with a single connected component without disconnection at the level of the distal TDAo. It is important to mention that 3D U-Net trained with 35 samples increased this type of problem since when trained with 175 samples, only one of the frames from patient 13 was poorly segmented at the PAAo.

The maximum and minimum surfaces obtained from 4D flow MRI and cine-MRI showed a high correlation with a correlation coefficient r of 0.80 and $r = 0.79$, respectively. The regression plots are presented in Figure 6.9.

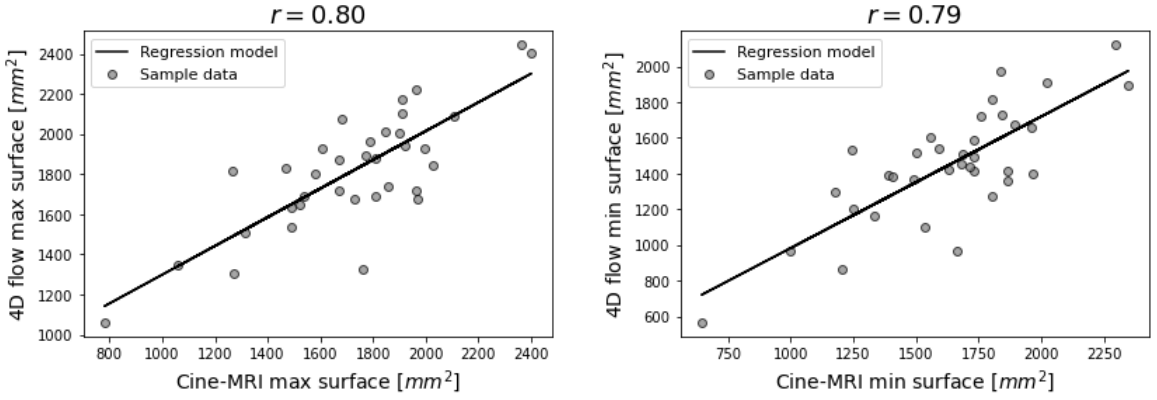

Figure 6.9: Correlation of the maximum and minimum surface calculated from cine-MRI and from 4D flow MRI. r is the correlation coefficient obtained between the surfaces.

The paired t-test with 95% confidence level showed a difference between the max-

Table 6.2: Average performance of the 4D residual CNN and 3D U-Net trained on 35 samples

Model	Local performance of the models					
	AAo+Arch		TDAo		PAAo	
	DSC	HD [mm]	DSC	HD [mm]	DSC	HD [mm]
4D CNN 5 frames	0.87±0.03	12.34±6.87	0.85±0.04	10.75±13.51	0.69±0.18	23.15±18.26
4D CNN Frame 0	86.05±0.05	12.4±4.90	0.85±0.04	10.07±11.56	0.74±0.01	19.51±13.67
3D Unet Frame 0	0.89±0.04	11.03±6.01	0.87±0.03	9.08±8.73	0.76±0.14	20.55±19.89
Model	**Global performance of the models**					
	Thoracic aorta		**Whole aorta**			
	DSC	**HD [mm]**	**DSC**	**HD [mm]**		
4D CNN 5 frames	0.86±0.04	15.66±13.93	0.85±0.03	30.79±29.58		
4D CNN Frame 0	0.86±0.04	14.75±10.76	0.85±0.04	27.57±27.6		
3D Unet Frame 0	0.88±0.03	13.36±9.25	0.87±0.03	29.02±29.92		

- AAo+Arch = Ascending aorta and aortic arch
- TDAo = Thoracic descending aorta
- PAAo = Proximal abdominal aorta
- Thoracic aorta = AAo+Arch and TDAo
- Whole aorta = AAo+Arch, TDAo and PAAo

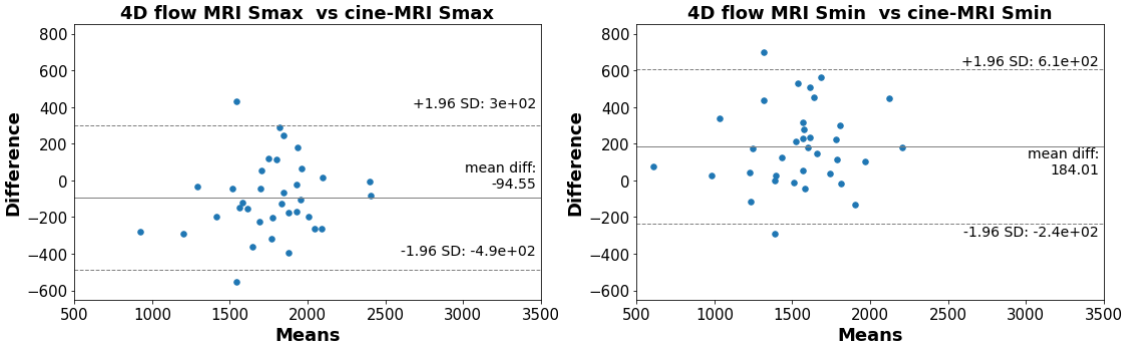

Figure 6.10: Bland-Altman plots of the maximum and minimum surface areas obtained at the level of the ascending aorta during the cardiac cycle.

imum and minimum surface area values obtained with 4D flow and cine-MRI. A p-value of 0.0094 [CI: -164.35 -24.74] was obtained for the maximum surface areas. When comparing minimum surface areas, a p-value< 0.0001 [CI: 108.99 259.07] was obtained. With a 99% confidence level, a p-value=0.0094 [CI: -188.26 -0.82] and a p-value< 0.0001 [CI: 83.29 284.77] were obtained for the maximum and minimum surface area, respectively.

6.4/ DISCUSSION

This chapter presents the results of aortic segmentation from 4D flow MRI using a 4D deep learning model. The benefits of using deep learning models that take advantage of information from different image dimensions have been shown in the literature, but 4D models have been rarely explored due to the lack of frameworks for direct implementation. This is the first time a 4D deep learning model has been tested for the segmentation of the aorta from 4D flow MRI.

Recently, to segment 4D medical images, Myronenko et al. [87] proposed a 4D CNN. In particular, they segmented the left ventricle and myocardium from 4D Coronary computed tomography angiography (CCTA). The performance achieved with the 4D CNN was comparable to that obtained with a 3D model for the DSC metric and better concerning a temporal smoothness metric. In applications such as object tracking through 4D optical coherence tomography (OCT), Bengs et al. [89] have shown that compared to the 3D CNN-based approach, 4D CNN decreased the object localization error by 30%.

For the implementation of 4D segmentation method, the generation of ground truth in 4D is a challenging task. Although automatic and semi-automatic techniques can be adopted for ground truth generation, a careful review is recommended to avoid propagating errors. Moreover, a direct comparison with a human is preferable because it allows exploring the possibility of replacing a segmentation from an expert with an automatic one. Due to the difference in the amount of training data used in the 4D segmentation strategy using 3D U-Net and 4D segmentation using 4D CNN, a direct comparison between the results is biased. So, the 3D U-Net is expected to present a better performance, verified with the segmentation metrics and the maximum and minimum surface analysis.

When a fair comparison is made regarding the number of training samples and cardiac phase used in training 4D CNN and a 3D U-Net models, it was observed that the segmentation performance with 4D CNN is better concerning HD at PAAo and the whole aorta. The post-processing techniques performed are necessary due to the need to smooth the results and eliminate small spurious spots that can dramatically affect the metrics. However, with the post-processing performed, for the patients in which the generated segmentation has two connected components (usually TAo and PAAo), the PAAo is eliminated in the final segmentation. For this reason, three cases were further analyzed before post processing to understand the differences in the segmentations produced with 4D CNN and 3D U-Net for diastole segmentation (Figure 6.8). With this analysis, we found that the aorta for two patients is approximately equally or better defined using 4D CNN. For the third patient (patient 36), 4D CNN obtained a segmentation with a single connected component, and in contrast, 3D U-Net disconnected the abdominal aorta. From these results, we hypothesize that indeed the 4D CNN model could potentially improve and maybe outperform a 4D segmentation based on a 3D U-Net model. Using only 35 training samples, we evidenced its ability to better represent the shape of the aorta in regions prone to errors due to irregular shapes or image

degradation.

The 95% confidence t-test and the 99% confidence level showed differences in calculating the maximum and minimum surface areas from 4d flow MRI and cine-MRI. This suggests that the performance of 4D CNN should be improved to obtain an average score that does not differ significantly between the two modalities.

7

CONCLUSION AND PERSPECTIVES

Our work aimed to develop methods of automatic segmentation of the aorta from 4D flow MRI to extend the use of this sequence in the study of thoracic aortic aneurysms. Currently, the decision to surgically intervene in an aneurysm is made mainly based on the size and growth rate of the aneurysm. However, it has been shown that these parameters are necessary but not completely reliable and that new and better biomarkers should be found and analyzed for personalized diagnoses. Thus, the extension of 4D flow MRI may contribute to generating hemodynamic biomarkers to analyze fluid-structure interactions.

For the development of this work, 36 4D flow MRIs of patients included in the MECATHOR project were used. For each patient, a manual 4D segmentation was generated due to the lack of public 4D flow MRI databases for training and evaluating automatic segmentation algorithms.

Initially, multi-atlas-based and deep learning-based segmentation were evaluated in the aorta segmentation in a systolic phase image since it provides a better contrast of the aorta. The performance of both methods was evaluated with metrics widely used in the image analysis field: the Dice similarity coefficients and the Hausdorff distance. Additionally, the ability of each method to obtain robust wall pressure values compared to those obtained with manually generated models was evaluated. This biomarker was selected because it is less sensitive to changes in the segmentation and is a relevant index for understanding the evolution of the aneurysm since high wall pressure corresponds to high intramural stress exerted on the wall. From these results, we concluded that the U-Net 3D deep learning model is the most suitable for automatic segmentation of the aorta in the systolic phase. Based on this conclusion, the path to aortic segmentation throughout the whole cardiac cycle using deep learning was established.

The first 4D segmentation approach implemented was based on the 3D U-Net model used to segment the systolic phase. For this purpose, the five manually segmented frames for each patient were used to train the model. Compared to the previous training, this strategy can be seen as a type of data augmentation because instead of feeding the model with a single frame for each patient, five frames are provided for each, in which the shape of the aorta changes slightly. Nevertheless, increasing the number of patients in the database is recommended

to include more anatomical variability. Although this approach treats the frames of each patient as independent instances, the segmentation performance showed the feasibility of its use for 4D aortic segmentation of patients with TAA. In addition, a strong correlation of the maximum and minimum surfaces extracted at the level of the ascending aorta with those calculated with cine-MRI was established. The above may give us an idea of the ability of 3D U-Net to adapt to the different shapes of the aorta during the cardiac cycle. In future works, attention mechanisms can be evaluated in the 3D-UNet model, such as the one proposed by Zhou et al. [101], to prioritize the most informative features for segmentation.

The 4D segmentations of the aorta derived from this segmentation approach should be further evaluated in the calculation of biomarkers in order to study their relationship with the progression of thoracic aortic aneurysms. For the cohort of patients in the MECATHOR project, Lin et al. [105] studied the biomechanical properties of the aorta. In particular, the thickness and pre-failure stiffness of the aortic wall were measured by quadrants (anterior, lateral, posterior and medial). Later, the relationship between the pre-failure stiffness with risk factors such as aortic diameter, type of valve or age was established. This result could be studied to analyze the link of the flow patterns and hemodynamic biomarkers with the biomechanical properties reported from the ex-vivo study of the human aortic wall. The MECATHOR project aims to study the thoracic aorta, particularly the ascending aorta. The segmentation results in this region were better than those obtained when the entire aorta was considered. However, it is necessary to improve the segmentation of the aortic valve. For simulation purposes, approaches that model the valve or are designed to analyze the ascending aorta after junction may be considered.

The second approach applied for 4D segmentation of the aorta was based on a proposed 4D CNN model. Overall, the 4D segmentation of the aorta based on 3D U-Net presented a better performance. However, the 4D model is affected by the reduced number of training samples. Comparable performance was achieved when we compared 4D CNN to the 3D U-Net for diastolic segmentation using the same number of training samples. From the results of this comparison, it could be concluded that the 4D model can potentially improve its performance with increasing training samples. Furthermore, by analyzing particular cases, it seems that treating temporal information with the 4D CNN model contributes to a better segmentation of particularly challenging regions such as the abdominal aorta. Further evaluation of this model can be addressed in the future by including more patients in the database. In addition, a patch-based training strategy could be evaluated [58]. Although this strategy increases variability, for example in the location of the organ of interest in the image, its impact and benefit as a data augmentation strategy should be addressed.

The results obtained with deep learning models in segmenting the aorta from 4D flow MRI also encourage the exploration of other models, such as Long short-term memory (LSTM). In a previous study, Gao et al. [73] explored this model for segmenting the brain from MRIs acquired in a longitudinal study. Together these

images are viewed as a 4D sequence. Moreover, the use of transform networks such as those proposed by Dhamija et al. [103] for medical image segmentation could be considered. These models use local and global features by combining transformer-based and convolution-based encoders to improve the segmentation quality.

As for the time required for segmenting a new patient, 4D CNN needs about 50 seconds more than 3D U-Net. However, at the current research stage, both times are acceptable to obtain a 4D segmentation. A graphical user interface will be set up in the future for a straightforward implementation of the proposed methods by the different members of the research team.

The database should be augmented to include anatomical variability in the algorithms and increase their predictive capacity, but also to analyze the performance in healthy patients or on images taken in several centers. Moreover, for a more accurate evaluation of automatic segmentation methods and a fair comparison with expert segmentation, the reasons for the significant differences between observers should be reviewed in detail. Although rules were initially established to try to cover possible biases, the differences were large at the level of the valve and abdominal aorta.

One of the reasons for noise presence in 4D flow MRI is the artifacts generated by patient motion during acquisition. 4D flow MRI is affected by this type of problem because the acquisition time is high compared to sequences such as 2D cine-MRI or MRI angiography. As a long-term work, a new 4D acquisition flow technique based on compressed sensing could be used. This technique can reduce the acquisition time by a factor of three to four. Another possible long-term work is the extension of the applied methods to 4D flow MRI images targeted at the abdominal aorta. Furthermore, the segmentation methods could be extended to similar applications that require segmentation from 4D flow MRI. For example, the study of pathologies in the pulmonary artery or heart.

BIBLIOGRAPHY

[1] BLAIR, R. C., AND HIGGINS, J. J. **The power of t and wilcoxon statistics: A comparison**. *Evaluation Review 4*, 5 (1980), 645–656.

[2] ROYSTON, P. **Approximating the shapiro-wilk w-test for non-normality**. *Statistics and computing 2*, 3 (1992), 117–119.

[3] HUTTENLOCHER, D. P., KLANDERMAN, G. A., AND RUCKLIDGE, W. J. **Comparing images using the hausdorff distance**. *IEEE Transactions on pattern analysis and machine intelligence 15*, 9 (1993), 850–863.

[4] RUMELHART, D. E., DURBIN, R., GOLDEN, R., AND CHAUVIN, Y. **Backpropagation: The basic theory**. *Backpropagation: Theory, architectures and applications* (1995), 1–34.

[5] COADY, M. A., RIZZO, J. A., HAMMOND, G. L., MANDAPATI, D., DARR, U., KOPF, G. S., AND ELEFTERIADES, J. A. **What is the appropriate size criterion for resection of thoracic aortic aneurysms?** *The Journal of thoracic and cardiovascular surgery 113*, 3 (1997), 476–491.

[6] MITCHELL, T. M., AND MITCHELL, T. M. **Machine learning**, vol. 1. McGraw-hill New York, 1997.

[7] CLOUSE, W. D., HALLETT JR, J. W., SCHAFF, H. V., GAYARI, M. M., ILSTRUP, D. M., AND MELTON III, L. J. **Improved prognosis of thoracic aortic aneurysms: a population-based study**. *Jama 280*, 22 (1998), 1926–1929.

[8] SHANEWISE, J. S., CHEUNG, A. T., ARONSON, S., STEWART, W. J., WEISS, R. L., MARK, J. B., SAVAGE, R. M., SEARS-ROGAN, P., MATHEW, J. P., QUIÑONES, M. A., AND OTHERS. **Ase/sca guidelines for performing a comprehensive intraoperative multiplane transesophageal echocardiography examination: recommendations of the american society of echocardiography council for intraoperative echocardiography and the society of cardiovascular anesthesiologists task force for certification in perioperative transesophageal echocardiography**. *Journal of the American Society of Echocardiography 12*, 10 (1999), 884–900.

[9] SHORE, A. C. **Capillaroscopy and the measurement of capillary pressure**. *British journal of clinical pharmacology 50*, 6 (2000), 501–513.

[10] CHUNG, T., AND OTHERS. **Computational fluid dynamics**. Cambridge university press, 2002.

[11] SVENSSON, L. G., AND KHITIN, L. **Aortic cross-sectional area-height ratio timing of aortic surgery in asymptomatic patients with marfan syndrome**. *The Journal of thoracic and cardiovascular surgery 123*, 2 (2002), 360–361.

[12] SVENSSON, L. G., KIM, K.-H., LYTLE, B. W., AND COSGROVE, D. M. **Relationship of aortic cross-sectional area to height ratio and the risk of aortic dissection in patients with bicuspid aortic valves**. *The Journal of thoracic and cardiovascular surgery 126*, 3 (2003), 892–893.

[13] WANG, Z., BOVIK, A. C., SHEIKH, H. R., AND SIMONCELLI, E. P. **Image quality assessment: from error visibility to structural similarity**. *IEEE transactions on image processing 13*, 4 (2004), 600–612.

[14] WARFIELD, S. K., ZOU, K. H., AND WELLS, W. M. **Simultaneous truth and performance level estimation (staple): an algorithm for the validation of image segmentation**. *IEEE transactions on medical imaging 23*, 7 (2004), 903–921.

[15] EL KHOURY, G., GLINEUR, D., RUBAY, J., VERHELST, R., D'ACOZ, Y. D., PONCELET, A., ASTARCI, P., NOIRHOMME, P., AND VAN DYCK, M. **Functional classification of aortic root/valve abnormalities and their correlation with etiologies and surgical procedures**. *Current opinion in cardiology 20*, 2 (2005), 115–121.

[16] ISSELBACHER, E. M. **Thoracic and abdominal aortic aneurysms**. *Circulation 111*, 6 (2005), 816–828.

[17] JUDGE, D. P., AND DIETZ, H. C. **Marfan's syndrome**. *The Lancet 366*, 9501 (2005), 1965–1976.

[18] HECKEMANN, R. A., HAJNAL, J. V., ALJABAR, P., RUECKERT, D., AND HAMMERS, A. **Automatic anatomical brain mri segmentation combining label propagation and decision fusion**. *NeuroImage 33*, 1 (2006), 115–126.

[19] YUSHKEVICH, P. A., PIVEN, J., HAZLETT, H. C., SMITH, R. G., HO, S., GEE, J. C., AND GERIG, G. **User-guided 3d active contour segmentation of anatomical structures: significantly improved efficiency and reliability**. *Neuroimage 31*, 3 (2006), 1116–1128.

[20] ZHU, L., VRANCKX, R., VAN KIEN, P. K., LALANDE, A., BOISSET, N., MATHIEU, F., WEGMAN, M., GLANCY, L., GASC, J.-M., BRUNOTTE, F., AND OTHERS. **Mutations in myosin heavy chain 11 cause a syndrome associating thoracic aortic aneurysm/aortic dissection and patent ductus arteriosus**. *Nature genetics 38*, 3 (2006), 343–349.

[21] BOCK, J., WIEBEN, O., JOHNSON, K., HENNIG, J., AND MARKL, M. **Optimal processing to derive static pc-mra from time-resolved 3d pc-mri data**. *Imaging 25* (2007), 824–831.

[22] PAPE, L. A., TSAI, T. T., ISSELBACHER, E. M., OH, J. K., O'GARA, P. T., EVANGELISTA, A., FATTORI, R., MEINHARDT, G., TRIMARCHI, S., BOSSONE, E., AND OTHERS. **Aortic diameter≥ 5.5 cm is not a good predictor of type a aortic dissection: observations from the international registry of acute aortic dissection**. *Circulation 116*, 10 (2007), 1120–1127.

[23] TAMÁS, É., AND NYLANDER, E. **Echocardiographic description of the anatomic relations within the normal aortic root**. *The Journal of heart valve disease 16*, 3 (2007), 240–246.

[24] ARTAECHEVARRIA, X., MUÑOZ-BARRUTIA, A., AND ORTIZ-DE SOLÓRZANO, C. **Efficient classifier generation and weighted voting for atlas-based segmentation: Two small steps faster and closer to the combination oracle**. In *Medical Imaging 2008: Image Processing* (2008), vol. 6914, SPIE, pp. 639–647.

[25] KLEIN, S., VAN DER HEIDE, U. A., LIPS, I. M., VAN VULPEN, M., STARING, M., AND PLUIM, J. P. **Automatic segmentation of the prostate in 3d mr images by atlas matching using localized mutual information**. *Medical physics 35*, 4 (2008), 1407–1417.

[26] KWONG, R. Y., JEROSCH-HEROLD, M., AND HEYDARI, B. **Cardiovascular magnetic resonance imaging**. Springer, 2008.

[27] MIYAZAKI, M., AND LEE, V. S. **Nonenhanced mr angiography**. *Radiology 248*, 1 (2008), 20–43.

[28] ARTAECHEVARRIA, X., MUNOZ-BARRUTIA, A., AND ORTIZ-DE SOLORZANO, C. **Combination strategies in multi-atlas image segmentation: application to brain mr data**. *IEEE transactions on medical imaging 28*, 8 (2009), 1266–1277.

[29] ISGUM, I., STARING, M., RUTTEN, A., PROKOP, M., VIERGEVER, M. A., AND VAN GINNEKEN, B. **Multi-atlas-based segmentation with local decision fusion—application to cardiac and aortic segmentation in ct scans**. *IEEE transactions on medical imaging 28*, 7 (2009), 1000–1010.

[30] KLEIN, S., STARING, M., MURPHY, K., VIERGEVER, M. A., AND PLUIM, J. P. **Elastix: a toolbox for intensity-based medical image registration**. *IEEE transactions on medical imaging 29*, 1 (2009), 196–205.

[31] BARRETT, K. E., BOITANO, S., BARMAN, S. M., AND BROOKS, H. L. **Ganong's review of medical physiology twenty**.

[32] BRYAN, R., MOHAN, P. S., HOPKINS, A., GALLOWAY, F., TAYLOR, M., AND NAIR, P. B. **Statistical modelling of the whole human femur incorporating geometric and material properties**. *Medical engineering & physics 32*, 1 (2010), 57–65.

[33] GÜLSÜN, M. A., AND TEK, H. **Segmentation of carotid arteries by graph-cuts using centerline models**. In *Medical Imaging 2010: Visualization, Image-Guided Procedures, and Modeling* (2010), vol. 7625, SPIE, pp. 948–955.

[34] SABUNCU, M. R., YEO, B. T., VAN LEEMPUT, K., FISCHL, B., AND GOLLAND, P. **A generative model for image segmentation based on label fusion**. *IEEE transactions on medical imaging 29*, 10 (2010), 1714–1729.

[35] COZIJNSEN, L., BRAAM, R. L., WAALEWIJN, R. A., SCHEPENS, M. A., LOEYS, B. L., VAN OOSTERHOUT, M. F., BARGE-SCHAAPVELD, D. Q., AND MULDER, B. J. **What is new in dilatation of the ascending aorta? review of current literature and practical advice for the cardiologist**. *Circulation 123*, 8 (2011), 924–928.

[36] HENNEMUTH, A., FRIMAN, O., SCHUMANN, C., BOCK, J., DREXL, J., HÜLLEBRAND, M., MARKL, M., AND PEITGEN, H.-O. **Fast interactive exploration of 4d mri flow data**. In *Medical Imaging 2011: Visualization, Image-Guided Procedures, and Modeling* (2011), vol. 7964, SPIE, pp. 110–120.

[37] MICHELENA, H. I., KHANNA, A. D., MAHONEY, D., MARGARYAN, E., TOPILSKY, Y., SURI, R. M., EIDEM, B., EDWARDS, W. D., SUNDT, T. M., AND ENRIQUEZ-SARANO, M. **Incidence of aortic complications in patients with bicuspid aortic valves**. *Jama 306*, 10 (2011), 1104–1112.

[38] MARKL, M., FRYDRYCHOWICZ, A., KOZERKE, S., HOPE, M., AND WIEBEN, O. **4d flow mri**. *Journal of Magnetic Resonance Imaging 36*, 5 (2012), 1015–1036.

[39] VAN PELT, R., NGUYEN, H., TER HAAR ROMENY, B., AND VILANOVA, A. **Automated segmentation of blood-flow regions in large thoracic arteries using 3d-cine pc-mri measurements**. *International journal of computer assisted radiology and surgery 7*, 2 (2012), 217–224.

[40] AYDIN, A., DESAI, N., BERNHARDT, A. M., TREEDE, H., DETTER, C., SHEIKHZADEH, S., RYBCZYNSKI, M., HILLEBRAND, M., LORENZEN, V., MORTENSEN, K., AND OTHERS. **Ascending aortic aneurysm and aortic valve dysfunction in bicuspid aortic valve disease**. *International journal of cardiology 164*, 3 (2013), 301–305.

[41] STALDER, A. F., GULSUN, M. A., GREISER, A., AND JOLLY, M.-P. **Fully automatic visualization of 4d flow data**. In *Proc Intl Soc Mag Reson Med* (2013), vol. 21, p. 1434.

[42] COLLINS, J. A., MUNOZ, J.-V., PATEL, T. R., LOUKAS, M., AND TUBBS, R. S. **The anatomy of the aging aorta**. *Clinical anatomy 27*, 3 (2014), 463–466.

[43] MEMBERS, A. F., ERBEL, R., ABOYANS, V., BOILEAU, C., BOSSONE, E., BARTOLOMEO, R. D., EGGEBRECHT, H., EVANGELISTA, A., FALK, V., FRANK, H., AND OTHERS. **2014 esc guidelines on the diagnosis and treatment of aortic diseases: document covering acute and chronic aortic diseases of the thoracic and abdominal aorta of the adult the task force for the diagnosis and treatment of aortic diseases of the european society of cardiology ESC**. *European heart journal 35*, 41 (2014), 2873–2926.

[44] ROTH, H. R., LU, L., SEFF, A., CHERRY, K. M., HOFFMAN, J., WANG, S., LIU, J., TURKBEY, E., AND SUMMERS, R. M. **A new 2.5 d representation for lymph node detection using random sets of deep convolutional neural network observations**. In *International conference on medical image computing and computer-assisted intervention* (2014), Springer, pp. 520–527.

[45] STANKOVIC, Z., ALLEN, B. D., GARCIA, J., JARVIS, K. B., AND MARKL, M. **4d flow imaging with mri**. *Cardiovascular diagnosis and therapy 4*, 2 (2014), 173.

[46] ADAMO, L., AND BRAVERMAN, A. C. **Surgical threshold for bicuspid aortic valve aneurysm: a case for individual decision-making**. *Heart 101*, 17 (2015), 1361–1367.

[47] BERGEN, R. V., LIN, H.-Y., ALEXANDER, M. E., AND BIDINOSTI, C. P. **4d mr phase and magnitude segmentations with gpu parallel computing**. *Magnetic Resonance Imaging 33*, 1 (2015), 134–145.

[48] BUSTAMANTE, M., PETERSSON, S., ERIKSSON, J., ALEHAGEN, U., DYVERFELDT, P., CARLHÄLL, C.-J., AND EBBERS, T. **Atlas-based analysis of 4d flow cmr: automated vessel segmentation and flow quantification**. *Journal of Cardiovascular Magnetic Resonance 17*, 1 (2015), 1–12.

[49] GUZZARDI, D. G., BARKER, A. J., VAN OOIJ, P., MALAISRIE, S. C., PUTHUMANA, J. J., BELKE, D. D., MEWHORT, H. E., SVYSTONYUK, D. A., KANG, S., VERMA, S., AND OTHERS. **Valve-related hemodynamics mediate human bicuspid aortopathy: insights from wall shear stress mapping**. *Journal of the American College of Cardiology 66*, 8 (2015), 892–900.

[50] IGLESIAS, J. E., AND SABUNCU, M. R. **Multi-atlas segmentation of biomedical images: a survey**. *Medical image analysis 24*, 1 (2015), 205–219.

[51] KENNY, C., AND MONAGHAN, M. **How to assess aortic annular size before transcatheter aortic valve implantation (tavi): the role of echocardiography compared with other imaging modalities**. *Heart 101*, 9 (2015), 727–736.

[52] LAI, M. **Deep learning for medical image segmentation**. *arXiv preprint arXiv:1505.02000* (2015).

[53] LALANDE, A., GARREAU, M., AND FROUIN, F. **Multi-modality cardiac imaging: processing and analysis**. John Wiley & Sons, 2015.

[54] RONNEBERGER, O., FISCHER, P., AND BROX, T. **U-net: Convolutional networks for biomedical image segmentation**. In *International Conference on Medical image computing and computer-assisted intervention* (2015), Springer, pp. 234–241.

[55] SALIBA, E., SIA, Y., DORE, A., AND EL HAMAMSY, I. **The ascending aortic aneurysm: When to intervene?** *IJC Heart & Vasculature 6* (2015), 91–100.

[56] TAHA, A. A., AND HANBURY, A. **Metrics for evaluating 3d medical image segmentation: analysis, selection, and tool**. *BMC medical imaging 15*, 1 (2015), 1–28.

[57] ÇIÇEK, Ö., ABDULKADIR, A., LIENKAMP, S. S., BROX, T., AND RONNEBERGER, O. **3d u-net: learning dense volumetric segmentation from sparse annotation**. In *International conference on medical image computing and computer-assisted intervention* (2016), Springer, pp. 424–432.

[58] CUI, Z., YANG, J., AND QIAO, Y. **Brain mri segmentation with patch-based cnn approach**. In *2016 35th Chinese Control Conference (CCC)* (2016), IEEE, pp. 7026–7031.

[59] DI CESARE, E., SPLENDIANI, A., BARILE, A., SQUILLACI, E., DI CESARE, A., BRUNESE, L., AND MASCIOCCHI, C. **Ct and mr imaging of the thoracic aorta**. *Open Medicine 11*, 1 (2016), 143–151.

[60] HA, H., KIM, G. B., KWEON, J., LEE, S. J., KIM, Y.-H., LEE, D. H., YANG, D. H., AND KIM, N. **Hemodynamic measurement using four-dimensional phase-contrast mri: quantification of hemodynamic parameters and clinical applications**. *Korean journal of radiology 17*, 4 (2016), 445–462.

[61] INDRAKUSUMA, R., JALALZADEH, H., PLANKEN, R., MARQUERING, H., LEGEMATE, D., KOELEMAY, M., AND BALM, R. **Biomechanical imaging markers as predictors of abdominal aortic aneurysm growth or rupture: a systematic review**. *European Journal of Vascular and Endovascular Surgery 52*, 4 (2016), 475–486.

[62] KÖHLER, B., PREIM, U., GROTHOFF, M., GUTBERLET, M., FISCHBACH, K., AND PREIM, B. **Robust cardiac function assessment in 4d pc-mri data of the aorta and pulmonary artery**. In *Computer Graphics Forum* (2016), vol. 35, Wiley Online Library, pp. 32–43.

[63] LADICH, E., BUTANY, J., AND VIRMANI, R. **Aneurysms of the aorta: ascending, thoracic and abdominal and their management**. In *Cardiovascular pathology*. Elsevier, 2016, pp. 169–211.

[64] MARWAN, M., AND ACHENBACH, S. **Role of cardiac ct before transcatheter aortic valve implantation (tavi)**. *Current cardiology reports 18*, 2 (2016), 1–9.

[65] PESHKOVA, I. O., SCHAEFER, G., AND KOLTSOVA, E. K. **Atherosclerosis and aortic aneurysm–is inflammation a common denominator?** *The FEBS journal 283*, 9 (2016), 1636–1652.

[66] RUDER, S. **An overview of gradient descent optimization algorithms**. *arXiv preprint arXiv:1609.04747* (2016).

[67] VAN DERLINDE, D., ROOS-HESSELINK, J., BART, L., AND OTHERS. **Aneurysms-Osteoarthritis Syndrome: SMAD3 Gene Mutations**. Elsevier, 2016.

[68] VOLONGHI, P., TRESOLDI, D., CADIOLI, M., USUELLI, A. M., PONZINI, R., MORBIDUCCI, U., ESPOSITO, A., AND RIZZO, G. **Automatic extraction of three-dimensional thoracic aorta geometric model from phase contrast mri for morphometric and hemodynamic characterization**. *Magnetic Resonance in Medicine 75*, 2 (2016), 873–882.

[69] AKKUS, Z., GALIMZIANOVA, A., HOOGI, A., RUBIN, D. L., AND ERICKSON, B. J. **Deep learning for brain mri segmentation: state of the art and future directions**. *Journal of digital imaging 30*, 4 (2017), 449–459.

[70] LITJENS, G., KOOI, T., BEJNORDI, B. E., SETIO, A. A. A., CIOMPI, F., GHAFOORIAN, M., VAN DER LAAK, J. A., VAN GINNEKEN, B., AND SÁNCHEZ, C. I. **A survey on deep learning in medical image analysis**. *Medical image analysis 42* (2017), 60–88.

[71] PASTA, S., GENTILE, G., RAFFA, G., BELLAVIA, D., CHIARELLO, G., LIOTTA, R., LUCA, A., SCARDULLA, C., AND PILATO, M. **In silico shear and intramural stresses are linked to aortic valve morphology in dilated ascending aorta**. *European Journal of Vascular and Endovascular Surgery 54*, 2 (2017), 254–263.

[72] BUSTAMANTE, M., GUPTA, V., FORSBERG, D., CARLHÄLL, C.-J., ENGVALL, J., AND EBBERS, T. **Automated multi-atlas segmentation of cardiac 4d flow mri**. *Medical image analysis 49* (2018), 128–140.

[73] GAO, Y., PHILLIPS, J. M., ZHENG, Y., MIN, R., FLETCHER, P. T., AND GERIG, G. **Fully convolutional structured lstm networks for joint 4d medical image segmentation**. In *2018 IEEE 15th International Symposium on Biomedical Imaging (ISBI 2018)* (2018), IEEE, pp. 1104–1108.

[74] HÄNSCH, A., SCHWIER, M., GASS, T., MORGAS, T., HAAS, B., DICKEN, V., MEINE, H., KLEIN, J., AND HAHN, H. K. **Evaluation of deep learning methods for parotid gland segmentation from ct images**. *Journal of Medical Imaging 6*, 1 (2018), 011005.

[75] JANSSENS, R., ZENG, G., AND ZHENG, G. **Fully automatic segmentation of lumbar vertebrae from ct images using cascaded 3d fully convolutional networks**. In *2018 IEEE 15th international symposium on biomedical imaging (ISBI 2018)* (2018), IEEE, pp. 893–897.

[76] MITÉRAN, J., BOUCHOT, O., COCHET, A., AND LALANDE, A. **Automatic determination of aortic compliance based on mri and adapted curvilinear detector**. *Biomedical Signal Processing and Control 40* (2018), 295–311.

[77] RODRÍGUEZ-PALOMARES, J. F., DUX-SANTOY, L., GUALA, A., KALE, R., MALDONADO, G., TEIXIDÓ-TURÀ, G., GALIAN, L., HUGUET, M., VALENTE, F., GUTIÉRREZ, L., AND OTHERS. **Aortic flow patterns and wall shear stress maps by 4d-flow cardiovascular magnetic resonance in the assessment of aortic dilatation in bicuspid aortic valve disease**. *Journal of Cardiovascular Magnetic Resonance 20*, 1 (2018), 1–15.

[78] YAMASHITA, R., NISHIO, M., DO, R. K. G., AND TOGASHI, K. **Convolutional neural networks: an overview and application in radiology**. *Insights into imaging 9*, 4 (2018), 611–629.

[79] YEGHIAZARYAN, V., AND VOICULESCU, I. **Family of boundary overlap metrics for the evaluation of medical image segmentation**. *Journal of Medical Imaging 5*, 1 (2018).

[80] BARRAL, P.-A., DEMASI-JACQUIER, M., BAL, L., OMNES, V., BARTOLI, A., PIQUET, P., JACQUIER, A., AND GAUDRY, M. **Fusion imaging to guide thoracic endovascular aortic repair (tevar): a randomized comparison of two methods, 2d/3d versus 3d/3d image fusion**. *CardioVascular and Interventional Radiology 42*, 11 (2019), 1522–1529.

[81] CLOUGH, J. R., BYRNE, N., OKSUZ, I., ZIMMER, V. A., SCHNABEL, J. A., AND KING, A. P. **A topological loss function for deep-learning based image segmentation using persistent homology**. *arXiv preprint arXiv:1910.01877* (2019).

[82] COURTIAL, N., SIMON, A., DONAL, E., LEDERLIN, M., AND GARREAU, M. **Cardiac cine-mri/ct registration for interventions planning**. In *2019 IEEE 16th International Symposium on Biomedical Imaging (ISBI 2019)* (2019), IEEE, pp. 776–779.

[83] DE PAULIS, R., AND SALICA, A. **Surgical anatomy of the aortic valve and root—implications for valve repair**. *Annals of cardiothoracic surgery 8*, 3 (2019), 313.

[84] HESAMIAN, M. H., JIA, W., HE, X., AND KENNEDY, P. **Deep learning techniques for medical image segmentation: achievements and challenges**. *Journal of digital imaging 32*, 4 (2019), 582–596.

[85] KÖHLER, B., GROTHOFF, M., GUTBERLET, M., AND PREIM, B. **Bloodline: A system for the guided analysis of cardiac 4d pc-mri data**. *Computers & Graphics 82* (2019), 32–43.

[86] LU, H., WANG, H., ZHANG, Q., YOON, S. W., AND WON, D. **A 3d convolutional neural network for volumetric image semantic segmentation**. *Procedia Manufacturing 39* (2019), 422–428.

[87] MYRONENKO, A., YANG, D., BUCH, V., XU, D., IHSANI, A., DOYLE, S., MICHALSKI, M., TENENHOLTZ, N., AND ROTH, H. **4d cnn for semantic segmentation of cardiac volumetric sequences**. In *International Workshop on Statistical Atlases and Computational Models of the Heart* (2019), Springer, pp. 72–80.

[88] WEI, W., EVIN, M., RAPACCHI, S., KOBER, F., BERNARD, M., JACQUIER, A., KAHN, C. J., AND BEHR, M. **Investigating heartbeat-related in-plane motion and stress levels induced at the aortic root**. *Biomedical engineering online 18*, 1 (2019), 1–15.

[89] BENGS, M., GESSERT, N., AND SCHLAEFER, A. **4d spatio-temporal convolutional networks for object position estimation in oct volumes**. *Current directions in biomedical engineering 6*, 1 (2020).

[90] BERHANE, H., SCOTT, M., ELBAZ, M., JARVIS, K., MCCARTHY, P., CARR, J., MALAISRIE, C., AVERY, R., BARKER, A. J., ROBINSON, J. D., AND OTHERS. **Fully automated 3d aortic segmentation of 4d flow mri for hemodynamic analysis using deep learning**. *Magnetic resonance in medicine 84*, 4 (2020), 2204–2218.

[91] BIANCOLINI, M. E., CHIAPPA, A., CELLA, U., COSTA, E., GROTH, C., AND PORZIANI, S. **Radial basis functions mesh morphing**. In *International Conference on Computational Science* (2020), Springer, pp. 294–308.

[92] EHRMAN, J. K., FERNANDEZ, A. B., MYERS, J., OH, P., THOMPSON, P. D., AND KETEYIAN, S. J. **Aortic aneurysm: diagnosis, management, exercise testing, and training**. *Journal of Cardiopulmonary Rehabilitation and Prevention 40*, 4 (2020), 215–223.

[93] GABRIELSSON, R. B., NELSON, B. J., DWARAKNATH, A., AND SKRABA, P. **A topology layer for machine learning**. In *International Conference on Artificial Intelligence and Statistics* (2020), PMLR, pp. 1553–1563.

[94] LIANG, L., MAO, W., AND SUN, W. **A feasibility study of deep learning for predicting hemodynamics of human thoracic aorta**. *Journal of biomechanics 99* (2020), 109544.

[95] BOSSONE, E., AND EAGLE, K. A. **Epidemiology and management of aortic disease: aortic aneurysms and acute aortic syndromes**. *Nature Reviews Cardiology 18*, 5 (2021), 331–348.

[96] CASCIARO, M. E., PASCANER, A. F., GUILENEA, F. N., ALCIBAR, J., GENCER, U., SOULAT, G., MOUSSEAUX, E., AND CRAIEM, D. **4d flow mri: impact of region of interest size, angulation and spatial resolution on aortic flow assessment**. *Physiological measurement 42*, 3 (2021), 035004.

[97] FUJIWARA, T., BERHANE, H., SCOTT, M. B., ENGLUND, E. K., SCHÄFER, M., FONSECA, B., BERTHUSEN, A., ROBINSON, J. D., RIGSBY, C. K., BROWNE, L. P., AND OTHERS. **Segmentation of the aorta and pulmonary arteries based on 4d flow mri in the pediatric setting using fully automated multi-site, multi-vendor, and multi-label dense u-net**. *Journal of Magnetic Resonance Imaging* (2021).

[98] HOEIJMAKERS, M., HUBERTS, W., RUTTEN, M., AND VAN DE VOSSE, F. **The impact of shape uncertainty on aortic-valve pressure-drop computations**. *International Journal for Numerical Methods in Biomedical Engineering 37*, 10 (2021), e3518.

[99] JUFFERMANS, J. F., WESTENBERG, J. J., VAN DEN BOOGAARD, P. J., ROEST, A. A., VAN ASSEN, H. C., VAN DER PALEN, R. L., AND LAMB, H. J. **Reproducibility of aorta segmentation on 4d flow mri in healthy volunteers**. *Journal of Magnetic Resonance Imaging 53*, 4 (2021), 1268–1279.

[100] PORZIANI, S., GROTH, C., WALDMAN, W., AND BIANCOLINI, M. E. **Automatic shape optimisation of structural parts driven by bgm and rbf mesh morphing**. *International Journal of Mechanical Sciences 189* (2021), 105976.

[101] ZHOU, T., CANU, S., AND RUAN, S. **Automatic covid-19 ct segmentation using u-net integrated spatial and channel attention mechanism**. *International Journal of Imaging Systems and Technology 31*, 1 (2021), 16–27.

[102] BUSTAMANTE, M., VIOLA, F., ENGVALL, J., CARLHÄLL, C.-J., AND EBBERS, T. **Automatic time-resolved cardiovascular segmentation of 4d flow mri using deep learning**. *Journal of Magnetic Resonance Imaging* (2022).

[103] DHAMIJA, T., GUPTA, A., GUPTA, S., KATARYA, R., SINGH, G., AND OTHERS. **Semantic segmentation in medical images through transfused convolution and transformer networks**. *Applied Intelligence* (2022), 1–17.

[104] FUJIWARA, T., BERHANE, H., SCOTT, M. B., ENGLUND, E. K., SCHÄFER, M., FONSECA, B., BERTHUSEN, A., ROBINSON, J. D., RIGSBY, C. K.,

BROWNE, L. P., AND OTHERS. **Segmentation of the aorta and pulmonary arteries based on 4d flow mri in the pediatric setting using fully automated multi-site, multi-vendor, and multi-label dense u-net**. *Journal of Magnetic Resonance Imaging 55*, 6 (2022), 1666–1680.

[105] LIN, S., MORGANT, M. C., MARÍN-CASTRILLÓN, D. M., WALKER, P. M., GLÉLÉ, L. S. A., BOUCHER, A., PRESLES, B., BOUCHOT, O., AND LALANDE, A. **Aortic local biomechanical properties in ascending aortic aneurysms**. *Acta Biomaterialia 149* (2022), 40–50.

[106] SOULAT, G., SCOTT, M. B., ALLEN, B. D., AVERY, R., BONOW, R. O., MALAISRIE, S. C., MCCARTHY, P., FEDAK, P. W., BARKER, A. J., AND MARKL, M. **Association of regional wall shear stress and progressive ascending aorta dilation in bicuspid aortic valve**. *Cardiovascular Imaging 15*, 1 (2022), 33–42.

III

ANNEXES

A

ADDITIONAL INFORMATION

A.1/ TOPOLOGICAL LOSS FUNCTION FOR DEEP-LEARNING BASED IMAGE SEGMENTATION

A.1.1/ TOPOLOGICAL LOSS FUNCTION USING PERSISTENT HOMOLOGY

In patients with low contrast at the level of the abdominal aorta, the segmentation generated by the different deep learning models represented the aorta as two disconnected components. Recently, James et al. [81] proposed a constraint on the loss function based on prior information about the desired segmentation topology. The objective of this approach is to explicitly set during training the topological features with respect to the number of connected components (β_0), number of holes (β_1), and number of hollow voids (β_2) in the object to be segmented. The topological features of an image are found by generating simplicial complexes with different groups of pixels, chosen by a threshold in the intensity values to be used. A simplicial complex is a set composed of points, line segments, triangles, and their n-dimensional counterparts A.1.

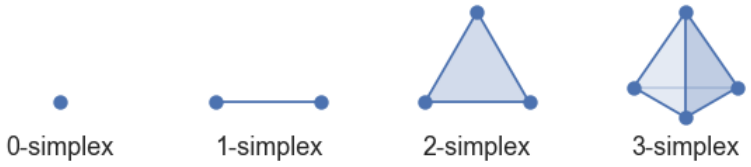

Figure A.1: Representation of simplicial complex in different dimensions. Thus a 0-simplex is a point, a 1-simplex is a line segment (between two zero simplices), a 2-simplex is a triangle (with three 1-simplices as "faces"), and a 3-simplex is a tetrahedron (with four 2-simplices as "faces") Credit: `https://umap-learn.readthedocs.io`

To find the topology of an image, cubical complexes are generated from the data, in our case, from the probability map generated by the deep learning model. A cubical complex is a set of points, unit line segments, unit squares, cubes, hypercubes, etc. To initiate this approach, the topological features of the objects to be segmented must be defined. For example, if you want to segment the numbers from 0 to 9 contained in the images of the MNIST database, you must define the topology of each number:

- Numbers 1, 2, 3, 4, 5 and 7 $\rightarrow \beta_0 = 1, \beta_1 = 0$
- Numbers 6, 9 and 0 $\rightarrow \beta_0 = 1, \beta_1 = 1$
- Number 8 $\rightarrow \beta_0 = 1, \beta_1 = 2$

As the images are 2D, only the first two topologies need to be defined. That is, for $i >= 2,\ \beta_i = 0$. The following figure shows the process of constructing cubical complexes on an image containing the number 0.

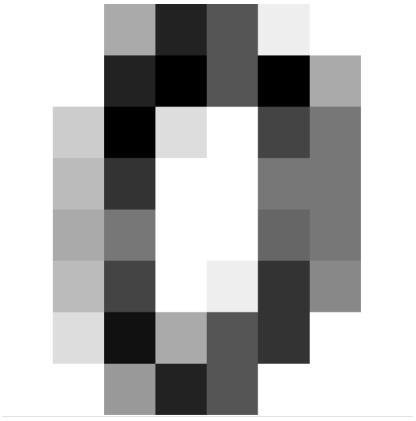

15	15	10	2	5	14	15	15
15	15	2	0	5	0	10	15
15	12	0	13	15	4	7	15
15	11	3	15	15	7	7	15
15	10	7	15	15	6	7	15
15	11	4	15	14	3	8	15
15	13	1	10	5	3	15	15
15	15	9	2	5	15	15	15

Figure A.2: Image of the number zero from which the topological features will be extracted by means of the cubical complexes. The image on the right represents the intensity values of the image.

Features β_0 and β_1 are searched in a set of pixels in the image denoted with an intensity threshold. A threshold equal to 3 is set to start.

Considering values lower or equal to three, five connected components are identified. A threshold equal to seven is then established.

With a threshold equal to seven, only one connected component remains. The start and end of the features are represented by a dot at the ends of the line. In topology, this start and end are called the birth and death of the features. Thus, five features are born with a threshold equal to three, and when the threshold is raised to seven, four of the features die. To continue the process, a threshold equal to ten is set.

When the threshold is set equal to ten the connected component remains and in addition a second level feature appears (β_1), represented by a dashed line. Then,

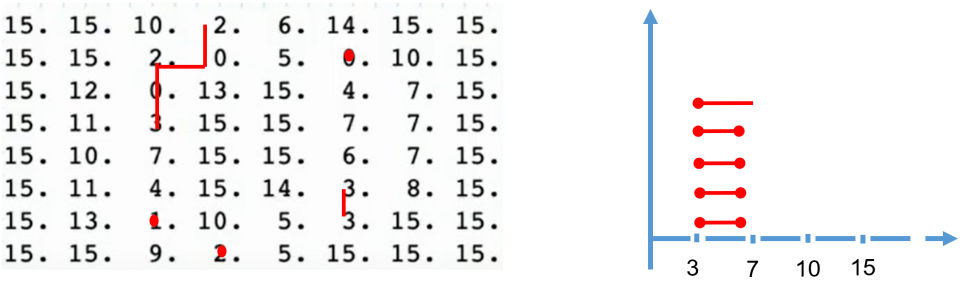

Figure A.3: Representation of the five connected components found with a threshold equal to three.

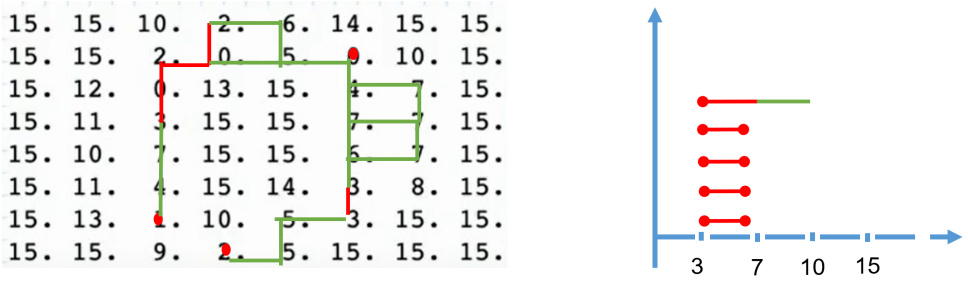

Figure A.4: Representation of the topological features with a threshold equal to seven.

the threshold can be changed until the maximum intensity in the image is reached. The barcode diagram representing the features is known as persistence barcode. The relevant features in this barcode are those that persist for the different tested thresholds or for most of them. In our example, a barcode representing the desired topology of the number zero would have only one line appearing around the first filtering threshold and maintained until the end.

After the barcode calculation using the probability map generated with the deep learning model, the objective of the constrained cost function (Topoloss) is to reduce the number of irrelevant features until a ”perfect” barcode is obtained. The mathematical definition of the Topoloss cost function is given by equations A.1 and equations A.2.

$$L_k(\beta_k) = \sum_{l=1}^{\beta_k}(1 - |b_{k,l} - d_{k,l}|) + \sum_{l=\beta_{k+1}}^{\infty} |b_{k,l} - d_{k,l}|^2 \tag{A.1}$$

where, b and d represent the birth and death of bar l.

$$L_{topo} = \sum_k L_k(\beta_k) \tag{A.2}$$

This loss function can be implemented during the training process as a semi-supervised framework or as a post-processing step on the final prediction provided by the network. In post-processing, the network f is trained in a supervised

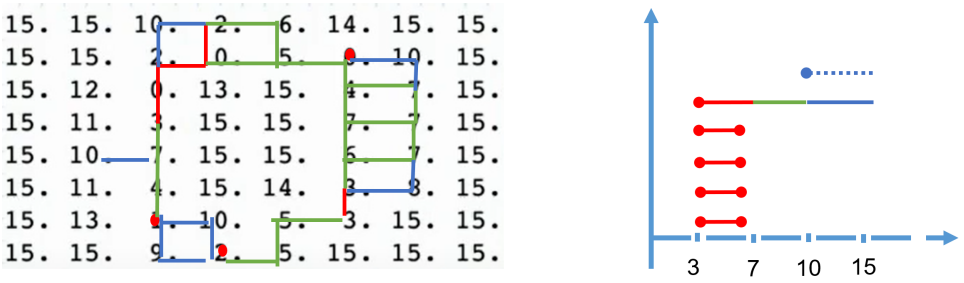

Figure A.5: Representation of the topological features with a threshold equal ten.

way on the training set. The weights ω obtained minimize the loss function, e.g., Dice loss. Then, the topoloss function is optimized on the test examples, creating a set ω_n of updated weights. For each image X_n in the test set, the cost function is as expressed in equation A.3

$$L(X_n; \omega, \omega_n) = \frac{1}{V} |f(X_n, \omega) - f(X_n, \omega_n)|^2 + \lambda L_{topo}(X_n, \omega_n) \tag{A.3}$$

Where V is the number of voxels in the image X_n. This post-processing finds the weights that allow the topology to be modified and corrected taking into account the prior information provided.

In the semi-supervised framework, the network is trained on a subset of images with their respective labels $(X_l,\ Y_l)$, but a set of unlabeled images (X_u) with a defined topology is also used. For the labeled images, a loss function such as the Dice loss can be used, and for the unlabeled images, the topoloss is used, as seen in equation A.4.

$$L(X_l, X_u; \omega) = \sum_{X_l} L_{Dice}(X_l, \omega) + \lambda \sum_{X_u} L_{topo}(X_u) \tag{A.4}$$

A.1.2/ POST-PROCESSING OF AORTIC SEGMENTATION USING TOPOLOSS

The topoloss cost function was used to post-process the segmentations generated in the systolic phase by the 3D U-Net model (section 4.4). Thus, we aimed to restrict the number of components generated by the model to represent the aorta in patients with signal loss in the image. For example, when signal loss was observed for some patients at the distal descending aorta or the abdominal aorta. The topology of the aorta in 3D corresponds to a connected component without loops and without hollow voids. Then, the topological features, $\beta_0 = 1$, $\beta_1 = 0$, and $\beta_2 = 0$, were defined. These features define the prior knowledge we have got about the topology of the object to be segmented.

For the implementation of topoloss as a post-processing strategy, several values

of λ were tested ($\lambda = 0.0001, 0.0003, 0.0004, 0.0005, 0.001, 0.003, 0.004, 0.005$). In the post-processing framework, it is also necessary to define the number of iterations, i.e., the number of times the model weights have to be updated. The number of iterations was set to 60, and during the process, the performance was evaluated at iterations 10, 30, and 60 using the DSC and the HD.

To evaluate the performance of the model's constraint strategy, two patients were used, one of them with signal degradation at the abdominal aortic level. For evaluating this approach, the TopoLayer implemented in Pytorch by Brüel-Gabrielsson et al. [93] was used.

A.1.3/ SEGMENTATION RESULTS FROM POST-PROCESSING WITH TOPOLOSS

In the systolic phase segmentation pipeline, post-processing was applied. The post-processing included the identification of the largest object in the segmentation followed by a morphological opening operation. Topoloss was applied directly at the model output per each patient. The results obtained were compared with those obtained from the initial segmentation of the model and from the post-process segmentation without topoloss (Table A.3). For the patient with degradation at the level of the distal thoracic aorta, the best segmentation result with topoloss was obtained with $\lambda = 0.0004$ in 30 iterations (Table A.2). For the other patient included in the analysis, the best segmentation result with topoloss was obtained with $\lambda = 0.005$ in ten iterations (Table A.1).

Compared to U-Net prediction results, topoloss significantly improves HD for the patient with image degradation at the distal thoracic aorta (patient 1). This improvement occurs because the method manages to eliminate a component that does not belong to the aorta (Figure A.6). However, obtaining a single component including the thoracic and abdominal aorta was impossible using the topoloss. Compared to the post-processing pipeline applied without topoloss, the results of topoloss are much better, but this is due to the fact that the connected component representing the abdominal aorta is removed when the main component search is applied. For patient four, the HD obtained with the topoloss-based post-processing is considerably better with respect to the initial prediction with U-Net. However, the improvement with the post-processing based in the identification of the largest object and the opening is around 2 mm only.

A.1.4/ CONCLUSION

With the post-processing approach based on topoloss, it was observed that it is possible to improve the segmentation and reduce the HD with respect to the initial prediction. Although post-processing with topoloss could not unite the components that are part of the aorta, it was possible to eliminate components that

Table A.1: Post-processing results with topoloss for patient 4

λ	Iteration 10		Iteration 30		Iteration 60	
	DSC	HD [mm]	DSC	HD [mm]	DSC	HD [mm]
0.0001	0.89	29.49	0.89	29.49	0.89	29.49
0.0003	0.89	27.74	0.89	28.60	0.89	29.49
0.0004	0.89	29.49	0.89	29.49	0.89	29.49
0.0005	0.89	26.80	0.89	28.60	0.89	29.49
0.001	0.86	26.80	0.88	27.74	0.89	27.74
0.003	0.89	21.33	0.89	21.54	0.89	21.55
0.004	0.89	25.97	0.88	27.09	0.88	27.74
0.005	**0.88**	**9.49**	0.88	24.03	0.88	18.01

Table A.2: Post-processing results with topoloss for patient 11

λ	Iteration 10		Iteration 30		Iteration 60	
	DSC	HD [mm]	DSC	HD [mm]	DSC	HD [mm]
0.0001	0.82	83.09	0.83	84.79	0.83	83.29
0.0003	0.88	33.19	0.88	38.35	0.88	37.63
0.0004	0.89	34.85	**0.88**	**24.69**	0.88	24.69
0.0005	0.88	35.67	0.88	36.77	0.88	36.56
0.001	0.87	38.30	0.87	34.82	0.88	35.06
0.003	0.87	43.66	0.87	50.09	0.87	43.32
0.004	0.84	47.86	0.82	75.20	0.82	80.26
0.005	0.86	29.57	0.82	45.32	0.81	144.31

Table A.3: Segmentation results with U-Net before and after previous pipeline post-processing.

Approach	Patient 4		Patient 11	
	DSC	HD [mm]	DSC	HD [mm]
U-Net prediction	0.89	29.49	0.88	36.61
U-Net prediction with ”classical ”post-processing	0.90	11.64	0.82	142.45

do not belong to the aorta without eliminating the abdominal part. From this point of view, topoloss helps to reduce the bias in metrics generated by removing components that belong to the aorta.

From the results, it can be said that the λ value and the number of iterations that allow performance improvement are different for each patient. The use of topoloss increases the post-processing time. One iteration can take about one hour. This is due to the process of finding topological features by building the cubical complexes. The topoloss computation time makes optimizing λ and the iterations on the whole database difficult. Thus, it was decided to implement post-processing based on the main object and opening for cost-benefit. It should be noted that the framework proposed by Brüel-Gabrielsson et al. is not optimized.

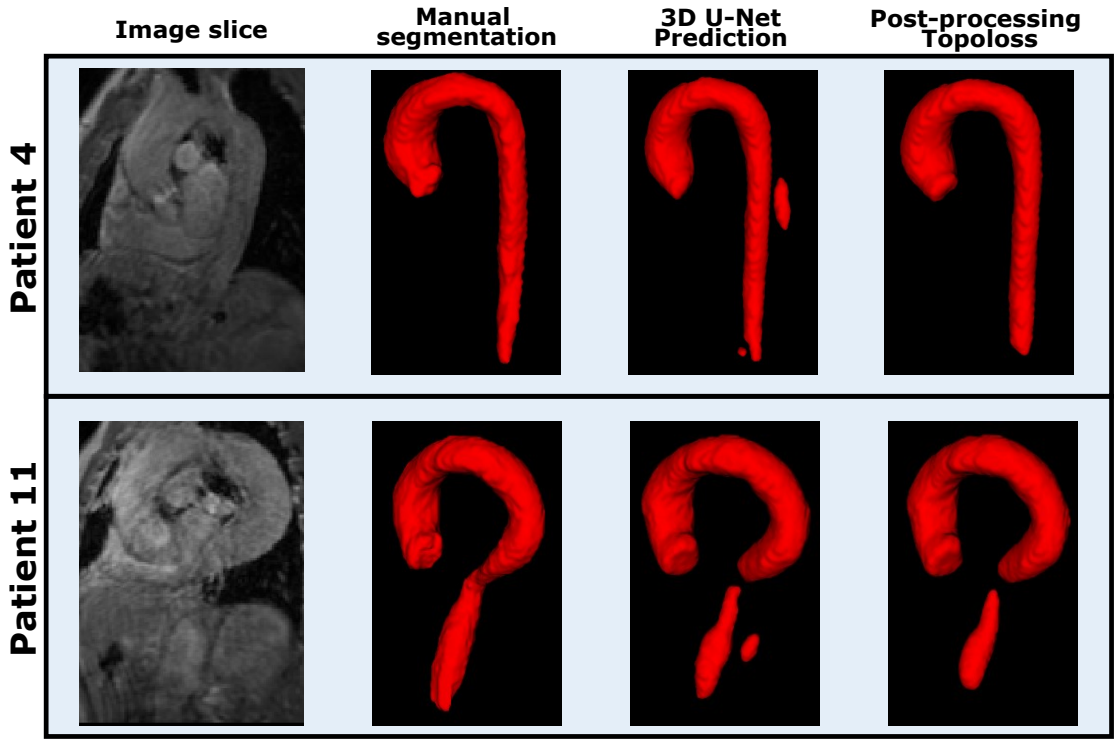

Figure A.6: Results of manual segmentation compared with automatic segmentation with and without post-processing using topoloss

Improving the future computation time could allow us to extensively evaluate this approach on 3D images.

A.2/ AFFINE AND B-SPLINE HYPER-PARAMETERS SEARCH

Table A.4: Average performance of each set of parameters tested for the affine transformation

Pyramid	Resolutions	Metric	Bins	mean HD	std HD	mean DSC	std DSC
SmoothingImagePyramid	1	AdvancedMattesMutualInformation	16	73.54	26.39	65.63	9.51
SmoothingImagePyramid	1	AdvancedMattesMutualInformation	32	74.33	25.36	63.76	10.23
SmoothingImagePyramid	1	AdvancedMattesMutualInformation	64	83.78	25.52	60.05	10.00
SmoothingImagePyramid	1	NormalizedMutualInformation	16	76.15	25.99	65.63	9.39
SmoothingImagePyramid	1	NormalizedMutualInformation	32	74.11	24.29	63.76	10.24
SmoothingImagePyramid	1	NormalizedMutualInformation	64	82.34	25.65	60.13	9.83
SmoothingImagePyramid	1	AdvancedNormalizedCorrelation	32	86.70	28.57	68.24	7.41
SmoothingImagePyramid	1	AdvancedMeanSquares	32	103.03	32.09	63.35	9.83
SmoothingImagePyramid	2	AdvancedMattesMutualInformation	16	64.24	26.52	69.64	8.14
SmoothingImagePyramid	2	AdvancedMattesMutualInformation	32	62.22	26.62	69.23	8.45
SmoothingImagePyramid	2	AdvancedMattesMutualInformation	64	65.72	23.52	67.00	9.14
SmoothingImagePyramid	2	NormalizedMutualInformation	16	64.82	26.34	69.67	8.08
SmoothingImagePyramid	2	NormalizedMutualInformation	32	62.90	26.62	69.23	8.43
SmoothingImagePyramid	2	NormalizedMutualInformation	64	67.82	23.78	66.84	9.08
SmoothingImagePyramid	2	AdvancedNormalizedCorrelation	32	79.68	26.77	70.27	7.01
SmoothingImagePyramid	2	AdvancedMeanSquares	32	104.22	28.79	65.77	9.35
SmoothingImagePyramid	3	AdvancedMattesMutualInformation	16	64.36	26.27	70.49	7.77
SmoothingImagePyramid	3	AdvancedMattesMutualInformation	32	60.36	25.33	70.63	7.97
SmoothingImagePyramid	3	AdvancedMattesMutualInformation	64	60.34	27.02	69.96	8.10
SmoothingImagePyramid	3	NormalizedMutualInformation	16	64.54	26.46	70.61	7.78
SmoothingImagePyramid	3	NormalizedMutualInformation	32	59.90	24.41	70.69	7.96
SmoothingImagePyramid	3	NormalizedMutualInformation	64	63.01	27.56	69.95	7.99
SmoothingImagePyramid	3	AdvancedNormalizedCorrelation	32	76.92	25.66	70.81	7.07
SmoothingImagePyramid	3	AdvancedMeanSquares	32	105.76	27.96	66.04	10.18
SmoothingImagePyramid	4	AdvancedMattesMutualInformation	16	62.23	26.66	70.70	7.76
SmoothingImagePyramid	4	AdvancedMattesMutualInformation	32	58.96	24.04	70.93	7.73
SmoothingImagePyramid	4	AdvancedMattesMutualInformation	64	60.96	23.39	70.53	7.81
SmoothingImagePyramid	4	NormalizedMutualInformation	16	62.34	26.37	70.72	7.76
SmoothingImagePyramid	4	NormalizedMutualInformation	32	61.68	25.16	70.85	7.78
SmoothingImagePyramid	4	NormalizedMutualInformation	64	61.85	26.78	70.51	7.93
SmoothingImagePyramid	4	AdvancedNormalizedCorrelation	32	77.80	25.54	70.78	6.97
SmoothingImagePyramid	4	AdvancedMeanSquares	32	121.08	29.44	63.23	14.26
RecursiveImagePyramid	1	AdvancedMattesMutualInformation	16	76.21	27.60	64.82	9.85
RecursiveImagePyramid	1	AdvancedMattesMutualInformation	32	79.25	24.46	62.20	10.10
RecursiveImagePyramid	1	AdvancedMattesMutualInformation	64	87.26	26.23	58.68	9.49
RecursiveImagePyramid	1	NormalizedMutualInformation	16	78.22	27.79	64.66	9.82
RecursiveImagePyramid	1	NormalizedMutualInformation	32	78.94	24.07	62.16	10.04
RecursiveImagePyramid	1	NormalizedMutualInformation	64	90.29	27.18	58.69	9.36
RecursiveImagePyramid	1	AdvancedNormalizedCorrelation	32	88.58	28.11	67.28	7.60
RecursiveImagePyramid	1	AdvancedMeanSquares	32	104.61	33.82	61.55	10.76
RecursiveImagePyramid	2	AdvancedMattesMutualInformation	16	61.28	24.49	70.55	7.88
RecursiveImagePyramid	2	AdvancedMattesMutualInformation	32	60.37	26.52	70.60	7.90
RecursiveImagePyramid	2	AdvancedMattesMutualInformation	64	62.22	26.85	69.79	8.08
RecursiveImagePyramid	2	NormalizedMutualInformation	16	62.98	24.81	70.45	7.78
RecursiveImagePyramid	2	NormalizedMutualInformation	32	59.25	25.91	70.53	7.87
RecursiveImagePyramid	2	NormalizedMutualInformation	64	60.32	27.64	69.73	8.16
RecursiveImagePyramid	2	AdvancedNormalizedCorrelation	32	78.01	27.80	70.78	7.02
RecursiveImagePyramid	2	AdvancedMeanSquares	32	107.47	28.35	66.00	10.41
RecursiveImagePyramid	3	AdvancedMattesMutualInformation	16	58.86	24.51	71.18	7.54
RecursiveImagePyramid	3	AdvancedMattesMutualInformation	32	57.59	24.64	71.24	7.67
RecursiveImagePyramid	**3**	**AdvancedMattesMutualInformation**	**64**	**55.76**	**25.18**	**71.07**	**7.91**
RecursiveImagePyramid	3	NormalizedMutualInformation	16	59.02	24.36	71.18	7.63
RecursiveImagePyramid	3	NormalizedMutualInformation	32	58.04	25.03	71.18	7.65
RecursiveImagePyramid	3	NormalizedMutualInformation	64	57.50	24.41	70.93	7.81
RecursiveImagePyramid	3	AdvancedNormalizedCorrelation	32	75.43	25.92	71.18	6.72
RecursiveImagePyramid	3	AdvancedMeanSquares	32	114.63	28.90	65.01	12.66
RecursiveImagePyramid	4	AdvancedMattesMutualInformation	16	63.21	27.09	71.26	7.41
RecursiveImagePyramid	4	AdvancedMattesMutualInformation	32	58.49	24.73	71.33	7.48
RecursiveImagePyramid	4	AdvancedMattesMutualInformation	64	57.96	26.22	70.95	7.94
RecursiveImagePyramid	4	NormalizedMutualInformation	16	63.74	26.73	71.20	7.39
RecursiveImagePyramid	4	NormalizedMutualInformation	32	63.01	26.84	71.06	7.66
RecursiveImagePyramid	4	NormalizedMutualInformation	64	60.83	28.58	70.77	8.03
RecursiveImagePyramid	4	AdvancedNormalizedCorrelation	32	80.44	29.53	71.01	7.07
RecursiveImagePyramid	4	AdvancedMeanSquares	32	131.16	27.43	59.49	17.49

Table A.5: Average performance of each set of parameters tested for the B-spline transformation

Pyramid	Resolutions	Metric	Bins	Spacing	mean HD	std HD	mean DSC	std DSC
RecursiveImagePyramid	3	AdvancedNormalizedCorrelation	32	(10.0, 10.0, 10.0)	46.83	29.61	85.53	3.94
RecursiveImagePyramid	3	AdvancedNormalizedCorrelation	32	(10.0, 10.0, 16.0)	49.76	29.79	85.12	3.63
RecursiveImagePyramid	3	AdvancedNormalizedCorrelation	32	(10.0, 10.0, 22.0)	50.56	29.74	84.58	3.6
RecursiveImagePyramid	3	AdvancedNormalizedCorrelation	32	(10.0, 10.0, 28.0)	51.21	29.74	84.22	3.62
RecursiveImagePyramid	3	AdvancedNormalizedCorrelation	32	(10.0, 10.0, 34.0)	53.26	30.41	83.88	3.72
RecursiveImagePyramid	3	AdvancedNormalizedCorrelation	32	(10.0, 10.0, 40.0)	53.69	30.75	83.64	3.76
RecursiveImagePyramid	3	AdvancedNormalizedCorrelation	32	(10.0, 10.0, 46.0)	54	30.68	83.37	3.84
RecursiveImagePyramid	3	AdvancedNormalizedCorrelation	32	(10.0, 16.0, 10.0)	42.36	30.18	85.93	3.89
RecursiveImagePyramid	3	AdvancedNormalizedCorrelation	32	(10.0, 16.0, 16.0)	44.34	29.85	85.54	3.63
RecursiveImagePyramid	3	AdvancedNormalizedCorrelation	32	(10.0, 16.0, 22.0)	45.43	29.75	84.96	3.61
RecursiveImagePyramid	3	AdvancedNormalizedCorrelation	32	(10.0, 16.0, 28.0)	47.74	30.92	84.5	3.63
RecursiveImagePyramid	3	AdvancedNormalizedCorrelation	32	(10.0, 16.0, 34.0)	48.96	30.86	84.27	3.67
RecursiveImagePyramid	3	AdvancedNormalizedCorrelation	32	(10.0, 16.0, 40.0)	49.63	30.85	84.06	3.76
RecursiveImagePyramid	3	AdvancedNormalizedCorrelation	32	(10.0, 16.0, 46.0)	50.07	30.97	83.82	3.81
RecursiveImagePyramid	3	AdvancedNormalizedCorrelation	32	(10.0, 22.0, 10.0)	41.71	29.25	86.1	3.91
RecursiveImagePyramid	3	AdvancedNormalizedCorrelation	32	(10.0, 22.0, 16.0)	43.93	28.92	85.66	3.62
RecursiveImagePyramid	3	AdvancedNormalizedCorrelation	32	(10.0, 22.0, 22.0)	46.65	29.16	85.04	3.58
RecursiveImagePyramid	3	AdvancedNormalizedCorrelation	32	(10.0, 22.0, 28.0)	47.86	29.14	84.62	3.57
RecursiveImagePyramid	3	AdvancedNormalizedCorrelation	32	(10.0, 22.0, 34.0)	49.69	29.51	84.29	3.67
RecursiveImagePyramid	3	AdvancedNormalizedCorrelation	32	(10.0, 22.0, 40.0)	50.73	30.04	84.06	3.8
RecursiveImagePyramid	3	AdvancedNormalizedCorrelation	32	(10.0, 22.0, 46.0)	50.69	30.08	83.89	3.88
RecursiveImagePyramid	3	AdvancedNormalizedCorrelation	32	(10.0, 28.0, 10.0)	44.39	29.1	85.83	3.74
RecursiveImagePyramid	3	AdvancedNormalizedCorrelation	32	(10.0, 28.0, 16.0)	46.58	29.16	85.35	3.5
RecursiveImagePyramid	3	AdvancedNormalizedCorrelation	32	(10.0, 28.0, 22.0)	47.59	29.14	84.86	3.52
RecursiveImagePyramid	3	AdvancedNormalizedCorrelation	32	(10.0, 28.0, 28.0)	49.77	28.95	84.41	3.61
RecursiveImagePyramid	3	AdvancedNormalizedCorrelation	32	(10.0, 28.0, 34.0)	53.09	32.1	84.07	3.84
RecursiveImagePyramid	3	AdvancedNormalizedCorrelation	32	(10.0, 28.0, 40.0)	52.93	32.79	83.87	3.85
RecursiveImagePyramid	3	AdvancedNormalizedCorrelation	32	(10.0, 28.0, 46.0)	53.52	33.47	83.7	3.91
RecursiveImagePyramid	3	AdvancedNormalizedCorrelation	32	(10.0, 34.0, 10.0)	42.91	29.57	85.7	3.57
RecursiveImagePyramid	3	AdvancedNormalizedCorrelation	32	(10.0, 34.0, 16.0)	44.58	28.9	85.25	3.42
RecursiveImagePyramid	3	AdvancedNormalizedCorrelation	32	(10.0, 34.0, 22.0)	47.27	30.31	84.76	3.49
RecursiveImagePyramid	3	AdvancedNormalizedCorrelation	32	(10.0, 34.0, 28.0)	49.14	30.43	84.3	3.69
RecursiveImagePyramid	3	AdvancedNormalizedCorrelation	32	(10.0, 34.0, 34.0)	51.9	33.42	83.94	3.85
RecursiveImagePyramid	3	AdvancedNormalizedCorrelation	32	(10.0, 34.0, 40.0)	49.71	30.02	83.78	3.83
RecursiveImagePyramid	3	AdvancedNormalizedCorrelation	32	(10.0, 34.0, 46.0)	55.48	33.95	83.45	3.96
RecursiveImagePyramid	3	AdvancedNormalizedCorrelation	32	(10.0, 40.0, 10.0)	44.29	29.75	85.27	3.56
RecursiveImagePyramid	3	AdvancedNormalizedCorrelation	32	(10.0, 40.0, 16.0)	46.55	28.25	84.89	3.36
RecursiveImagePyramid	3	AdvancedNormalizedCorrelation	32	(10.0, 40.0, 22.0)	49.02	29.01	84.35	3.61
RecursiveImagePyramid	3	AdvancedNormalizedCorrelation	32	(10.0, 40.0, 28.0)	51.85	28.27	83.91	3.76
RecursiveImagePyramid	3	AdvancedNormalizedCorrelation	32	(10.0, 40.0, 34.0)	55.17	31.59	83.59	3.98
RecursiveImagePyramid	3	AdvancedNormalizedCorrelation	32	(10.0, 40.0, 40.0)	55.4	30.81	83.4	4.06
RecursiveImagePyramid	3	AdvancedNormalizedCorrelation	32	(10.0, 40.0, 46.0)	56.12	32.07	83.1	4.21
RecursiveImagePyramid	3	AdvancedNormalizedCorrelation	32	(10.0, 46.0, 10.0)	46.9	30.48	84.78	3.63
RecursiveImagePyramid	3	AdvancedNormalizedCorrelation	32	(10.0, 46.0, 16.0)	49.47	29.94	84.42	3.48
RecursiveImagePyramid	3	AdvancedNormalizedCorrelation	32	(10.0, 46.0, 22.0)	52.12	29.4	84	3.69
RecursiveImagePyramid	3	AdvancedNormalizedCorrelation	32	(10.0, 46.0, 28.0)	55.54	31.89	83.61	3.88
RecursiveImagePyramid	3	AdvancedNormalizedCorrelation	32	(10.0, 46.0, 34.0)	57.55	31.68	83.29	3.88
RecursiveImagePyramid	3	AdvancedNormalizedCorrelation	32	(10.0, 46.0, 40.0)	57.38	33.09	83.13	3.89
RecursiveImagePyramid	3	AdvancedNormalizedCorrelation	32	(10.0, 46.0, 46.0)	57.54	32.86	82.89	4.04
RecursiveImagePyramid	3	AdvancedNormalizedCorrelation	32	(16.0, 10.0, 10.0)	47.27	26.81	85.71	3.44
RecursiveImagePyramid	3	AdvancedNormalizedCorrelation	32	(16.0, 10.0, 16.0)	48.51	26.26	85.46	3.23
RecursiveImagePyramid	3	AdvancedNormalizedCorrelation	32	(16.0, 10.0, 22.0)	50.04	27.57	84.95	3.16
RecursiveImagePyramid	3	AdvancedNormalizedCorrelation	32	(16.0, 10.0, 28.0)	51.72	27.87	84.5	3.24
RecursiveImagePyramid	3	AdvancedNormalizedCorrelation	32	(16.0, 10.0, 34.0)	51.95	28.14	84.24	3.29
RecursiveImagePyramid	3	AdvancedNormalizedCorrelation	32	(16.0, 10.0, 40.0)	52.11	28.04	84	3.42
RecursiveImagePyramid	3	AdvancedNormalizedCorrelation	32	(16.0, 10.0, 46.0)	52.35	27.33	83.77	3.49
RecursiveImagePyramid	3	AdvancedNormalizedCorrelation	32	(16.0, 16.0, 10.0)	40.74	26.43	86.22	3.48
RecursiveImagePyramid	3	AdvancedNormalizedCorrelation	32	(16.0, 16.0, 16.0)	43.32	26.68	85.95	3.3
RecursiveImagePyramid	3	AdvancedNormalizedCorrelation	32	(16.0, 16.0, 22.0)	44.62	26.25	85.48	3.36
RecursiveImagePyramid	3	AdvancedNormalizedCorrelation	32	(16.0, 16.0, 28.0)	46.49	26.41	85.06	3.41
RecursiveImagePyramid	3	AdvancedNormalizedCorrelation	32	(16.0, 16.0, 34.0)	47.5	26.81	84.75	3.46
RecursiveImagePyramid	3	AdvancedNormalizedCorrelation	32	(16.0, 16.0, 40.0)	47.63	27.01	84.53	3.51
RecursiveImagePyramid	3	AdvancedNormalizedCorrelation	32	(16.0, 16.0, 46.0)	48.26	27.09	84.25	3.71
RecursiveImagePyramid	3	AdvancedNormalizedCorrelation	32	(16.0, 22.0, 10.0)	39.77	26.3	86.39	3.48
RecursiveImagePyramid	3	AdvancedNormalizedCorrelation	32	(16.0, 22.0, 16.0)	41.49	26.38	86.06	3.34
RecursiveImagePyramid	3	AdvancedNormalizedCorrelation	32	(16.0, 22.0, 22.0)	43.74	27.28	85.62	3.36
RecursiveImagePyramid	3	AdvancedNormalizedCorrelation	32	(16.0, 22.0, 28.0)	44.45	27.09	85.11	3.48
RecursiveImagePyramid	3	AdvancedNormalizedCorrelation	32	(16.0, 22.0, 34.0)	45.11	27.3	84.89	3.42
RecursiveImagePyramid	3	AdvancedNormalizedCorrelation	32	(16.0, 22.0, 40.0)	46.41	27.18	84.63	3.56
RecursiveImagePyramid	3	AdvancedNormalizedCorrelation	32	(16.0, 22.0, 46.0)	47.07	27.11	84.38	3.71

Table A.6: Average performance of each set of parameters tested for the B-spline transformation

Pyramid	Resolutions	Metric	Bins	Spacing	mean HD	std HD	mean DSC	std DSC
RecursiveImagePyramid	3	AdvancedNormalizedCorrelation	32	(16.0, 28.0, 10.0)	40.16	26.09	86.17	3.43
RecursiveImagePyramid	3	AdvancedNormalizedCorrelation	32	(16.0, 28.0, 16.0)	41.53	24.75	85.93	3.25
RecursiveImagePyramid	3	AdvancedNormalizedCorrelation	32	(16.0, 28.0, 22.0)	43.81	26.95	85.46	3.24
RecursiveImagePyramid	3	AdvancedNormalizedCorrelation	32	(16.0, 28.0, 28.0)	44.96	26.42	85.05	3.36
RecursiveImagePyramid	3	AdvancedNormalizedCorrelation	32	(16.0, 28.0, 34.0)	46.01	26.14	84.77	3.48
RecursiveImagePyramid	3	AdvancedNormalizedCorrelation	32	(16.0, 28.0, 40.0)	47.82	26.49	84.52	3.63
RecursiveImagePyramid	3	AdvancedNormalizedCorrelation	32	(16.0, 28.0, 46.0)	47.62	26.66	84.21	3.77
RecursiveImagePyramid	3	AdvancedNormalizedCorrelation	32	(16.0, 34.0, 10.0)	39.49	27.43	86.06	3.3
RecursiveImagePyramid	3	AdvancedNormalizedCorrelation	32	(16.0, 34.0, 16.0)	41.5	25.97	85.74	3.22
RecursiveImagePyramid	3	AdvancedNormalizedCorrelation	32	(16.0, 34.0, 22.0)	43.59	27.88	85.19	3.39
RecursiveImagePyramid	3	AdvancedNormalizedCorrelation	32	(16.0, 34.0, 28.0)	45.11	27.49	84.76	3.6
RecursiveImagePyramid	3	AdvancedNormalizedCorrelation	32	(16.0, 34.0, 34.0)	48.26	30.35	84.51	3.77
RecursiveImagePyramid	3	AdvancedNormalizedCorrelation	32	(16.0, 34.0, 40.0)	49.43	30.67	84.32	3.73
RecursiveImagePyramid	3	AdvancedNormalizedCorrelation	32	(16.0, 34.0, 46.0)	50.43	31.59	84.04	3.93
RecursiveImagePyramid	3	AdvancedNormalizedCorrelation	32	(16.0, 40.0, 10.0)	40.47	27.71	85.7	3.4
RecursiveImagePyramid	3	AdvancedNormalizedCorrelation	32	(16.0, 40.0, 16.0)	42.12	26.2	85.46	3.36
RecursiveImagePyramid	3	AdvancedNormalizedCorrelation	32	(16.0, 40.0, 22.0)	43.86	26.63	84.95	3.44
RecursiveImagePyramid	3	AdvancedNormalizedCorrelation	32	(16.0, 40.0, 28.0)	45.54	27.59	84.53	3.53
RecursiveImagePyramid	3	AdvancedNormalizedCorrelation	32	(16.0, 40.0, 34.0)	46.72	27.33	84.2	3.67
RecursiveImagePyramid	3	AdvancedNormalizedCorrelation	32	(16.0, 40.0, 40.0)	49.72	31.5	83.97	3.78
RecursiveImagePyramid	3	AdvancedNormalizedCorrelation	32	(16.0, 40.0, 46.0)	50.58	31.11	83.68	3.89
RecursiveImagePyramid	3	AdvancedNormalizedCorrelation	32	(16.0, 46.0, 10.0)	43.03	28.24	85.28	3.34
RecursiveImagePyramid	3	AdvancedNormalizedCorrelation	32	(16.0, 46.0, 16.0)	45.1	25.98	85.06	3.16
RecursiveImagePyramid	3	AdvancedNormalizedCorrelation	32	(16.0, 46.0, 22.0)	47.32	27.27	84.6	3.46
RecursiveImagePyramid	3	AdvancedNormalizedCorrelation	32	(16.0, 46.0, 28.0)	51.17	30.95	84.15	3.56
RecursiveImagePyramid	3	AdvancedNormalizedCorrelation	32	(16.0, 46.0, 34.0)	52.4	30.78	83.86	3.62
RecursiveImagePyramid	3	AdvancedNormalizedCorrelation	32	(16.0, 46.0, 40.0)	53.55	31.13	83.66	3.73
RecursiveImagePyramid	3	AdvancedNormalizedCorrelation	32	(16.0, 46.0, 46.0)	53.73	30.72	83.43	3.86
RecursiveImagePyramid	3	AdvancedNormalizedCorrelation	32	(22.0, 10.0, 10.0)	47.4	22.79	85.71	3.24
RecursiveImagePyramid	3	AdvancedNormalizedCorrelation	32	(22.0, 10.0, 16.0)	47.95	22.93	85.58	3.01
RecursiveImagePyramid	3	AdvancedNormalizedCorrelation	32	(22.0, 10.0, 22.0)	49.25	22.59	85.13	2.91
RecursiveImagePyramid	3	AdvancedNormalizedCorrelation	32	(22.0, 10.0, 28.0)	49.75	22.84	84.74	2.95
RecursiveImagePyramid	3	AdvancedNormalizedCorrelation	32	(22.0, 10.0, 34.0)	51.05	22.94	84.4	3.06
RecursiveImagePyramid	3	AdvancedNormalizedCorrelation	32	(22.0, 10.0, 40.0)	51.9	22.73	84.22	3.11
RecursiveImagePyramid	3	AdvancedNormalizedCorrelation	32	(22.0, 10.0, 46.0)	51.62	22.83	84.01	3.08
RecursiveImagePyramid	3	AdvancedNormalizedCorrelation	32	(22.0, 16.0, 10.0)	39.43	23.22	86.28	3.15
RecursiveImagePyramid	3	AdvancedNormalizedCorrelation	32	(22.0, 16.0, 16.0)	43.62	23.68	85.49	3.26
RecursiveImagePyramid	3	AdvancedNormalizedCorrelation	32	(22.0, 16.0, 22.0)	43.6	22.77	85.59	3.05
RecursiveImagePyramid	3	AdvancedNormalizedCorrelation	32	(22.0, 16.0, 28.0)	43.39	23.31	85.09	3.22
RecursiveImagePyramid	3	AdvancedNormalizedCorrelation	32	(22.0, 16.0, 34.0)	45.23	23.58	85	3.06
RecursiveImagePyramid	3	AdvancedNormalizedCorrelation	32	(22.0, 16.0, 40.0)	45.55	22.49	84.81	3.11
RecursiveImagePyramid	3	AdvancedNormalizedCorrelation	32	(22.0, 16.0, 46.0)	46.66	23.14	84.48	3.24
RecursiveImagePyramid	3	AdvancedNormalizedCorrelation	32	(22.0, 22.0, 10.0)	39.56	27.43	86.03	3.49
RecursiveImagePyramid	3	AdvancedNormalizedCorrelation	32	(22.0, 22.0, 16.0)	39.89	25.07	86	3.37
RecursiveImagePyramid	3	AdvancedNormalizedCorrelation	32	(22.0, 22.0, 22.0)	41.96	25.28	85.49	3.03
RecursiveImagePyramid	3	AdvancedNormalizedCorrelation	32	(22.0, 22.0, 28.0)	44.16	25.33	85.38	3.14
RecursiveImagePyramid	3	AdvancedNormalizedCorrelation	32	(22.0, 22.0, 34.0)	45.15	25.02	85.06	3.24
RecursiveImagePyramid	3	AdvancedNormalizedCorrelation	32	(22.0, 22.0, 40.0)	43.77	23.82	85.3	2.46
RecursiveImagePyramid	3	AdvancedNormalizedCorrelation	32	(22.0, 22.0, 46.0)	46.09	25.54	84.55	3.43
RecursiveImagePyramid	3	AdvancedNormalizedCorrelation	32	(22.0, 28.0, 10.0)	37.74	22.95	86.07	2.97
RecursiveImagePyramid	3	AdvancedNormalizedCorrelation	32	(22.0, 28.0, 16.0)	40.57	24.66	86.1	2.6
RecursiveImagePyramid	3	AdvancedNormalizedCorrelation	32	(22.0, 28.0, 22.0)	41.78	23.64	85.47	3.15
RecursiveImagePyramid	3	AdvancedNormalizedCorrelation	32	(22.0, 28.0, 28.0)	43.27	23.17	85.23	3.02
RecursiveImagePyramid	3	AdvancedNormalizedCorrelation	32	(22.0, 28.0, 34.0)	43.79	24.35	84.87	3.39
RecursiveImagePyramid	3	AdvancedNormalizedCorrelation	32	(22.0, 28.0, 40.0)	44.91	24.27	84.73	3.34
RecursiveImagePyramid	3	AdvancedNormalizedCorrelation	32	(22.0, 28.0, 46.0)	44.26	24.65	84.64	3.43
RecursiveImagePyramid	3	AdvancedNormalizedCorrelation	32	(22.0, 34.0, 10.0)	37.55	23.61	85.87	3.25
RecursiveImagePyramid	3	AdvancedNormalizedCorrelation	32	(22.0, 34.0, 16.0)	39.48	23.95	85.77	3.11
RecursiveImagePyramid	3	AdvancedNormalizedCorrelation	32	(22.0, 34.0, 22.0)	40.85	27.66	85.18	3.31
RecursiveImagePyramid	3	AdvancedNormalizedCorrelation	32	(22.0, 34.0, 28.0)	42.84	26.67	84.93	3.42
RecursiveImagePyramid	3	AdvancedNormalizedCorrelation	32	(22.0, 34.0, 34.0)	42.22	25.36	84.99	3.16
RecursiveImagePyramid	3	AdvancedNormalizedCorrelation	32	(22.0, 34.0, 40.0)	43.41	24.82	84.63	3.62
RecursiveImagePyramid	3	AdvancedNormalizedCorrelation	32	(22.0, 34.0, 46.0)	45.17	27.65	84.49	3.74
RecursiveImagePyramid	**3**	**AdvancedNormalizedCorrelation**	**32**	**(22.0, 40.0, 10.0)**	**36.26**	**23.16**	**85.79**	**3.27**
RecursiveImagePyramid	3	AdvancedNormalizedCorrelation	32	(22.0, 40.0, 16.0)	38.65	23.31	85.59	3.21
RecursiveImagePyramid	3	AdvancedNormalizedCorrelation	32	(22.0, 40.0, 22.0)	40.66	24.09	85.2	3.25
RecursiveImagePyramid	3	AdvancedNormalizedCorrelation	32	(22.0, 40.0, 28.0)	40.52	23.42	85.15	2.87
RecursiveImagePyramid	3	AdvancedNormalizedCorrelation	32	(22.0, 40.0, 34.0)	44.08	23.12	84.3	3.34
RecursiveImagePyramid	3	AdvancedNormalizedCorrelation	32	(22.0, 40.0, 40.0)	44.59	25.55	84.3	3.6
RecursiveImagePyramid	3	AdvancedNormalizedCorrelation	32	(22.0, 40.0, 46.0)	44.5	24.51	84.19	3.6

Table A.7: Average performance of each set of parameters tested for the B-spline transformation

Pyramid	Resolutions	Metric	Bins	Spacing	mean HD	std HD	mean DSC	std DSC
RecursiveImagePyramid	3	AdvancedNormalizedCorrelation	32	(22.0, 46.0, 10.0)	40.94	25.02	85.32	3.4
RecursiveImagePyramid	3	AdvancedNormalizedCorrelation	32	(22.0, 46.0, 16.0)	40.5	24.66	85.06	3.26
RecursiveImagePyramid	3	AdvancedNormalizedCorrelation	32	(22.0, 46.0, 22.0)	43.39	26.31	84.83	3.21
RecursiveImagePyramid	3	AdvancedNormalizedCorrelation	32	(22.0, 46.0, 28.0)	45.44	25.96	84.55	3.07
RecursiveImagePyramid	3	AdvancedNormalizedCorrelation	32	(22.0, 46.0, 34.0)	47.29	26.93	84.48	3.29
RecursiveImagePyramid	3	AdvancedNormalizedCorrelation	32	(22.0, 46.0, 40.0)	49.78	29.24	83.89	3.55
RecursiveImagePyramid	3	AdvancedNormalizedCorrelation	32	(22.0, 46.0, 46.0)	46.44	29.64	84	3.72
RecursiveImagePyramid	3	AdvancedNormalizedCorrelation	32	(28.0, 10.0, 10.0)	47.5	23.01	85.52	2.62
RecursiveImagePyramid	3	AdvancedNormalizedCorrelation	32	(28.0, 10.0, 16.0)	48.28	21.71	85.39	2.73
RecursiveImagePyramid	3	AdvancedNormalizedCorrelation	32	(28.0, 10.0, 22.0)	48.25	23.35	84.86	2.86
RecursiveImagePyramid	3	AdvancedNormalizedCorrelation	32	(28.0, 10.0, 28.0)	48.31	22.13	84.73	2.72
RecursiveImagePyramid	3	AdvancedNormalizedCorrelation	32	(28.0, 10.0, 34.0)	48.67	21.64	84.55	2.81
RecursiveImagePyramid	3	AdvancedNormalizedCorrelation	32	(28.0, 10.0, 40.0)	49.74	22.09	84.28	2.73
RecursiveImagePyramid	3	AdvancedNormalizedCorrelation	32	(28.0, 10.0, 46.0)	50.51	22.61	84.09	2.79
RecursiveImagePyramid	3	AdvancedNormalizedCorrelation	32	(28.0, 16.0, 10.0)	40.89	22.25	86	2.93
RecursiveImagePyramid	3	AdvancedNormalizedCorrelation	32	(28.0, 16.0, 16.0)	41.78	22.36	85.77	2.72
RecursiveImagePyramid	3	AdvancedNormalizedCorrelation	32	(28.0, 16.0, 22.0)	43.23	22.71	85.87	2.27
RecursiveImagePyramid	3	AdvancedNormalizedCorrelation	32	(28.0, 16.0, 28.0)	44.03	23.34	85.16	2.88
RecursiveImagePyramid	3	AdvancedNormalizedCorrelation	32	(28.0, 16.0, 34.0)	43.92	23.88	84.9	3.13
RecursiveImagePyramid	3	AdvancedNormalizedCorrelation	32	(28.0, 16.0, 40.0)	44.22	23.31	84.69	3.11
RecursiveImagePyramid	3	AdvancedNormalizedCorrelation	32	(28.0, 16.0, 46.0)	44.46	23.56	84.43	3.21
RecursiveImagePyramid	3	AdvancedNormalizedCorrelation	32	(28.0, 22.0, 10.0)	39.84	22.25	85.89	2.97
RecursiveImagePyramid	3	AdvancedNormalizedCorrelation	32	(28.0, 22.0, 16.0)	40.58	23.12	85.74	3
RecursiveImagePyramid	3	AdvancedNormalizedCorrelation	32	(28.0, 22.0, 22.0)	39.78	23.68	85.58	2.88
RecursiveImagePyramid	3	AdvancedNormalizedCorrelation	32	(28.0, 22.0, 28.0)	41.96	24.65	85.33	2.99
RecursiveImagePyramid	3	AdvancedNormalizedCorrelation	32	(28.0, 22.0, 34.0)	42.29	24.56	85.16	2.95
RecursiveImagePyramid	3	AdvancedNormalizedCorrelation	32	(28.0, 22.0, 40.0)	42.58	25.65	84.91	3.05
RecursiveImagePyramid	3	AdvancedNormalizedCorrelation	32	(28.0, 22.0, 46.0)	43.38	25.38	84.71	3.09
RecursiveImagePyramid	3	AdvancedNormalizedCorrelation	32	(28.0, 28.0, 10.0)	37.44	22.64	85.76	3.1
RecursiveImagePyramid	3	AdvancedNormalizedCorrelation	32	(28.0, 28.0, 16.0)	38.03	23.55	85.88	2.87
RecursiveImagePyramid	3	AdvancedNormalizedCorrelation	32	(28.0, 28.0, 22.0)	39.67	23.48	85.42	3.04
RecursiveImagePyramid	3	AdvancedNormalizedCorrelation	32	(28.0, 28.0, 28.0)	41.44	22.5	85.27	2.94
RecursiveImagePyramid	3	AdvancedNormalizedCorrelation	32	(28.0, 28.0, 34.0)	44.16	27.35	85.04	3.45
RecursiveImagePyramid	3	AdvancedNormalizedCorrelation	32	(28.0, 28.0, 40.0)	44.16	27.35	85.04	3.45
RecursiveImagePyramid	3	AdvancedNormalizedCorrelation	32	(28.0, 28.0, 46.0)	44.16	27.35	85.04	3.45
RecursiveImagePyramid	3	AdvancedNormalizedCorrelation	32	(28.0, 34.0, 10.0)	44.16	27.35	85.04	3.45
RecursiveImagePyramid	3	AdvancedNormalizedCorrelation	32	(28.0, 34.0, 16.0)	44.16	27.35	85.04	3.45
RecursiveImagePyramid	3	AdvancedNormalizedCorrelation	32	(28.0, 34.0, 22.0)	44.16	27.35	85.04	3.45
RecursiveImagePyramid	3	AdvancedNormalizedCorrelation	32	(28.0, 34.0, 28.0)	44.16	27.35	85.04	3.45
RecursiveImagePyramid	3	AdvancedNormalizedCorrelation	32	(28.0, 34.0, 34.0)	44.16	27.35	85.04	3.45
RecursiveImagePyramid	3	AdvancedNormalizedCorrelation	32	(28.0, 34.0, 40.0)	44.16	27.35	85.04	3.45
RecursiveImagePyramid	3	AdvancedNormalizedCorrelation	32	(28.0, 34.0, 46.0)	44.16	27.35	85.04	3.45
RecursiveImagePyramid	3	AdvancedNormalizedCorrelation	32	(28.0, 40.0, 10.0)	44.16	27.35	85.04	3.45
RecursiveImagePyramid	3	AdvancedNormalizedCorrelation	32	(28.0, 40.0, 16.0)	44.16	27.35	85.04	3.45
RecursiveImagePyramid	3	AdvancedNormalizedCorrelation	32	(28.0, 40.0, 22.0)	44.16	27.35	85.04	3.45
RecursiveImagePyramid	3	AdvancedNormalizedCorrelation	32	(28.0, 40.0, 28.0)	44.16	27.35	85.04	3.45
RecursiveImagePyramid	3	AdvancedNormalizedCorrelation	32	(28.0, 40.0, 34.0)	44.16	27.35	85.04	3.45
RecursiveImagePyramid	3	AdvancedNormalizedCorrelation	32	(28.0, 40.0, 40.0)	44.16	27.35	85.04	3.45
RecursiveImagePyramid	3	AdvancedNormalizedCorrelation	32	(28.0, 40.0, 46.0)	44.16	27.35	85.04	3.45
RecursiveImagePyramid	3	AdvancedNormalizedCorrelation	32	(28.0, 46.0, 10.0)	44.16	27.35	85.04	3.45
RecursiveImagePyramid	3	AdvancedNormalizedCorrelation	32	(28.0, 46.0, 16.0)	44.16	27.35	85.04	3.45
RecursiveImagePyramid	3	AdvancedNormalizedCorrelation	32	(28.0, 46.0, 22.0)	44.16	27.35	85.04	3.45
RecursiveImagePyramid	3	AdvancedNormalizedCorrelation	32	(28.0, 46.0, 28.0)	44.16	27.35	85.04	3.45
RecursiveImagePyramid	3	AdvancedNormalizedCorrelation	32	(28.0, 46.0, 34.0)	44.16	27.35	85.04	3.45
RecursiveImagePyramid	3	AdvancedNormalizedCorrelation	32	(28.0, 46.0, 40.0)	44.08	28.32	85.1	3.19
RecursiveImagePyramid	3	AdvancedNormalizedCorrelation	32	(28.0, 46.0, 46.0)	45.35	28.21	84.93	3.42
RecursiveImagePyramid	3	AdvancedNormalizedCorrelation	32	(34.0, 10.0, 10.0)	45.35	28.21	84.93	3.42
RecursiveImagePyramid	3	AdvancedNormalizedCorrelation	32	(34.0, 10.0, 16.0)	45.35	28.21	84.93	3.42
RecursiveImagePyramid	3	AdvancedNormalizedCorrelation	32	(34.0, 10.0, 22.0)	45.28	27.5	84.86	3.6
RecursiveImagePyramid	3	AdvancedNormalizedCorrelation	32	(34.0, 10.0, 28.0)	46.77	28.54	84.98	3.35
RecursiveImagePyramid	3	AdvancedNormalizedCorrelation	32	(34.0, 10.0, 34.0)	44.44	23.06	85.22	3.1
RecursiveImagePyramid	3	AdvancedNormalizedCorrelation	32	(34.0, 10.0, 40.0)	49.63	30.19	84.7	3.66
RecursiveImagePyramid	3	AdvancedNormalizedCorrelation	32	(34.0, 10.0, 46.0)	47.04	29.98	84.81	3.88
RecursiveImagePyramid	3	AdvancedNormalizedCorrelation	32	(34.0, 16.0, 10.0)	42.55	26.6	85.61	3.05
RecursiveImagePyramid	3	AdvancedNormalizedCorrelation	32	(34.0, 16.0, 16.0)	47.83	29.27	84.88	3.83
RecursiveImagePyramid	3	AdvancedNormalizedCorrelation	32	(34.0, 16.0, 22.0)	44.39	28.29	85.13	3.71
RecursiveImagePyramid	3	AdvancedNormalizedCorrelation	32	(34.0, 16.0, 28.0)	46.74	29.11	84.77	3.78
RecursiveImagePyramid	3	AdvancedNormalizedCorrelation	32	(34.0, 16.0, 34.0)	44.51	28.22	85.27	3.28
RecursiveImagePyramid	3	AdvancedNormalizedCorrelation	32	(34.0, 16.0, 40.0)	46.35	29.32	84.9	3.55
RecursiveImagePyramid	3	AdvancedNormalizedCorrelation	32	(34.0, 16.0, 46.0)	44.95	28.56	85.07	3.22

Table A.8: Average performance of each set of parameters tested for the B-spline transformation

Pyramid	Resolutions	Metric	Bins	Spacing	mean HD	std HD	mean DSC	std DSC
RecursiveImagePyramid	3	AdvancedNormalizedCorrelation	32	(34.0, 22.0, 10.0)	44.72	26.55	85.11	3.52
RecursiveImagePyramid	3	AdvancedNormalizedCorrelation	32	(34.0, 22.0, 16.0)	45.32	27.75	85.04	3.54
RecursiveImagePyramid	3	AdvancedNormalizedCorrelation	32	(34.0, 22.0, 22.0)	46.41	27.52	84.84	3.67
RecursiveImagePyramid	3	AdvancedNormalizedCorrelation	32	(34.0, 22.0, 28.0)	45.11	27.92	84.93	3.72
RecursiveImagePyramid	3	AdvancedNormalizedCorrelation	32	(34.0, 22.0, 34.0)	43.91	26.88	84.89	3.9
RecursiveImagePyramid	3	AdvancedNormalizedCorrelation	32	(34.0, 22.0, 40.0)	43.79	26.23	85.11	3.35
RecursiveImagePyramid	3	AdvancedNormalizedCorrelation	32	(34.0, 22.0, 46.0)	45.27	28.09	84.99	3.14
RecursiveImagePyramid	3	AdvancedNormalizedCorrelation	32	(34.0, 28.0, 10.0)	43.55	27.21	85.11	3.51
RecursiveImagePyramid	3	AdvancedNormalizedCorrelation	32	(34.0, 28.0, 16.0)	44	27.06	85.11	3.41
RecursiveImagePyramid	3	AdvancedNormalizedCorrelation	32	(34.0, 28.0, 22.0)	46.24	29.38	84.89	3.51
RecursiveImagePyramid	3	AdvancedNormalizedCorrelation	32	(34.0, 28.0, 28.0)	43.28	27.48	85.13	3.66
RecursiveImagePyramid	3	AdvancedNormalizedCorrelation	32	(34.0, 28.0, 34.0)	44.35	28.19	84.95	3.42
RecursiveImagePyramid	3	AdvancedNormalizedCorrelation	32	(34.0, 28.0, 40.0)	44.84	27.46	85	3.49
RecursiveImagePyramid	3	AdvancedNormalizedCorrelation	32	(34.0, 28.0, 46.0)	46.28	28.09	84.79	3.56
RecursiveImagePyramid	3	AdvancedNormalizedCorrelation	32	(34.0, 34.0, 10.0)	46.15	28.47	84.85	3.65
RecursiveImagePyramid	3	AdvancedNormalizedCorrelation	32	(34.0, 34.0, 16.0)	44.97	26.92	84.93	3.67
RecursiveImagePyramid	3	AdvancedNormalizedCorrelation	32	(34.0, 34.0, 22.0)	45.73	28.36	84.73	3.86
RecursiveImagePyramid	3	AdvancedNormalizedCorrelation	32	(34.0, 34.0, 28.0)	45.13	28.28	85.01	3.37
RecursiveImagePyramid	3	AdvancedNormalizedCorrelation	32	(34.0, 34.0, 34.0)	44.63	27.92	85.27	3.54
RecursiveImagePyramid	3	AdvancedNormalizedCorrelation	32	(34.0, 34.0, 40.0)	44.01	28.69	85.47	3.31
RecursiveImagePyramid	3	AdvancedNormalizedCorrelation	32	(34.0, 34.0, 46.0)	45.84	27.77	84.91	3.43
RecursiveImagePyramid	3	AdvancedNormalizedCorrelation	32	(34.0, 40.0, 10.0)	49.6	28	84.85	3.82
RecursiveImagePyramid	3	AdvancedNormalizedCorrelation	32	(34.0, 40.0, 16.0)	43.52	26.9	85.36	3.15
RecursiveImagePyramid	3	AdvancedNormalizedCorrelation	32	(34.0, 40.0, 22.0)	43.17	26.27	85.04	3.6
RecursiveImagePyramid	3	AdvancedNormalizedCorrelation	32	(34.0, 40.0, 28.0)	43.17	26.27	85.04	3.6
RecursiveImagePyramid	3	AdvancedNormalizedCorrelation	32	(34.0, 40.0, 34.0)	44.28	27.4	84.87	3.77
RecursiveImagePyramid	3	AdvancedNormalizedCorrelation	32	(34.0, 40.0, 40.0)	43.48	25.77	85.04	3.73
RecursiveImagePyramid	3	AdvancedNormalizedCorrelation	32	(34.0, 40.0, 46.0)	58.81	41.52	83.89	4.52
RecursiveImagePyramid	3	AdvancedNormalizedCorrelation	32	(34.0, 46.0, 10.0)	43.64	30.37	85.23	3.52
RecursiveImagePyramid	3	AdvancedNormalizedCorrelation	32	(34.0, 46.0, 16.0)	38.95	24.64	85.13	3.01
RecursiveImagePyramid	3	AdvancedNormalizedCorrelation	32	(34.0, 46.0, 22.0)	43.37	27.01	85.01	3.64
RecursiveImagePyramid	3	AdvancedNormalizedCorrelation	32	(34.0, 46.0, 28.0)	44.64	28.33	85.14	3.65
RecursiveImagePyramid	3	AdvancedNormalizedCorrelation	32	(34.0, 46.0, 34.0)	44.97	27.06	85.01	3.56
RecursiveImagePyramid	3	AdvancedNormalizedCorrelation	32	(34.0, 46.0, 40.0)	45.08	28.18	84.85	3.33
RecursiveImagePyramid	3	AdvancedNormalizedCorrelation	32	(34.0, 46.0, 46.0)	45.35	28.21	84.93	3.42
RecursiveImagePyramid	3	AdvancedNormalizedCorrelation	32	(40.0, 10.0, 10.0)	44.65	26.6	84.76	3.45
RecursiveImagePyramid	3	AdvancedNormalizedCorrelation	32	(40.0, 10.0, 16.0)	46.01	27.8	84.85	3.63
RecursiveImagePyramid	3	AdvancedNormalizedCorrelation	32	(40.0, 10.0, 22.0)	45.43	28.23	84.97	3.41
RecursiveImagePyramid	3	AdvancedNormalizedCorrelation	32	(40.0, 10.0, 28.0)	45.35	28.21	84.93	3.42
RecursiveImagePyramid	3	AdvancedNormalizedCorrelation	32	(40.0, 10.0, 34.0)	45.35	28.21	84.93	3.42
RecursiveImagePyramid	3	AdvancedNormalizedCorrelation	32	(40.0, 10.0, 40.0)	55.17	29.47	84.58	4.13
RecursiveImagePyramid	3	AdvancedNormalizedCorrelation	32	(40.0, 10.0, 46.0)	51.84	24.36	83.34	3.31
RecursiveImagePyramid	3	AdvancedNormalizedCorrelation	32	(40.0, 16.0, 10.0)	44.7	23.82	85.51	2.87
RecursiveImagePyramid	3	AdvancedNormalizedCorrelation	32	(40.0, 16.0, 16.0)	46.75	21.92	83.51	7.46
RecursiveImagePyramid	3	AdvancedNormalizedCorrelation	32	(40.0, 16.0, 22.0)	45.76	23.16	85.08	2.74
RecursiveImagePyramid	3	AdvancedNormalizedCorrelation	32	(40.0, 16.0, 28.0)	47.35	24.73	84.74	2.84
RecursiveImagePyramid	3	AdvancedNormalizedCorrelation	32	(40.0, 16.0, 34.0)	44.15	27.1	85.05	3.56
RecursiveImagePyramid	3	AdvancedNormalizedCorrelation	32	(40.0, 16.0, 40.0)	44.82	27.87	85.27	3.13
RecursiveImagePyramid	3	AdvancedNormalizedCorrelation	32	(40.0, 16.0, 46.0)	46.83	28.8	84.66	3.77
RecursiveImagePyramid	3	AdvancedNormalizedCorrelation	32	(40.0, 22.0, 10.0)	43.48	27.01	84.79	3.92
RecursiveImagePyramid	3	AdvancedNormalizedCorrelation	32	(40.0, 22.0, 16.0)	46.03	29.08	84.72	4.12
RecursiveImagePyramid	3	AdvancedNormalizedCorrelation	32	(40.0, 22.0, 22.0)	45.96	26.77	84.5	3.34
RecursiveImagePyramid	3	AdvancedNormalizedCorrelation	32	(40.0, 22.0, 28.0)	49.95	31.68	84.01	3.95
RecursiveImagePyramid	3	AdvancedNormalizedCorrelation	32	(40.0, 22.0, 34.0)	45.67	27.55	84.49	3.8
RecursiveImagePyramid	3	AdvancedNormalizedCorrelation	32	(40.0, 22.0, 40.0)	45.42	28.22	84.87	3.46
RecursiveImagePyramid	3	AdvancedNormalizedCorrelation	32	(40.0, 22.0, 46.0)	47.09	27.25	84.81	3.4
RecursiveImagePyramid	3	AdvancedNormalizedCorrelation	32	(40.0, 28.0, 10.0)	46.25	25.86	84.53	3.34
RecursiveImagePyramid	3	AdvancedNormalizedCorrelation	32	(40.0, 28.0, 16.0)	46.84	26.6	84.54	3.22
RecursiveImagePyramid	3	AdvancedNormalizedCorrelation	32	(40.0, 28.0, 22.0)	48.9	27.85	84.14	3.42
RecursiveImagePyramid	3	AdvancedNormalizedCorrelation	32	(40.0, 28.0, 28.0)	49.09	27.96	84.12	3.14
RecursiveImagePyramid	3	AdvancedNormalizedCorrelation	32	(40.0, 28.0, 34.0)	51.75	26.82	84.15	3.54
RecursiveImagePyramid	3	AdvancedNormalizedCorrelation	32	(40.0, 28.0, 40.0)	49.35	26.84	84.71	3.56
RecursiveImagePyramid	3	AdvancedNormalizedCorrelation	32	(40.0, 28.0, 46.0)	49.96	25.85	84.93	3.65
RecursiveImagePyramid	3	AdvancedNormalizedCorrelation	32	(40.0, 34.0, 10.0)	50.67	25.32	84.83	3.4
RecursiveImagePyramid	3	AdvancedNormalizedCorrelation	32	(40.0, 34.0, 16.0)	51.2	24.2	84.57	3.02
RecursiveImagePyramid	3	AdvancedNormalizedCorrelation	32	(40.0, 34.0, 22.0)	50.97	23.3	84.5	3.16
RecursiveImagePyramid	3	AdvancedNormalizedCorrelation	32	(40.0, 34.0, 28.0)	51.31	25.17	83.96	3.48
RecursiveImagePyramid	3	AdvancedNormalizedCorrelation	32	(40.0, 34.0, 34.0)	48.71	23.86	84.37	3.72
RecursiveImagePyramid	3	AdvancedNormalizedCorrelation	32	(40.0, 34.0, 40.0)	44.88	25.33	85.3	3.15
RecursiveImagePyramid	3	AdvancedNormalizedCorrelation	32	(40.0, 34.0, 46.0)	47.86	24.27	84.88	3.31

Table A.9: Average performance of each set of parameters tested for the B-spline transformation

Pyramid	Resolutions	Metric	Bins	Spacing	mean HD	std HD	mean DSC	std DSC
RecursiveImagePyramid	3	AdvancedNormalizedCorrelation	32	(40.0, 40.0, 10.0)	46.22	24.39	85.09	3.12
RecursiveImagePyramid	3	AdvancedNormalizedCorrelation	32	(40.0, 40.0, 16.0)	43.23	25.25	85.33	3.26
RecursiveImagePyramid	3	AdvancedNormalizedCorrelation	32	(40.0, 40.0, 22.0)	48.24	24.51	84.8	2.93
RecursiveImagePyramid	3	AdvancedNormalizedCorrelation	32	(40.0, 40.0, 28.0)	46	26.81	84.67	3.3
RecursiveImagePyramid	3	AdvancedNormalizedCorrelation	32	(40.0, 40.0, 34.0)	41.05	22.49	85.38	3.35
RecursiveImagePyramid	3	AdvancedNormalizedCorrelation	32	(40.0, 40.0, 40.0)	43.98	28.32	85.38	3.55
RecursiveImagePyramid	3	AdvancedNormalizedCorrelation	32	(40.0, 40.0, 46.0)	40.82	24.41	85.53	2.87
RecursiveImagePyramid	3	AdvancedNormalizedCorrelation	32	(40.0, 46.0, 10.0)	42.91	22.65	85.25	3.07
RecursiveImagePyramid	3	AdvancedNormalizedCorrelation	32	(40.0, 46.0, 16.0)	43.61	25.22	85.27	3.36
RecursiveImagePyramid	3	AdvancedNormalizedCorrelation	32	(40.0, 46.0, 22.0)	39.39	21.11	85.21	3.15
RecursiveImagePyramid	3	AdvancedNormalizedCorrelation	32	(40.0, 46.0, 28.0)	42.85	24.84	85.18	3.3
RecursiveImagePyramid	3	AdvancedNormalizedCorrelation	32	(40.0, 46.0, 34.0)	42.03	25.2	85.42	3.26
RecursiveImagePyramid	3	AdvancedNormalizedCorrelation	32	(40.0, 46.0, 40.0)	40.83	26.28	85.43	3.23
RecursiveImagePyramid	3	AdvancedNormalizedCorrelation	32	(40.0, 46.0, 46.0)	41.62	24.1	85.62	3.11
RecursiveImagePyramid	3	AdvancedNormalizedCorrelation	32	(46.0, 10.0, 10.0)	43.98	22.11	85.24	3.13
RecursiveImagePyramid	3	AdvancedNormalizedCorrelation	32	(46.0, 10.0, 16.0)	45.24	24.32	85.14	3.5
RecursiveImagePyramid	3	AdvancedNormalizedCorrelation	32	(46.0, 10.0, 22.0)	43.12	25.14	85.4	3.17
RecursiveImagePyramid	3	AdvancedNormalizedCorrelation	32	(46.0, 10.0, 28.0)	43.5	23.94	84.88	3.33
RecursiveImagePyramid	3	AdvancedNormalizedCorrelation	32	(46.0, 10.0, 34.0)	41.41	23.74	85.48	2.94
RecursiveImagePyramid	3	AdvancedNormalizedCorrelation	32	(46.0, 10.0, 40.0)	41.8	24.21	85.65	2.97
RecursiveImagePyramid	3	AdvancedNormalizedCorrelation	32	(46.0, 10.0, 46.0)	40.61	24.54	85.8	2.82
RecursiveImagePyramid	3	AdvancedNormalizedCorrelation	32	(46.0, 16.0, 10.0)	42.37	25.24	85.07	3.64
RecursiveImagePyramid	3	AdvancedNormalizedCorrelation	32	(46.0, 16.0, 16.0)	41.92	25.64	85.29	2.84
RecursiveImagePyramid	3	AdvancedNormalizedCorrelation	32	(46.0, 16.0, 22.0)	40.27	24.12	85.24	2.96
RecursiveImagePyramid	3	AdvancedNormalizedCorrelation	32	(46.0, 16.0, 28.0)	41.92	24.02	84.98	3.13
RecursiveImagePyramid	3	AdvancedNormalizedCorrelation	32	(46.0, 16.0, 34.0)	41.8	23.68	84.76	3.27
RecursiveImagePyramid	3	AdvancedNormalizedCorrelation	32	(46.0, 16.0, 40.0)	39.06	23.44	85.66	3.06
RecursiveImagePyramid	3	AdvancedNormalizedCorrelation	32	(46.0, 16.0, 46.0)	40.87	27.26	85.18	3.59
RecursiveImagePyramid	3	AdvancedNormalizedCorrelation	32	(46.0, 22.0, 10.0)	40.14	25.36	85.09	3.48
RecursiveImagePyramid	3	AdvancedNormalizedCorrelation	32	(46.0, 22.0, 16.0)	41.12	23.29	85.13	3.33
RecursiveImagePyramid	3	AdvancedNormalizedCorrelation	32	(46.0, 22.0, 22.0)	41.83	25.72	84.78	3.34
RecursiveImagePyramid	3	AdvancedNormalizedCorrelation	32	(46.0, 22.0, 28.0)	43.58	26.38	84.52	3.72
RecursiveImagePyramid	3	AdvancedNormalizedCorrelation	32	(46.0, 22.0, 34.0)	41.58	23.06	84.56	3.27
RecursiveImagePyramid	3	AdvancedNormalizedCorrelation	32	(46.0, 22.0, 40.0)	41.06	24.52	84.92	3.17
RecursiveImagePyramid	3	AdvancedNormalizedCorrelation	32	(46.0, 22.0, 46.0)	41.69	26.51	85.15	3.19
RecursiveImagePyramid	3	AdvancedNormalizedCorrelation	32	(46.0, 28.0, 10.0)	41.87	23.66	84.75	3.42
RecursiveImagePyramid	3	AdvancedNormalizedCorrelation	32	(46.0, 28.0, 16.0)	43.97	24.24	85.04	3.11
RecursiveImagePyramid	3	AdvancedNormalizedCorrelation	32	(46.0, 28.0, 22.0)	41.92	25.89	84.67	3.24
RecursiveImagePyramid	3	AdvancedNormalizedCorrelation	32	(46.0, 28.0, 28.0)	41.25	24.28	84.68	3.63
RecursiveImagePyramid	3	AdvancedNormalizedCorrelation	32	(46.0, 28.0, 34.0)	45.77	25.34	84.89	2.88
RecursiveImagePyramid	3	AdvancedNormalizedCorrelation	32	(46.0, 28.0, 40.0)	43.93	24.43	84.74	3.09
RecursiveImagePyramid	3	AdvancedNormalizedCorrelation	32	(46.0, 28.0, 46.0)	47.92	26.34	83.58	5.16
RecursiveImagePyramid	3	AdvancedNormalizedCorrelation	32	(46.0, 34.0, 10.0)	43.59	23.67	85.12	2.78
RecursiveImagePyramid	3	AdvancedNormalizedCorrelation	32	(46.0, 34.0, 16.0)	43.67	22.06	85.02	3
RecursiveImagePyramid	3	AdvancedNormalizedCorrelation	32	(46.0, 34.0, 22.0)	46.57	24.92	84.79	2.78
RecursiveImagePyramid	3	AdvancedNormalizedCorrelation	32	(46.0, 34.0, 28.0)	46.25	24.13	84.77	2.99
RecursiveImagePyramid	3	AdvancedNormalizedCorrelation	32	(46.0, 34.0, 34.0)	45.88	26.49	84.51	3.51
RecursiveImagePyramid	3	AdvancedNormalizedCorrelation	32	(46.0, 34.0, 40.0)	46.13	29.29	84.99	3.11
RecursiveImagePyramid	3	AdvancedNormalizedCorrelation	32	(46.0, 34.0, 46.0)	45.86	23.69	84.97	2.88
RecursiveImagePyramid	3	AdvancedNormalizedCorrelation	32	(46.0, 40.0, 10.0)	45.02	22.77	84.98	3.01
RecursiveImagePyramid	3	AdvancedNormalizedCorrelation	32	(46.0, 40.0, 16.0)	45.81	26.43	85.33	3.39
RecursiveImagePyramid	3	AdvancedNormalizedCorrelation	32	(46.0, 40.0, 22.0)	44.95	23.71	84.74	3.32
RecursiveImagePyramid	3	AdvancedNormalizedCorrelation	32	(46.0, 40.0, 28.0)	41.1	22.74	85.35	2.48
RecursiveImagePyramid	3	AdvancedNormalizedCorrelation	32	(46.0, 40.0, 34.0)	43.81	23.08	84.77	3.14
RecursiveImagePyramid	3	AdvancedNormalizedCorrelation	32	(46.0, 40.0, 40.0)	42.37	23.83	85.07	3.13
RecursiveImagePyramid	3	AdvancedNormalizedCorrelation	32	(46.0, 40.0, 46.0)	43.79	21.63	84.9	3.01
RecursiveImagePyramid	3	AdvancedNormalizedCorrelation	32	(46.0, 46.0, 10.0)	41.98	21.88	85.38	2.85
RecursiveImagePyramid	3	AdvancedNormalizedCorrelation	32	(46.0, 46.0, 16.0)	42.2	21.82	85.29	3.24
RecursiveImagePyramid	3	AdvancedNormalizedCorrelation	32	(46.0, 46.0, 22.0)	43.91	25.11	84.98	3.17
RecursiveImagePyramid	3	AdvancedNormalizedCorrelation	32	(46.0, 46.0, 28.0)	42.39	22.17	85.15	3.13
RecursiveImagePyramid	3	AdvancedNormalizedCorrelation	32	(46.0, 46.0, 34.0)	43.51	23.88	84.75	3.09
RecursiveImagePyramid	3	AdvancedNormalizedCorrelation	32	(46.0, 46.0, 40.0)	41.61	23.64	85.12	3.18
RecursiveImagePyramid	3	AdvancedNormalizedCorrelation	32	(46.0, 46.0, 46.0)	42.01	25.83	85.19	3.24

A.3/ List of Publications

A.3.1/ Submissions Needing Revision

Diana M. Marin-Castrillon, Leonardo Geronzi, Arnaud Boucher, Siyu Lin, Marie-Catherine Morgant, Alexandre Cochet, Michel Rochette, Sarah Leclerc, Khalid Ambarki, Ning Jin, Ludwig Serge Aho Glele, Alain Lalande, Olivier Bouchot, Benoit Presles. Segmentation of the aorta in systolic phase from 4D flow MRI. Multi-atlas vs. deep learning. Magnetic Resonance Materials in Physics Biology and Medicine (MAGMA), 2022

A.3.2/ Journal - Submitted

Diana M. Marin-Castrillon, Alain Lalande, Sarah Leclerc, Khalid Ambarki, Marie-Catherine Morgant, Alexandre Cochet, Siyu Lin, Olivier Bouchot, Arnaud Boucher, Benoit Presles. 4D segmentation of the thoracic aorta from 4D flow MRI using deep learning. Magnetic Resonance Imaging (MRI), 2022.

A.3.3/ Journal - Published

Siyu Lin, Marie-Catherine Morgant, **Diana M. Marin-Castrillon**, Chloe Bernard, Arnaud Boucher,Benoit Presles, Alain Lalande, and Olivier Bouchot, (2022). What Are the Biomechanical Properties of an Aortic Aneurysm Associated with Quadricuspid Aortic Valve?. Journal of Clinical Medicine, volume 11, pages 4897.

Siyu Lin, Marie-Catherine Morgant,**Diana M. Marin-Castrillon**, Paul Michael.Walker Walker, Ludwig Serge Aho Glélé, Arnaud Boucher, Benoit Presles, Olivier Bouchot, and, Alain Lalande (2022). Aortic local biomechanical properties in ascending aortic aneurysms. Acta Biomaterialia, volume 149, pages 40-50.

Marie-Catherine Morgant, Siyu Lin, **Diana M. Marin-Castrillon**, Chloe Bernard, Aline Laubriet, Alexandre Cochet, Alain Lalande, Olivier Bouchot, (2021). Comparison of two techniques (in vivo and ex-vivo) for evaluating the elastic properties of the ascending aorta: Prospective cohort study. PLOS ONE, volume 16, number 9.

A.3.4/ Conference paper

Diana M. Marin-Castrillon, Arnaud Boucher, Siyu Lin, Chloe Bernard, Marie-Catherine Morgant, Alexandre Cochet, Alain Lalande, Olivier Bouchot, and Benoit

Presles. Multi-atlas Segmentation of the Aorta from 4D Flow MRI: Comparison of Several Fusion Strategies. In Statistical Atlases and Computational Models of the Heart (STACOM), Virtual. Multi-Disease, Multi-View, and Multi-Center Right Ventricular Segmentation in Cardiac MRI Challenge. Lecture Notes in Computer Science, volume 13131, pages 3–11, October 2021, Strasbourg, France.

A.3.5/ CONFERENCE ABSTRACT

Diana M. Marin-Castrillon, Arnaud Boucher, Siyu Lin, Chloe Bernard, Marie-Catherine Morgant, Alexandre Cochet, Alain Lalande , Benoit Presles , and Olivier Bouchot. Automatic 3D PC-MRI atlas-based segmentation of the aorta. International Society for Magnetic Resonance in Medicine. May 2021.

Diana M. Marin-Castrillon, Leonardo Geronzi, Siyu Lin, Benoit Presles, Arnaud Boucher, Chloe Bernard, Marie-Catherine Morgant, Alexandre Cochet, Alain Lalande, Olivier Bouchot. Automatic multi-atlas-based segmentation of the aorta to determine hemodynamic biomarkers - Computer Methods in Biomechanics and Biomedical Engineering. October 2021, Saint-Etienne, France.

Document generated with LaTeX and:
the LaTeX style for PhD Thesis created by S. Galland — http://www.multiagent.fr/ThesisStyle
the tex-upmethodology package suite — http://www.arakhne.org/tex-upmethodology/